BUBBLE PLUMES IN CROSSFLOW:

LABORATORY AND FIELD MEASUREMENTS OF THEIR FLUID DYNAMIC

PROPERTIES WITH APPLICATION TO LAKE AERATION AND MANAGEMENT

A Dissertation

by

MARYAM REZVANI

Submitted to the Office of Graduate and Professional Studies of
Texas A&M University
in partial fulfillment of the requirements for the degree of

DOCTOR OF PHILOSOPHY

Chair of Committee,	Scott Socolofsky
Committee Members,	Kuang-An Chang
	Sharath Girimaji
	Steve DiMarco
Head of Department,	Robin Autenrieth

May 2016

Major Subject: Civil Engineering

ABSTRACT

This dissertation presents laboratory experiments of bubble plumes in crossflows and field measurements in managed lakes aerated by bubble plumes to better understand the behavior of bubble plumes in natural environments. The laboratory experiments were conducted to investigate the detailed time-average and turbulent fluctuating velocity field in the wake region behind the bubble column and above the separation height, at which fluid entrained at the base of the plume separates from the bubbles. These measurements are important for developing predictive models for bubble plume dynamics and for quantifying their mixing characteristics. Two field campaigns, at Carvins Cove in Virginia and at Lake Hallwil in Switzerland, were conducted to measure the detailed bottom boundary currents and oxygen exchange across the sediment-water interface for different diffuser operations. These lakes have different bubble plume diffuser types, and they span a range of shape, bathymetry, and environmental forcing. These field data are useful to elucidate the physical mechanisms by which currents resulting from both natural forcing (e.g., seiches) and artificial forcing (e.g., bubble plumes) affect oxygen uptake at the sediment-water interface, with the ultimate goal of better management of aeration systems in drinking water reservoirs.

Experimental techniques applied in the laboratory experiments include Particle Image Velocimetry (PIV) and Planar Laser Induced Fluorescence (PLIF). Crossflows were generated in two ways: by towing the source and by forcing a recirculation current. A combination of field equipment was used in the field campaigns, including a microprofiler for temperature and oxygen; point and profiling acoustic Doppler

velocimeter (ADV); thermistor chains; conductivity, temperature, and depth (CTD) profiles; and a meteorological station. During the field experiments, the bubble plume flow rate was varied to produce different dynamic and chemical conditions in the lakes.

The laboratory experiments present a cohesive view of the flow dynamics in the wake of a bubble plume in crossflow. Using the forced and towed plume validates the analogy of the towed plume to that of the real current. The observations showed that no secondary bubble plume forms above the separation height, but rather the bubble column becomes a continuous source of vertical momentum to the wake region. The resulting vertical velocities impart a rising frame of reference on the separated plume so that its trajectory scales like a buoyant jet despite the absence of buoyancy in the separated fluid. Maximum values of the Reynolds stresses and mixing occur at the base of the separated plumes, and the bubble column elevates both the turbulence intensity and the kinetic energy throughout the wake region.

The *in situ* field measurements provide insight into the role of aeration bubble plumes on the oxygen dynamics at the sediment-water interface. Detailed, simultaneous measurements of turbulence and oxygen uptake in the bottom boundary layer allowed the direct validation of boundary exchange models. The measurements also showed that unsteady operation of the bubble plume results in generation of basin-scale internal waves that drive measurable currents in the bottom boundary layer. Moreover, measurements showed that it is the oxygen concentration outside the diffusive boundary layers that is the dominant mechanism for controlling the uptake at the sediment-water interface.

DEDICATION

To Mohammad, my best friend and lovely husband, for his patience and during this journey across the globe.

"If nature were not beautiful it would not be worth knowing, and life would not be worth living."

Henri Poincaré

ACKNOWLEDGEMENTS

Obtaining my PhD has been quite a journey for me and I take it upon myself to thank many people for their guidance, assistance, and support during this journey.

Above all, I would like to extend my deepest gratitude to my advisor, Dr. Scott Socolofsky who gave me the great opportunity to work on this project and for all his fruitful suggestions, invaluable help, trust, and motivation. His passion for teaching and research and his high standard professional attitude has been a prominent source of inspiration for me during this journey and for the rest of my career path. I am thankful for many things I have learned from him and for all the support he provided me to attend national and international conferences to present our work, and more importantly the opportunity to collaborate with world-class organizations such as EAWAG and Deltares.

I would like to specially thank my committee members, Dr. Sharath Girimaji, Dr. Kuang-An. Chang, and Dr. Steve DiMarco for all the helpful comments and suggestion they provided during the course of my research and for all the great courses I had with them. I greatly appreciate all their motivation. Many thanks go to Dr. Girimaji who gave me a lot of help in understanding of the turbulence world.

I would like to extend my sincere gratitude and appreciation to Dr. John Little and Kevin Bierlein of Virginia Tech whom I closely collaborated with for the field portion of this project. It has been a pleasure conducting experiments and collaborating with you. I would like to extend my thankfulness to Dr. Little for everything I have learned from him. Special thanks to Kevin whose expertise was a key component of

conducting demanding field experiments and for being such a great colleague and friend and for teaching me a lot of cool and helpful field tip during the campaigns.

My sincere thanks go to Dr. Johny Wuest of EAWAG for his continuous contribution and invaluable help with his deep experience and also for providing us the opportunity to collaborate with EAWAG to do the field experiments. I have learned tremendously in the course of the field experiments we were collaborating with their world class Institute. I would also like to thank Michi Schruter for providing us technical solution for all the issues during the field campaign.

During my course of research I had a pleasure to meet many great people and learn from their valuable knowledge and experience through the discussions we had. My special thanks go to Rob Uittenbogaard, Daniel McGinnis, and Bruno Fraga who gave me invaluable advice on different aspects of the project.

I also would like to thank my colleagues Anusha, Binbin, Chris, Vadoud, Kerri, Samira and InOk for all the valuable helps they provided through our discussions.

My sincere thanks go to the people and organizations that contribute to the field portion of this research including Western Virginia Water Authority staff. I am also thankful to Mr. John Reed for his untimely help during my laboratory setup.

My especial thanks go to my dear friends Mona, Mojdeh, Nessrine, Jawad, Ehsan, Saeid, and Cheng de Wu for all their help, the enjoyable moments we had together and all the energy I received from them.

Last but not least, I would like to thank my beloved parents, brothers, and family for giving me all kind of support and unconditional love and help whenever I needed,

also my dear husband for all his help. The days I spent with him working/writing side-by-side have been as enjoyable as they have been productive.

NOMENCLATURE

α	Entrainment Coefficient
ρ_w	Density of Ambient Water
ρ_b	Density of Gas Bubbles at Discharge Location
ρ	Reference Density of Reservoir Fluid
ADCP	Acoustic Doppler Current Profiler
ADV	Acoustic Doppler Velocimeter
ALP	Advected Line Puff
ALT	Advected Line Thermal
B	Bubble Buoyancy Flux
BBL	Bottom Boundary Layer
BDFF	Buoyancy Dominated Far Field
CCR	Carvin's Cove Reservoir
CFD	Computational Fluid Dynamics
CO_2	Carbon Dioxide
CTD	Conductivity, Temperature and Depth Profiler
D	Bombardelli Characteristic Length Scale
DBL	Diffusive Boundary Layer
DO	Dissolve Oxygen
FOV	Field of View
g	Gravitational Constant

HOx	Hypolimnetic Oxygenation Systems
h_s	Separation Height,
JO2	Oxygen Flux
LH	Lake Hallwil
LIF	Laser Induce Fluorescence
MDFF	Momentum Dominated Far Field
NSF	National Science Foundation
O_2	Oxygen
PIV	Particle Image Velocimetry
PLIF	Planar Laser-Induced Fluorescence
Qg	Volumetric Air Flow rate at Diffuser
RMSD	Root-Mean-Square Deviation
SWI	Sediment-Water Interface
u_∞	Ambient Velocity
U_a	Ambient Velocity
u_s	Bubble Slip Velocity

TABLE OF CONTENTS

LIST OF FIGURES

xvii

LIST OF TABLES

1. INTRODUCTION

Multiphase flows are ubiquitous in natural and man-made environments and have been the focus of significant research in fluid dynamics. In recent years, scientists and engineers have explored new topics in multiphase flows due to their relevance in important areas such as global warming, water quality control, and analysis, mitigation, and risk assessment of oil well blowouts. Ocean carbon sequestration, i.e. release of CO_2 in the form of multiphase plumes in the deep ocean, has been considered as one approach to mitigate rising CO_2 concentration in the atmosphere, an important forcing for the global climate system. Multiphase plumes are increasingly used in the form of bubble plumes for mixing or aeration in lakes to improve water quality by addition of oxygen, also, with the trend toward deepwater oil and gas exploration and production, there is heightened risk for the oil-well blowouts, which generate multiphase plumes of oil and gas. A key feature of the multiphase plumes in these examples is their ability to mix and transport the surrounding water. For CO_2 sequestration and lake management, the induced mixing and transport are integral to the performance of the engineered systems; thus, the efficiency and performance of each design would benefit from better understanding of bubble plume behavior in the enclosing environment. For oil-well blowouts, mixing and transport determine the locations and toxicity of the impact; hence, mitigation and risk assessment benefit from better understanding of mixing processes in multiphase plumes.

Environmental conditions, including ambient currents, are very influential in determining the behavior of multiphase plumes in their applications. In the presence of

an ambient current, a multiphase plume will be deflected downstream. As the current becomes stronger, it starts to strip the entrained continuous phase fluid away from the dispersed bubbles, drops, or particles, thus, reducing upward flux of entrained water. Eventually, when the crossflow becomes strong enough, the plume may reach an equilibrium condition where inflow through the plume leading edge is matched to outflow in the downstream wake. In this condition, the upward velocity of entrained fluid is minimized. In spite of the important influence that crossflow can have on the behavior of multiphase plumes, there are comparatively few studies devoted to multiphase plumes in the presence of currents, and very few quantitative data for velocity fields through multiphase plumes in crossflow. To optimize the application of multiphase plumes in environmental systems where currents are ubiquitous, it is important to improve the knowledge of the behavior and performance of the multiphase plumes in moving environments. For this purpose, this dissertation applies both laboratory and field experiment methods to study bubble plumes, a particular case of a multiphase plume, in realistic ambient conditions. This study particularly focuses on the understanding of physical mixing and transport processes in air-aerated bubble plumes in crossflows and the influence of bubble plume operation on the overall flow characteristics in closed basins.

1. 1.   Motivation of study

Depletion of oxygen in the hypolimnia of lakes and reservoirs is a pernicious global problem which negatively affects the drinking-water treatment process, cold-water fisheries, and riverine flow impacted by releases from hydropower reservoirs.

Mitigation of low level oxygen levels is increasingly accomplished using hypolimnetic oxygenation via bubble plumes. While properly designed bubble plumes are successful at adding oxygen, recent studies have shown that uptake of oxygen across the sediment-water interface is correlated with the diffuser gas flow rate. This may be caused by larger concentration gradients across the sediment-water interface, mixing induced by currents generated by the bubble plume, or a combination of these processes. Yet, no definitive data exist to determine a mechanism, and existing coupled 3-D hydrodynamic lake models do not account for the currents induced by the bubble plumes. To bridge this gap, this dissertation aims to elucidate the flow field induced by a bubble plume in crossflow and to study the current field in the benthic boundary layer of two oxygenated. The tools developed in these studies will allow lake managers to efficiently design artificial bubble plumes for maximum input of oxygen. Moreover, the bubble plume models are also generally useful for modeling a wide array of multiphase plume applications, including CO_2 sequestration and oil well blowouts.

1. 2. Bubble plumes in a crossflow

Bubbles released from a localized source rise through the water column and entrain ambient water. This upward rising mixture, driven by the buoyancy of the bubbles, constitutes a plume. Crossflows alter the plume dynamics by causing the plume to deflect in the downstream direction. Because the bubbles slip relative to the water, in strong crossflow the bubbles may separate from the water on the leading edge of the plume (Socolofsky and Adams, 2002a) . Figure 1 shows a laboratory bubble plume in a crossflow. The image is an instantaneous sample from laboratory experiments of bubble

3

plumes in crossflow using the Planar Laser Induced Fluorescence (PLIF) technique to visualize the plume center plane. In these experiments, the fluorescent dye was injected at the source to track the path traced out by the entrained ambient fluid. The velocity streamlines are also shown in the figure on top of the PLIF image. Streamlines are computed using the Particle Image Velocimetry (PIV) technique, by which velocities are quantified throughout the flow on the same two-dimensional center plane. As seen in Figure 1, close to the source, the entrained fluid rises with the bubbles forming a plume. Prior to the onset of separation, modeling of the bubble plume can be simplified by treating the mixture as a mixed single-phase plume with $B = \frac{\Delta \rho}{\rho} g Q_b$ as its initial buoyancy flux, where ρ = ambient density, $\Delta \rho$ = density difference at the source, g = acceleration due to gravity, and Q_b = the volume flux of air at the source. After reaching the separation height, entrained fluid separates from the bubbles. Thereafter, air bubble trajectory can be predicted from the sum of the slip velocity and ambient current velocity. Socolofsky and Adams (2002) derived empirical correlations for the separation height (h_s) from similar laboratory experiments and found $h_s = 5.1 B / (u_\infty u_s^{2.4})^{0.88}$ where u_∞ = ambient velocity and the u_s = bubble slip velocity. Here, the empirical constant *5.1* is dimensionless and is determined from the experiments.
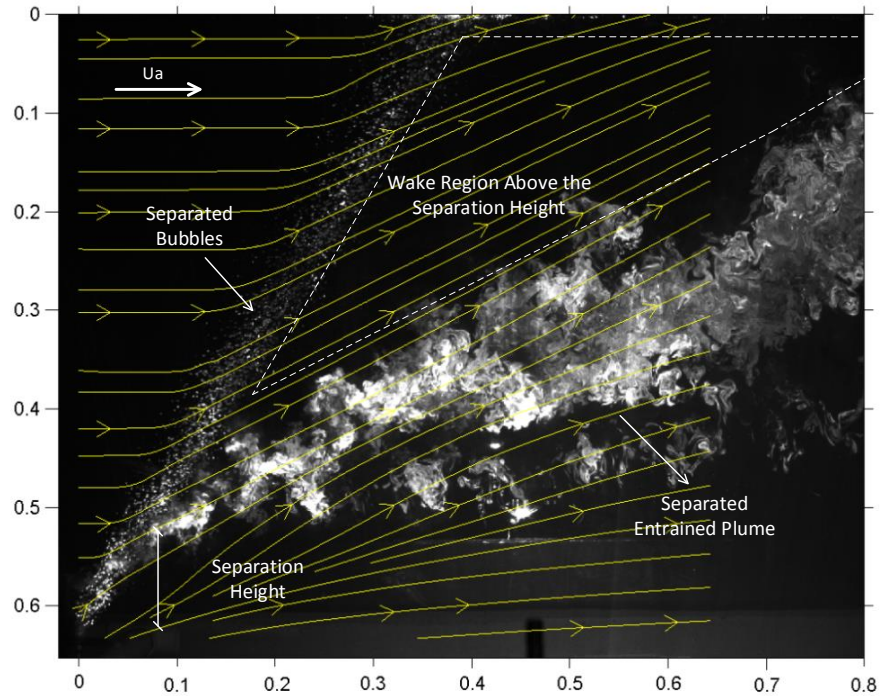
Figure 1. Definition image for bubble plume in crossflow (Ua)

1.2.1 *Knowledge gaps*

The wake region above the separated entrained plume is shown in Figure 1 in the outlined dashed triangle. There are scarce measurements in this region and little is known about the properties of flow in this region. Consequently, there are a few issues that are still unclear and can be resolved using the measurements in this region. For example, it is of interest to determine whether a secondary bubble plume would form above the separation height. Additionally, the dynamics of the wake behind the bubble column is of significant importance especially for applications such as aeration and bubble plume mixing. To answer these questions and understand this region in detail, measurements of the velocity field in this wake region are needed for bubble plumes in crossflow. At the same time, the averaged and instantaneous measurement database

collected in these experiments forms a valuable and consistent dataset for the validation

and development of advanced three-dimensional two-phase flow simulation tools.

1.2.2   Scaling analysis for bubble plume

To design the experiments and to relate the results to field scale, it is important to

define the fundamental scaling parameters of a bubble plume in crossflow.

Scaling laws for bubble plumes have been reported by many studies (Asaeda and

Imberger, 1993; Mcdougall, 1978; Milgram, 1983; Socolofsky and Adams, 2002a,

2005). Socolofsky and Adams (2002) extended the work of Wright, (1984) who

analyzed the general case of a single-phase buoyant jet in a stratified crossflow. They

defined the governing dimensional parameters for a bubble plume in crossflow by

making some simplifications which led to the following parameters: the crossflow

velocity u_∞, the slip velocity u_s (which is the terminal rise velocity of a bubble in a

stagnant reservoir that includes the dynamic effect of several bubble properties), the

height above the discharge, and the buoyancy flux (B). Thus, in functional form, any

properties of bubble plume in crossflow can be written as $\phi = f(B, u_\infty, u_s, z)$. Correlation

equations in (Socolofsky and Adams, 2002b) for the case of crossflow provide the

relationship for h_s as previously defined in this section.

(Bombardelli et al., 2007) established a characteristic length scale in an

unstratified, quiescent bubble plume, given as $D = \dfrac{B}{4\pi\alpha^2 u_s^3}$ (where α is the entrainment

coefficient). They showed that the plume properties become asymptotic (i.e. independent

of initial conditions) when $z/D > 5$. The existence of this length scale explains why the

6

bubble plume is not really self-similar, since self-similarity is only possible if there is only one geometric length scale in the problem (e.g., z). Since D is an additional geometric length scale, self-similarity breaks down for the bubble plumes. This break down in self-similarity is weak, however, so that results from integral models remain valuable.

In stratification, another length scale emerges, which is related to the trapping height of the stratification, given by $l_c = \left(\dfrac{B}{N^3}\right)^{\frac{1}{4}}$ where $N = [-(g/\rho)(\partial\rho/\partial z)]$ is the buoyancy frequency of the stratification. Entrainment of stratified water results in negative buoyancy for the plume fluid. If the negative buoyancy overcomes the positive buoyancy of the bubbles, the water will separate, or peel, forming an intrusion layer at a trap height h_T, given from experiment by

$$\frac{h_T}{l_c} = 2.9\exp\left(\frac{-(U_N - 1.0)^2}{5.3^2}\right)$$

(1)

where $U_N = u_s/(BN)^{1/4}$ is the non-dimensional slip velocity (Socolofsky and Adams, 2005).

For bubble plumes in crossflow, stratification can be ignored if $h_s << h_T$, that is, separation is caused by the crossflow before it would be initiated by the stratification (Socolofsky and Adams, 2002b). This dissertation will focus on the crossflow dominant case.

In this case where stratification is negligible, three dominant length scales are:

- Water depth, H which is a limiting parameter on the height of the plume.

- Characteristic length scale D of an unstratified bubble plume.

The non-dimensional ratios of these parameters, i.e, $\xi_D = \dfrac{H}{D}$, and $\xi_s = \dfrac{H}{h_s}$,

define the scaling laws needed to relate laboratory experiments to the field (provided $h_s \ll h_T$); they also help to define the relevant parameter space covered by a set of experiments.

1. 3. Lake aeration management

A large number of lakes and reservoirs around the world are increasingly managed by bubble plumes to artificially add oxygen to the lake bottom water. Excessive loadings of phosphorous increase the content of organic matter, which leads to increase in oxygen demand upon decomposition of the organic matter at the sediments. Meanwhile, stable stratification conditions, particularly in summer months, inhibit the replenishment of oxygen to bottom water by surface aeration. As a result, lower layers exhibit significantly reduced water quality due to low oxygen concentration while oxygen is needed to sustain a healthy lake ecosystem and to reduce costs for water treatment in drinking water supplies (Little and McGinnis, 2001). A considerable amount of literature has been published on the consequences of oxygen depletion in lakes and reservoirs (Beutel et al., 2008; Cooke and Carlson, 1989; Paul A. Gantzer et al., 2009; Huttunen et al., 2006; Stefan, 1992).

Engineered bubble plumes in lakes have been studied in detail in the literature (Hugi, 1993; Mcdougall, 1978; Wüest et al., 1992). Integral models for bubble plumes in stratified reservoirs have been developed (Asaeda and Imberger, 1993; Wüest et al.,

1992) and validated to field data in quiescent stratification (Lemckert and Imberger, 1993; Singleton et al., 2007; Wüest et al., 1992). Although bubble plumes can be designed to perform their role by adding oxygen successfully, studies have shown that they may increase the consumption of oxygen at the sediments. Whether this increased O_2 uptake is due to the higher concentration of O_2 in the hypolimnion or increased mixing resulting from currents generated by the bubble plume is unclear.

1.3.1   Knowledge gap

Despite the current broad application of bubble plumes in lakes, little is known about if /how turbulence changes caused by bubble plume operations affect Oxygen Uptake at the sediment-water interface in the field (J_{O2}), where J_{O2} can be significantly affected by natural turbulence as well. Furthermore, it is of great importance to know how the uptake can be predicted from the bottom turbulence and oxygen concentration profiles. It would be beneficial for the numerical models and for designing bubble plume diffusers to more accurately predict the induced sediment oxygen uptake. The current best practice is the use of an induced hypolimnetic oxygen uptake multiplier as a factor of safety (Beutel, 2003; Moore et al., 1996). To answer these questions field measurements in two lakes aerated by bubble plumes were conducted to measure J_{O2} and the benthic boundary layer flow dynamics under different environmental conditions and bubble plume operations. Together with the laboratory experiments, these observations provide a holistic view of bubble plume dynamics in natural conditions and their potential effects in closed basins.

1. 4.   Dissertation organization

This dissertation is a compilation of three manuscripts which have been prepared for publication, each included as separate sections followed by the summary of results for further research and appendices that give the details of the experimental methods and selected results.

A preview of the content of each section is provided below:

Section 2- In this section, the averaged properties of the flow on the center-plane of a bubble plume is quantified in the laboratory using PLIF and PIV. Also, through two sets of independent experiments the analogy of a towed plume to a bubble plume in a real cross flow is validated. Using these observations, we quantify the trajectory of the separated continuous phase, provide data for validation of numerical simulations, gain a better understanding of flow behavior at the wake and propose a conceptual model to predict the vertical velocity of the ambient water flowing through the bubble column above the separation height.

Section 3 - The overarching goal of this section is to present the analysis of velocity field and turbulence statistics measured from laboratory PIV experiments downstream of a round bubble plume in moving ambient, using high-speed velocity field data. Profiles of turbulence intensities and Reynolds stresses are presented for this kind of flow for the first time and the effects of bubbles on turbulence generation are investigated.

Section 4- The ultimate goal of this section is to study the effects of bubble plume operation on near-sediment mixing and oxygen uptake in real lakes and to use

these field observations to develop a physics-based predictive model for the flux of

oxygen across the sediment-water interface as a result of mixing induced by natural and

artificial currents, as from a bubble plume for lake aeration.

Each manuscript is intended to stand alone and have its own conclusion. Even

though each section has its own list of references, these were omitted in the individual

sections and are instead presented at the end of the dissertation.

2. EXPERIMENTS ON PHYSICS OF BUBBLE PLUMES IN CROSSFLOW

2. 1.   Overview

This paper presents detailed laboratory experiments of a round bubble plume in uniform crossflows. Standard Particle Image Velocimetry (PIV) technique was utilized to obtain the velocity field of the continuous phase in the plume center plane. The PIV data were obtained from twenty-five separate camera fields of views used to map the whole velocity field over a 65.5cm × 68.5cm region. The analogy of a towed plume to that of a real current was also examined by comparing the results from two independent experiments (i.e., using a towed source and recirculating flume). Analysis of the time-averaged velocity field shows that: the trajectory of the separated continuous phase fluid in the wake behind the bubble column deviates from the asymptotic power laws for momentum jet and instead matches plume scaling laws due to the vertical momentum imparted by the bubbles on fluid flowing through the bubble column above the separation height. A conceptual model is proposed to predict the vertical velocities of the ambient water above the separation point which agrees well with the measured velocities.

2. 2.   Introduction

Natural and engineered bubble plumes often occur in flowing environments. Such applications include lake aeration (Wüest et al., 1992) , reservoir desertification (Lemckert and Imberger, 1993), reducing salt intrusion (Uittenbogaard et al., 2015), and accidental subsea oil-well blowouts (Mcdougall, 1978). Socolofsky and Adams (2002)

showed that fluid entrained in the base of a bubble plume in crossflow may be lifted to varying elevations depending on the plume configuration, and then separates itself from the plume. This leads to the idea that the existence of crossflow has the potential to have a positive or negative impact on the objective functionality of the bubble plume depending on the design purpose. For example, for reservoir destratification purposes, it is important to know whether the bubble plume is capable of lifting the bottom water into the epilimnion and eroding the thermocline. Also, the impact of crossflow on the design goal was an important question for the destratification of Notterdom waterways, in which, the possibility of using bubble plumes instead of hard structures was considered for the purpose of preventing the intrusion of the seawater into the fresh water intakes of the irrigation systems. Likewise, in aeration systems, crossflow can impact the contact time between the water and the gas. This will control the concentration of the dissolved gas and distribution of the injected gas into the hypolimnion of the lake. For oil-well blowouts, designing better mitigation technologies and making better decisions during future disasters require better understanding of the transport of released oil and gas under ambient currents during the blowout. This paper, in particular, addresses these concerns by investigating the flow field downstream of a round bubble plume in a moving ambient fluid. An improved understanding of the behavior of bubble plumes in ambient currents will lead to more accurate predictions of the environmental impacts of underwater oil and gas blowouts and more efficient design of aeration and destratification systems.

Most previous experimental studies focus on bubble plumes in virtually stagnant water (Bryant et al., 2009a; D.-G. Seol et al., 2007), and very limited laboratory experiments were conducted in crossflows. The general problem of single-phase jets/ or plumes in a crossflow has been studied extensively in the past; e.g. Fan (1967) and Lee and Chu (2003), and experiments of single and multiphase plumes in crossflow have observed some similar traits. In their studies of vertical buoyant jets discharged into a perpendicular crossflow, Davidson and Pun (1999) and Pun and Davidson (1999) observed tracer detachment from the main body of the jet that leads to an elongated lower jet edge. They showed the detachment of tracer happens whenever the ambient-to-entrainment velocity ratio becomes high enough. Hugi (1993) and (Socolofsky and Adams, 2002b) observed a similar behavior for bubble plumes in crossflows. This can be explained by the fact that in bubble plumes, bubbles are not required to follow the fluid and instead slip; as a result, crossflow can pull and separate the entrained fluid from the rising bubbles. Consequently, when the entrainment velocity becomes weaker than the crossflow, the crossflow pulls the fluid out of the plume, i.e. exhausting it of its entrained water. Above this critical point in the plume, the bubble column behavior resembles more that of a porous column than a plume. (Socolofsky and Adams, 2002b) quantified the characteristic separation height as the height where the fluid entrained at the base of the plume separates from the dispersed phase. They provided an empirical equation that relates the separation height h_s to the bubble buoyancy flux $B = \frac{\Delta\rho}{\rho} g Q_b$

(where ρ = ambient density, $\Delta\rho$ = density difference at the source, g = acceleration due

to gravity, and Q_b = the volume flux of air at the source), ambient crossflow velocity u_∞ and the bubble slip velocity u_s as

$$h_s = \frac{5.1B}{(u_\infty u_s^{2.4})^{0.88}}$$ (2)

where the empirical constant 5.1 is dimensionless and determined from the experiments. Based on the defined separation height, they categorized the crossflow into weak and strong. In a weak crossflow, entrainment keeps the plume fluid with the bubbles throughout the reservoir depth; whereas, in a strong crossflow, the plume fluid entrained at the source will separate from the bubbles at the separation height, below the free surface. Figure 2 shows the problem of the bubble plume as presented by Socolofsky and Adams (2002). Also, separated entrained plume in the downstream wake and the wake region above the separation height is shown on this figure. Tracking fluid entrained at the source, as was done by Socolofsky and Adams (2002) , is of practical importance in applications such as oil well blowouts where small oil droplets may be expected to follow the entrained fluid. In other applications such as lake aerations or CO_2 sequestration, the pathways of water entering the plume at all heights are of interest to predict the concentration of dissolved gas downstream of the bubble plume.

Available quantified data in bubble plumes in crossflows are very limited with scarce velocity information for much of the flow field. Hugi (1993) performed experiments of bubble plumes in crossflows using the towed approach and presented coarse data on the velocity field in the wake. Zhang and Zhu (2013) did an experimental study on characteristics of bubbly jets in crossflow. The jets were generated by releasing water together with air from a nozzle in their study, they focus on the bubble properties

and did not obtain velocity measurements of the continuous phase. They also released

dye streaks windward of the bubbly jets to track the movement of the ambient water

passing the bubbly jets and they qualitatively observed that bubble induced water

velocity inside the bubble plume is significant for the bubbly jets with small and no

water flow rate. However, these studies did not measure the velocity field in the wake

and consequently, there are no quantified velocity measurements over the downstream

wake especially above the separation height which is needed to better understand the

mixing and validate numerical models in this region of the flow.
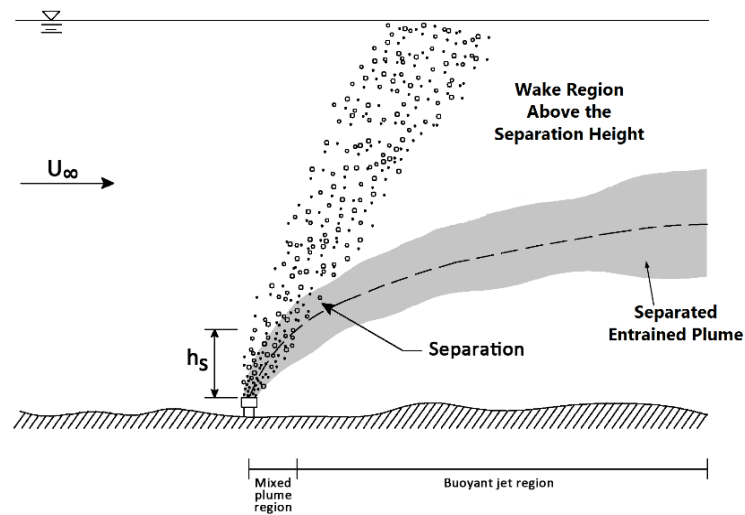
Figure 2. Bubble plume in a crossflow, adapted from Socolofsky and Adams (2002)

Numerical methods of bubble plume analysis span the range from one-

dimensional integral models to fully three-dimensional computational fluid dynamics

(CFD) models. Integral models have been used to predict the bubble plume's properties

in the stagnant ambient conditions (Crounse et al., 2007; Mcdougall, 1978; Socolofsky et

al., 2008). These models are based on the self-similarity and entrainment hypotheses.

Nonetheless, in crossflow, bubbles are not required to travel with the entrained ambient

water, and entrained fluid in the plume core may continually be refreshed by the currents, which violates the self-similarity assumption of the integral model approach. For the case of crossflows, Socolofsky and Adams (2002) showed that prior to separation, the two-phase plume can be modeled as a mixed single-phase plume with B as its initial buoyancy flux. As h_s is reached, all entrained water from the source is observed to be detrained into the wake of the plume becomes a single-phase momentum jet. The trajectory of this separated continuous phase can be predicted with its momentum flux derived from the local entrained fluid velocity and width at the separation height. The trajectory of the dispersed bubble column can be predicted from the sum of the slip velocity and ambient current velocity. Thus, the integral model as described can track the trajectory of the fluid which is entrained at the source of the plume but does not consider the fluid passing through the plume into the wake in the leeward side of the plume or the bubble plume induced flow field above h_s. A few other integral models have been developed based on these observations to predict accidental oil-well blowouts in the presence of crossflows (Johansen, 2000; Yapa et al., 1999; Yapa and Chen, 2004; Yapa and Li, 1997; Zheng et al., 2003). These studies have used limited field and laboratory data as related experimental data are very rare (Chen and Yapa, 2004). These models include the effects of cross currents and separation of continuous phase from the dispersed phase. They track the continuous phase of the plume after the separation of the dispersed phase and track the separated dispersed phase using lagrangian particle tracking models. However, none of these models consider the effects of the wake formed due to the plume or the dynamic effect of the separated dispersed

17

phases. Therefore, there is a need for data to validate these numerical techniques, to predict the crossflow-plume interaction, and to further investigate the wake region flow where models have not been validated.

To address this existing research gap, this paper uses laboratory experimental data to study the behavior of the bubble plumes in crossflow to quantify the time-averaged velocity field throughout the bubble plume and its downstream wake in a forced current using PIV. In a separate set of experiments, a towed source has been used with dye visualization (similar to Socolofsky and Adams (2002)). To determine whether a towed bubble plume is representative of a bubble plume in a real crossflow (e.g., forced current) and also to check that the presence of flume turbulence did not bias the results, streamlines from the PIV measurements in the open-channel were compared with PLIF results for a towed plume. Using these comprehensive experimental measurements, the flow field has been thoroughly quantified on the center plane of the plume (i.e., below the separation height, above the separation height and also at the separated continuous phase).

Sections 2.3 and 2.4 present the experimental methods and data analysis. Section 5 reports the observations and discussions, which includes the detailed measurement results of the plume and its downstream wake, comparison between a towed plume and crossflow, contrasting the trajectory of the separated continuous phase with asymptotic scaling laws for jets and plumes, and introduces a conceptual model to predict the vertical velocities above the separation height. Finally, the main conclusions are summarized in section 5.

2. 3.   Experimental methods

The experiments were carried out in a glass-walled flume 35 m long by 0.9 m wide and 1.2 m deep in the Fluid Dynamics Laboratory of the Zachry Department of Civil Engineering at Texas A&M University. The tank is equipped with both a towing carriage, to simulate crossflow by moving the plume source, and a recirculation pump system, which was used to simulate different ambient currents (generating a forced current). Hence, crossflow was created in two different, yet comparable, ways, and independent sets of experiments were conducted for open channel crossflow and towed source along the long axis of the flume with the plume placed in the center axis of the flume. The measurement approach for each set of experiment is described in the following.

To generate the bubble plume, we used a 2.5 cm tall by 1.4 cm in diameter porous aquarium airstone, which was located at the centerline of the wave flume at a depth of 0.68 m. The bubble flow rates were chosen as $Q_o = 0.5$, 1 and 1.5NL/min to match those of previous experiments with zero crossflow (D. Seol et al., 2007). The bubble flow rates at standard pressure and temperature were monitored by a calibrated gas flowmeter. As reported in Lai and Socolofsky (2015), who used a similar setup, the generated air bubbles have a median diameter d_{50} of 2.4 mm (Figure 3) with a corresponding velocity of 24 cm/s (Clift et al., 2005a). The bubble size was visually validated from the raw images in the crossflow experiments.
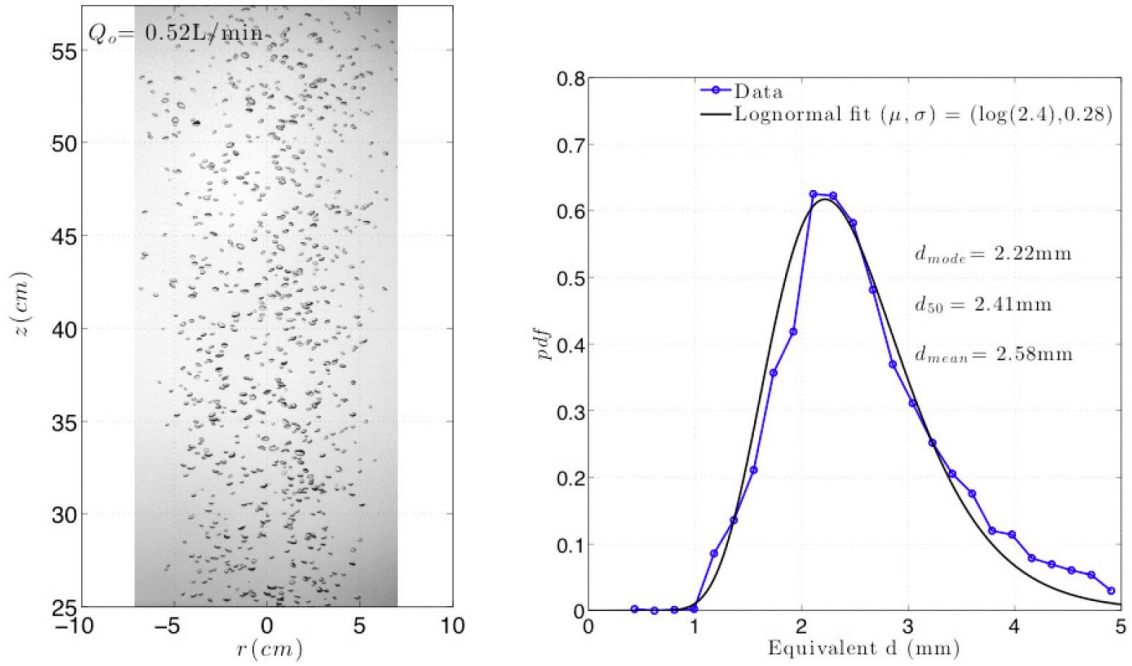
Figure 3. Bubble size distribution adopted from Lai and Socolofsky (2015)

Three different ambient currents of u∞=4, 10, and 15 cm/s were simulated in open channel crossflow and u∞=4, 10, and 14.5 cm/s in the towed experiments. Combined with the water depth and the bubble flow rates, these crossflows span a range of separation heights (i.e., no separation, weak separation, and strong separation). Table 1 summarizes the full range of experimental conditions for these experiments. In the table, h_s is the separation height and D is a characteristic length scale given by $\dfrac{B}{4\pi\alpha^2 u_s^3}$ where $\alpha = 0.083$ (Bombardelli et al., 2007).

Table 1. Parameters of the crossflow experiments analyzed using particle image velocimetry

Crossflow Velocity, u_∞ (m/s)	Water Depth, H (m)	Bubble Flow rate, Q_o (Nl/min)	B (m⁴/s³)	Slip Velocity, u_s(m/s)	H/D	H/h_s
0.04	0.68	0	0	-	-	
		0.5	7.663e-5	0.17	3.54	2.43
		1	0.0001533	0.18	2.1	1.36
		1.5	0.0002299	0.20	1.92	1.13
0.1	0.68	0	0	-	-	
		0.5	7.663e-5	0.17	3.54	5.23
		1	0.0001533	0.18	2.1	3.1
0.15	0.68	-	0	-	-	
		1	0.0001533	0.18	2.1	4.25
		1.5	0.0002299	0.20	1.92	3.58

For the towed experiments, the crossflow was simulated using the overhead tow carriage. The diffuser was mounted to the carriage by an L-shaped PVC support in a way that the diffuser could be supported at the tank centerline and disturbance of the flow in the tank was minimized. The tow carriage was equipped with a variable speed motor yielding speeds of 4 to 14.5 cm/s.

For open channel flow, crossflows were generated using two centrifugal pumps equipped with a frequency controller. The pumps are capable of generating flows ranging between 1.32 and 6.06 m³/s. The flow rates were monitored by the inline propeller flow meter in the external recirculation piping as well as by ADV velocity measurements in the flume during the experiments. Recirculating flow enters the flume through a ramp inlet in the flume bottom creating a submerged wall jet. In order to destroy the jet structure of the inflow at the flume entrance, an array of bricks was placed immediately after the inflow (Ghisalberti and Nepf, 2002). A homogeneous grid of

porous plates was then used to smooth the velocity profile as suggested by Stoker (1946). Flow straighteners made out of PVC pipes with a diameter of 2.54cm and length of 70cm were used to eliminate large scale turbulence and secondary currents. The bubble plume was located at 19 times the water depth downstream of the flow straightener, which was about 2/3 of the flume length. Measurements of the velocity field validated the uniform open channel flow condition in the measurement section.

In all the experiments, the center plane of the bubble plume was illuminated by a laser sheet. The vertical illumination plane along the centerline of the bubble diffuser was produced using continuous lasers along with a pair of cylindrical lenses that focused and expanded the beam, creating the light sheet. The light sheet was formed outside the tank and directed into the tank through the glass at the side of the tank and oriented upward by a mirror placed on the bottom of the tank.

For the towed bubble plume, visualization of the bulk flow field was accomplished by qualitative planar laser induced fluorescence (PLIF) using a continuous wave Nd: YAG laser, operating on a single wavelength of 532 nm and capable of peak power up to 5.3 W. This high power was needed to illuminate the large field of view spanning the full wake region in one camera field of view. Rhodamine 6G dye was used as the dye tracer and was injected as a continuous point source just upstream of the aquarium airstone, at the same depth as the diffuser. The dye flow rate was held constant using a Marriot bottle configuration. Following injection, the dye stream was rapidly entrained into the front of the plume and tracked along the streamline of fluid entrained near the base of the plume. A schematic of the setup is shown in Figure 4. The dye was

efficiently excited by the Nd: YAG laser and fluoresced at a peak emission near 550 nm.

Images were captured using a progressive scan CCD camera (Basler acA1600-20gm

gigE interface camera). The video images were processed to quantify characteristic

scales of the plume evolution. These include the height of separation of the dyed fluid in

the wake of the plume, the centerline trajectory of the dye streak, and the visual tracking

of individual coherent structures in the dye plume.
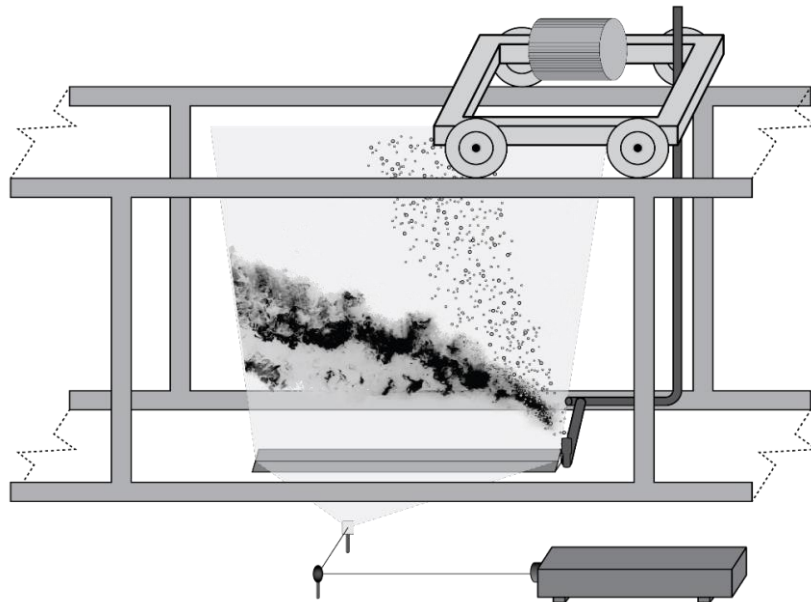
Figure 4. Schematic of the PLIF setup

Quantitative measurements for the forced current case were accomplished using

PIV, where the source of light sheet was a continuous Argon-ion laser (Spectra- Physics)

capable of a peak power of 2.8 W. The flume water was seeded with neutrally buoyant

homopolymer polyamide particles (manufactured by Vestonic) with mean diameter of

56 microns and of specific gravity 1.03. Flow images were captured by a high speed

Phantom camera (Phantom v5.1, Vision Research Inc.) mounted on a three-dimensional

traverse and positioned perpendicularly to the light sheet. The camera frame rate was 200Hz and the exposure time was 300 microseconds collecting 2000 images for each measurement burst (e.g., 10s burst duration, limited by camera physical memory). The resolution of the camera is 1024×1024 pixels at 10 bit gray scale resolution. In order to cover the whole field of interest, 25 fields of view (FOV) were used, starting from the center of the bubble diffuser. Each FOV is defined by two numbers; first number indicates the row number and the second number shows the number of column in our measurement matrix. Each FOV has the dimension of 15×15 cm with 1.5 cm overlap. Experiments were repeated three times at each FOV, which resulted in a total of 30 seconds of data, or 6015 images at each flow rate. The PIV processing of these images resulted in 30s of instantaneous velocity data (in 10s bursts), providing the full-field velocity along the plume center plane. Meanwhile, PIV sequences were neither synoptic from FOV to FOV nor were the data contiguous over the whole 30 s at each measurement point; therefore, we rebuild the flow field from statistical averages of the results. Figure 5 shows a schematic of the experiment setup.
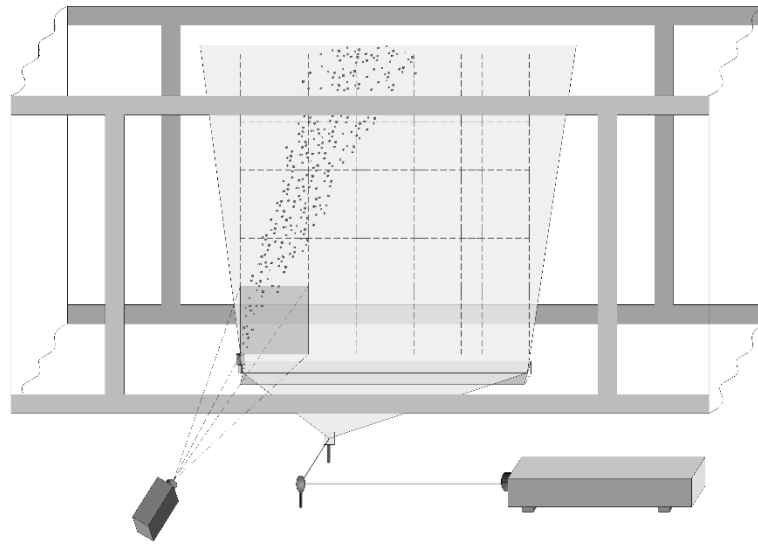
Figure 5. Schematic of the PIV setup

2. 4.　Data analysis

2.4.1.　Image preprocessing and PIV analysis

Before applying the PIV algorithm to the images, the dispersed phase (i.e., bubbles) needs to be discriminated from the seeding particles in the FOVs that contain bubbles to obtain the continuous phase velocities. Previous studies suggested three approached to remove the bubble signatures: Optical separation, removing bubble signature by pre-processing the images, and vector post-processing of the mixed-phase velocity field (Seol and Socolofsky, 2008a). In this study we used the second method and removed the bubbles by pre-processing the images containing both phases, which resulted in images containing only particles to which PIV can be applied. A size and brightness discrimination method was used based on the method introduced by (Seol and Socolofsky, 2008a) for separating the bubbles. The MATLAB image processing toolbox

25

was used for identifying the bubbles based on their size and brightness; an appropriate mask was created for each image from the identified bubbles which could remove the dispersed phase from the image. This was accomplished as follows: Initially, background noise was removed by subtracting the mean of all the images. Secondly, the image was converted to a binary image containing all the pixels above a threshold intensity determined by trial and error. This way bubbles and tracer particles that were outside the laser sheet and illuminated from the reflected light were eliminated. Then the area-open algorithm was applied to the binary image to remove the contiguous objects below a threshold size to remove the tracer particles. To fill the possible hollow areas in the bubbles, the area close algorithm was used to create filled bubbles. Finally, to make up for the fact that the bubble mask was from the binary image, the bubble mask was dilated to cover the area around the bubbles which fell below the threshold value. This new black and white mask of bubbles was multiplied by the original image to obtain an image with only bubbles, and was subtracted from the original image to obtain the particle image. This process takes trial and error to find the appropriate parameters. Figure 6 displays a raw image of a sample FOV containing bubbles (top), the bubble mask identified with image processing (middle), and the post processed result after removing the bubbles (bottom).
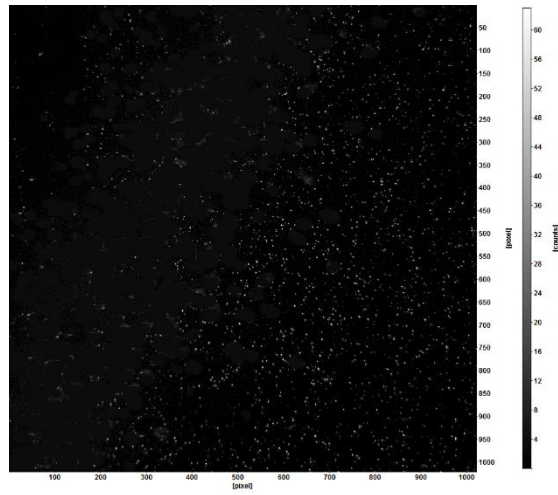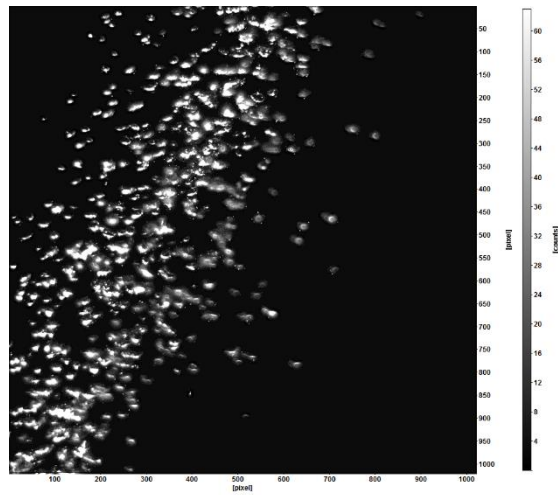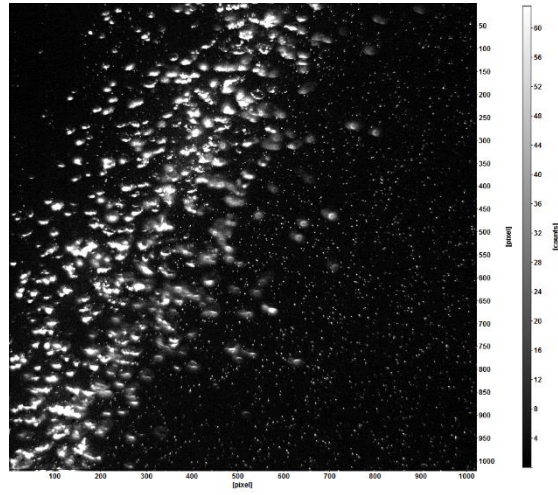
Figure 6. Images of FOV (3, 2), case 0.15-1.5. Top: the original image, middle: bubble mask, bottom: the image with the bubbles removed

Because of the removal of the bubbles, the data coverage in the plume core is intermittent. This was circumvented partly by time averaging over the total experiment duration of 30 seconds, thereby obtaining the mean velocity across the whole plume core. However, for high bubble concentrations, some of the velocity statistics in the plume, did not converge. These regions are omitted from our analysis.

The LaVision Davis software package was used to perform the PIV processing and obtain the velocity vector field. Velocities were calculated using a multiple pass interrogation window with 50% overlap. The iterations used an initial window size of 64 by 64 pixels and a final interrogation window size of 32 by 32 pixels, yielding a uniform vector grid of 2.3 by 2.3 mm. To remove the vectors that did not accurately represent the flow field, a median filter was applied to the resulting velocity field by comparing each vector to the root mean square of the 8 surrounding vectors, and spurious vectors were replaced by a local neighbor average. A sample of the resulting instantaneous velocity field for the particle image in Figure 6 is shown in Figure 7.
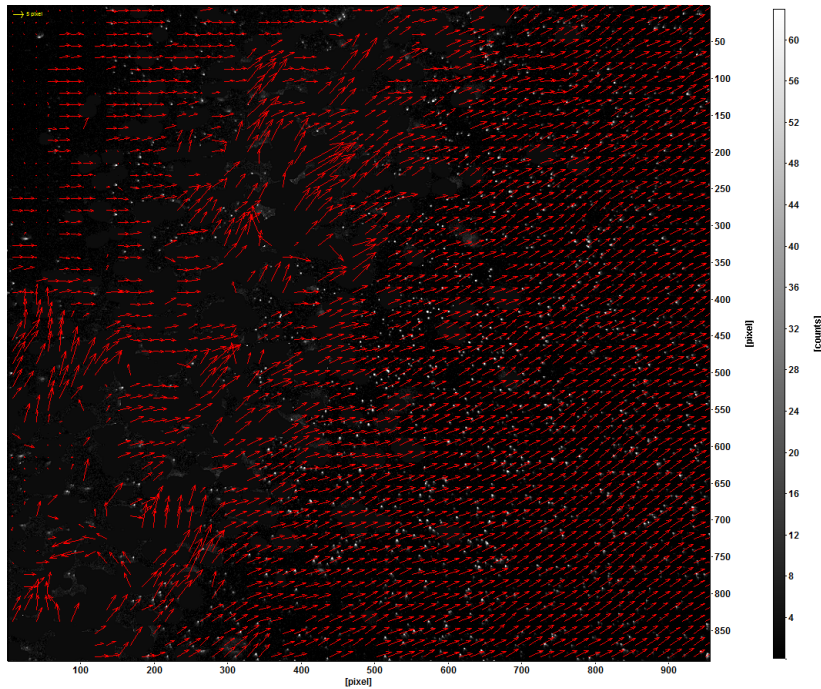
Figure 7. Instantaneous velocity field for FOV (3,2) for the PIV measurements of case 0.15-1.5

2.4.2.   PLIF analysis

Video images from the PLIF experiments were processed to visualize the

trajectory of the dye streak, separation of the dyed fluid in the wake of the plume, and

the behavior of bubble plume for different cases. A sample image is shown in Figure 8.

The images were rectified for geometric distortion based on the images of calibration

grid plate to yield accurate geometric scaling.
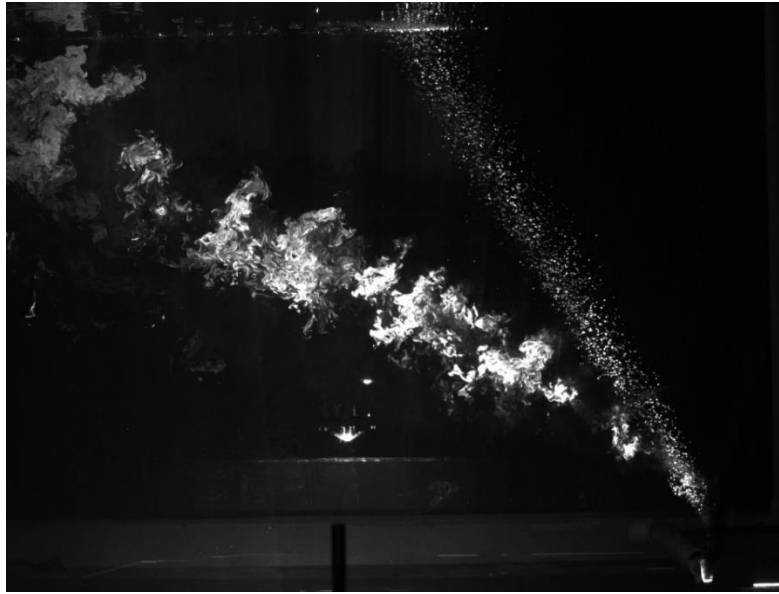
Figure 8. Still image of PLIF experiment for a tow speed of 0.1 m/s and 1 Nl/min bubble flow rate

In this study, a total of 9 experimental scenarios were investigated as presented in Table 1. Experiments are identified with two numbers: the first number indicates the current velocity and the second number shows the bubble flow rate. For example case 0.04-0.5 is the case with the crossflow velocity of 0.04 m/s and bubble flow rate of 0.5 NL/min.

2. 5.   Observations and discussions

2.5.1.   *Comparison of forced crossflow and towed plume*

Previous studies simulated crossflow using a towed bubble plume, where ambient water was not moving and ambient turbulence was neglected (Socolofsky and Adams, 2002b; Zhang and Zhu, 2014). In this study, data from PLIF and PIV experiments were analyzed and compared to address three main questions. The first question is whether a towed source in stagnant water would accurately represent a fixed

30

source in a crossflow and produce the same plume. The agreement between these results

can validate the towed-plume analogy. The second question is whether the ambient

turbulence in the forced crossflow has an impact on the results. Lastly, the third question

addressed by this comparison is whether the vertical velocities measured in the PIV data

are consistent with the upward motion of the dye in the PLIF experiments. This question

is raised since the wake field is three dimensional and the dye in the wake will spread

throughout the full wake region, which may cause the mean advection of dye to not

match the PIV measured velocity on the center plane. To address these questions, the

streamlines of the wake flow field were computed directly from the time averaged PIV

data in the forced current experiment and then plotted on top of the rectified PLIF

images from analogous experiments using a towed source. Figure 9 shows streamlines

laid over PLIF images for different cases of the flow, including weak separation cases

(such as $u_\infty = 0.04$ m/s and $Q_0 = 1$ NL/min) and strong separation cases such as ($u_\infty = 0.15$

m/s and $Q_0 = 1.5$ NL/min). The PLIF images have been flipped right to left to match the

direction of the PIV data and the grayscale has been inverted to improve clarity of the

presentation.
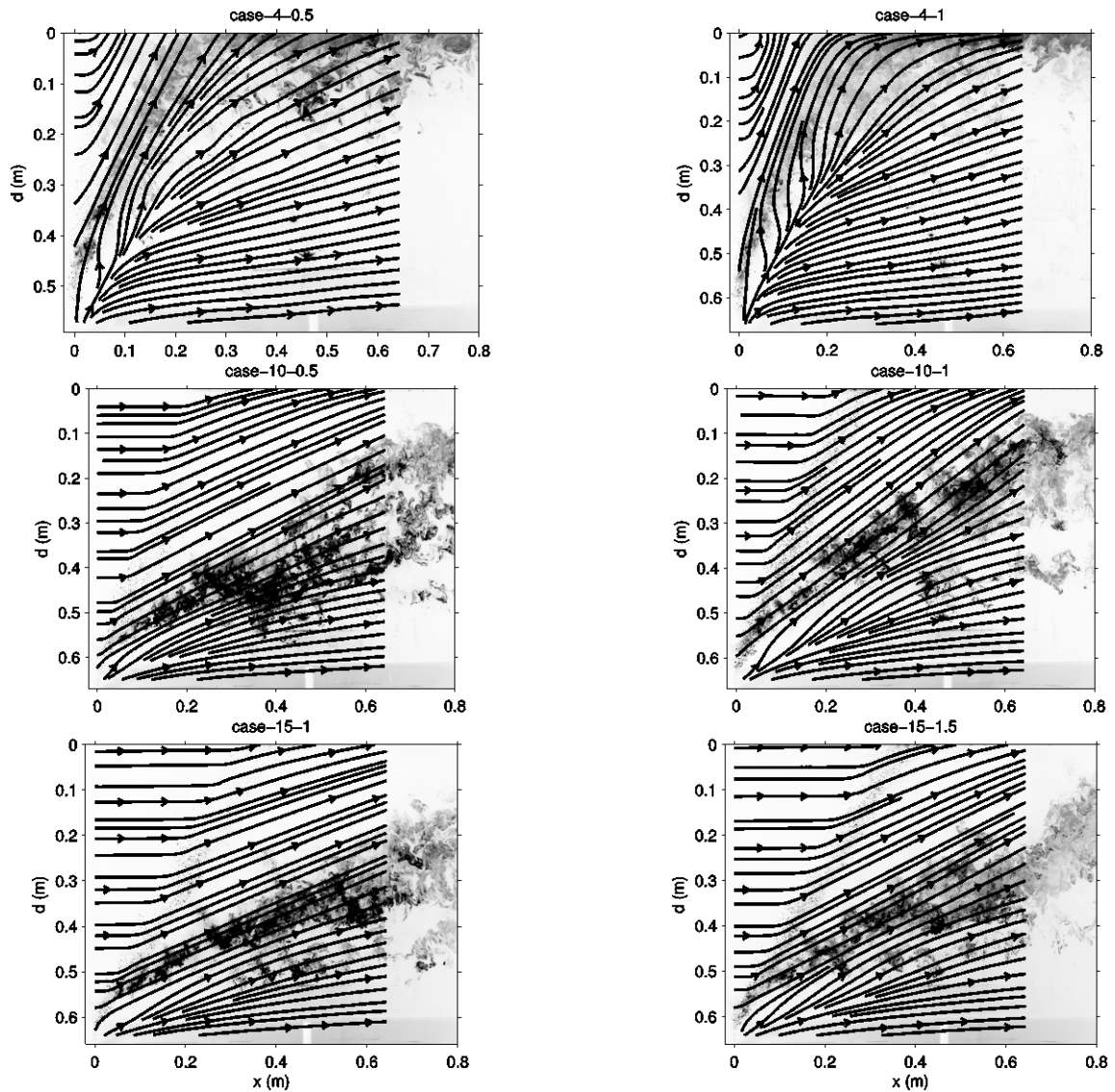
Figure 9. Comparison of PLIF observations to PIV streamlines for different cases of bubble flow rates and current velocities

As observed in Figure 9, the agreement between the trajectory of the dye from the PLIF experiments and the streamlines from the PIV experiments is quite similar for all the cases. Hence, the dye trajectory along the center plane of a towed bubble plume can be assumed to match streamlines computed from the velocity field in a real current for these steady flows. This supports the analogy of a towed plume to that of a real

current. These observations suggest that the streamline and streakline along the center plane are identical indicating the center plane of the flow is a symmetry plane, furthermore, the observed agreement in trajectories of dye and streamlines implies that the vertical and longitudinal advection experienced by the dye agrees with the average velocity from the PIV on the center plane only. The agreement also verifies the quality and accuracy of the time average PIV data.

From the plots in Figure 9, we also notice that the region where entrainment overcomes the crossflow is clearly visible on the downstream side of the plume. This is indicated in the PLIF data where dye has not yet separated from the plume. For the streamlines, this region is bounded by the point where the streamlines stop entering the. This is in accordance with the theoretical model of (Socolofsky and Adams, 2002b), which hypothesized that separation begins when the crossflow velocity exceeds the entrainment velocity on the downwind side of the plume, leading to the onset of dye leakage. Note also in the images that entrainment does not resume on the downstream side of the bubble column for any height above this point, implying that the bubble plume in crossflow is exhausted of its entrainment (i.e., continuously leaks its fluid in the wake) above the separation height.

The streamlines in Figure 9 display two separate behaviors. First, below the separation height, the streamlines point upward, along the rising plume, and none of the entering streamlines exit the plume until a point at or slightly above the separation height. Second, behavior belongs to the fluid entrained at the base of the plume in which the streamlines go up with the plume and exit at or above the separation height.

33

Second, above the separation height, streamlines enter the plume horizontally on the upstream side of the plume and then become advected upward eventually leaving the plume on the downstream side, somewhere above the point where the streamline entered the plume. Each of the streamlines are also parallel in nature.

Whether entrained below the separation height or above it, the fluid exiting the plume has vertical momentum, as witnessed by the upward trajectory of the dye and streamlines in the wake. This vertical velocity stems from transfer of the plume buoyancy force of the bubbles to vertical momentum of the ejected water. Above the separation height, the lack of entrainment on the downstream side and weaker upward trajectory of streamlines within the bubble column, lead to the definition of an "exhausted" plume: one that no longer increases in volume flux continuously by entrainment, and whose size and cross section change only by differential advection and diffusion. Hence, it evolves to some kind of equilibrium between upstream capture of fluid and downstream loss.

2.5.2.   *Investigating the separated phase behavior*

As previously shown by Socolofsky and Adams, (2002b) for a bubble plume in crossflow, above the separation height, the trajectory of the separated continuous phase may be predicted as that of a single phase momentum jet. Theories of single phase jets and plumes are well developed in the literature and different software such as CORMIX (Doneker et al., 1990), VISJET, and Visual Plume are widely used for modeling the single phase buoyant jets. Moreover, some commonly used relations based on

34

experiments and dimensional analysis have been reported for jet and plume trajectories; such as the relations proposed in Wright, (1977a, b), and Lee and Chu (2003).

The bent-over phase of a turbulent jet or plume in crossflow has been analyzed numerically and experimentally using the Advected Line Puff (ALP) and Advected Line Thermal (ALT) analogy. Wright, (1977a, b) and Lee and Chu, (2003) proposed the following power laws for the trajectories of the centerline of jets and plumes in crossflow:

$$\frac{z_c}{L_m} \sim \left(\frac{x}{L_m}\right)^{\frac{1}{3}} \text{ Advected Line Puff (ALP)/ Momentum Dominated Far Field (MDFF)} \qquad (3)$$

$$\frac{z_c}{L_b} \sim \left(\frac{x}{L_b}\right)^{\frac{2}{3}} \text{ Advected Line Thermal (ALT)/ Buoyancy Dominated Far Field (BDFF)} \qquad (4)$$

where x and z_c are horizontal and vertical coordinates of the jet centerline, measured from the nozzle, respectively and $L_m = \frac{M_{v_0}^{1/2}}{U_a}$,and $L_b = \frac{F_0}{U_a^3}$ are the crossflow momentum and buoyancy length scales used to non-dimensionalize the centerline distances where M_{v_0} is the vertical jet momentum flux, F_0 is the buoyancy flux, and U_a is the crossflow velocity.

As mentioned previously, the trajectory of pure jets in crossflow can be predicted by ALP. To investigate the trajectories of bubbly jets in crossflows, Zhang and Zhu, (2014) examined the centerline trajectories of the water and air phase in bubbly jets in crossflows after separation. In their study, the centerline trajectories of the water phase were identified from the jet's lower and upper boundaries using a photographic technique. They modeled the liquid-phase centerlines for bubbly jets with large water

35

flow rate Q_w using a single-phase jet model and compared the measured visual centerline with the modeled one. They observed some deviations from the measured centerline beyond a certain distance from the nozzle for some of their cases due to the lifting effects of bubbles on the liquid phase; however, they did not find this bubble induced lifting substantial and they concluded that using the single-phase momentum jet model is overall satisfactory to model the bubbly jets; hence, they drew the conclusion that the centerlines for bubbly jets follow an advected line puff relationship. Nevertheless, they did not model the centerline for bubble plumes and bubbly jets with low Q_w (i.e., bubble plumes), due to the difficulty in determining the centerline in these cases for their experimental methods.

In order to examine the behavior of the separated continuous phase in bubble plumes in an objective way, we investigate the behavior of the streamlines and the locus of the maximum velocities in the wake, defined as the location of maximum velocity magnitudes found from the PIV velocity field data, as the representatives for the trajectory of the separated phase. Figure 10 displays a plot of a representative image of dye experiments for case (15-1). An arbitrary streamline has been picked in the middle of the dye and is shown by the yellow line in the figure. Dark blue lines show the visual boundaries of the separated dyes and the red line represents the visual centerline. The locus of the maximum velocity magnitude is also plotted on the figure. Streamlines follow the visual trajectory of the centerline as is delineated in Figure 10 and also expected since streamlines have been shown in section 2.5.1 to follow the dye trajectories. To further visualize the flow field, a velocity profile along a vertical transect

at *x*=45 cm has been shown in Figure 11 for this case. Velocities above the 15 cm/s

ambient current result from acceleration around the bubble column and within the plume

below the separation height.
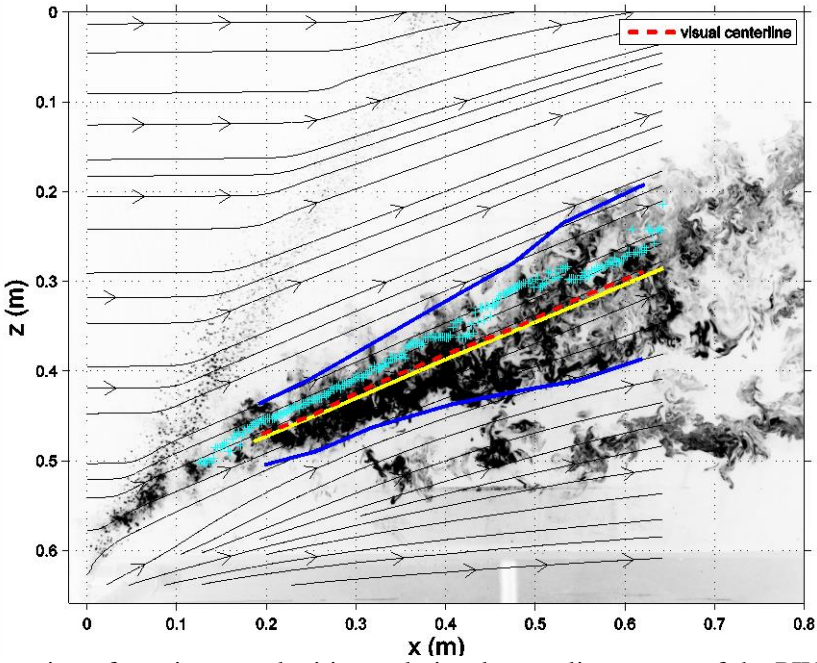
Figure 10. Location of maximum velocities and visual centerline on top of the PIV streamlines and PLIF results for case of 15-1
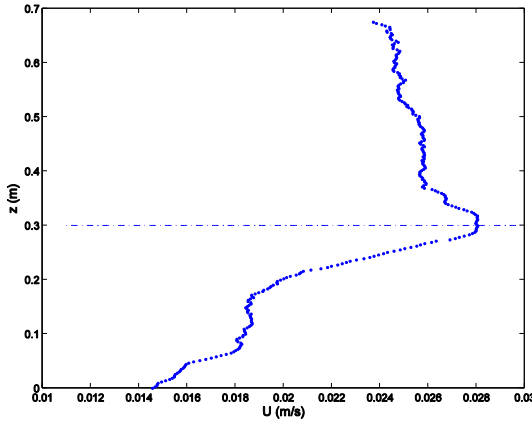
Figure 11. Profile of the velocity magnitude at x= 0.45 m

It is evident from Figure 11 that the trajectory defined by the locus of maximum velocities is located higher than the visual centerline of the dye tracer, which is due to the pear-shaped structure of the jet in crossflow as shown in Figure 12 (Lee and Chu, 2003); the visual trajectory is normally defined as the midpoint between the bottom and top boundaries of the dye tracer.
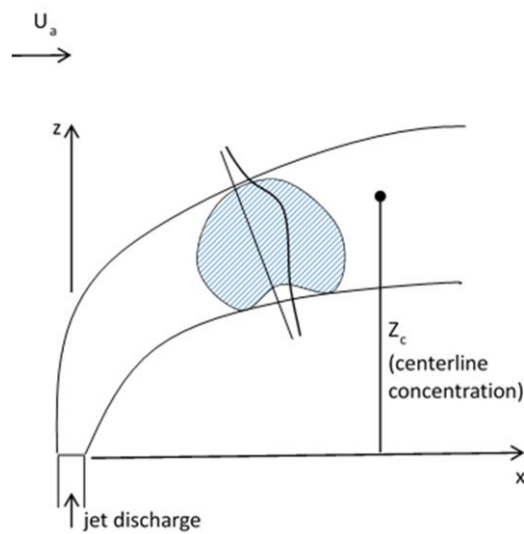
Figure 12. Asymptotic flow regime showing the vortex-pair concentration profile in the farfield for a jet in crossflow adapted from Lee and Chu, (2003)

To study the asymptotic behavior of the separated dye plume, Figure 13 presents a log-log plot of the plume trajectories based on the velocity data together with the ALP and ALT asymptotic slopes. As is evident in Figure 13, the measured maximum trajectory line appears to overlays with the streamlines and fits very close to the 2/3 trajectory law of the ALT. Previous models in the literature assumed the separated dye plume could be modeled using pure jet equations after the gas bubbles separate from the plume. Moreover, for these experiments with neutrally buoyant dye, there is no

buoyancy in the separated plume region. As a result, we would have expected the asymptotic slope of the separated plume to have a 1/3 slope, conforming to an advected line puff. However, the trajectory given by the streamlines and the locus of maximum velocity are experiencing 2/3 slopes. Especially for the cases of stronger crossflows, where the separation happens faster and the separated continuous phase exits with lower initial velocities.
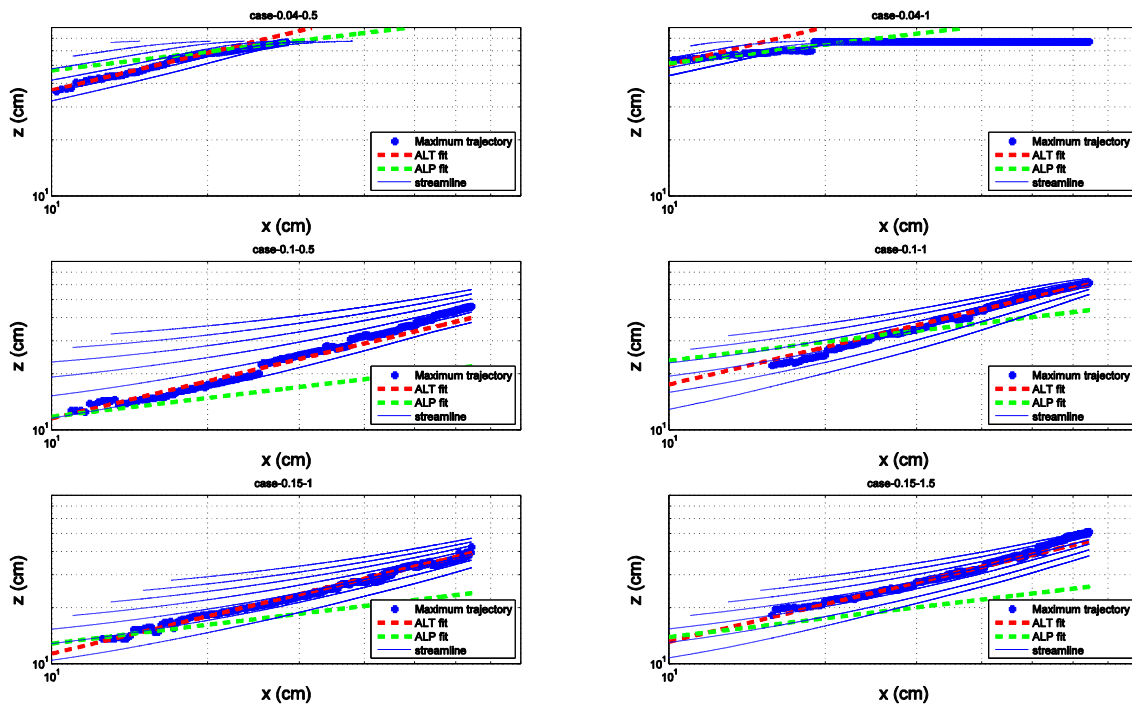
Figure 13. Comparison between the slopes of trajectories of separated continuous phase and asymptotic power laws of the advected line puffs and line thermals

To further verify the asymptotic behavior of the separated plume, we found the visual centerline of the dye distribution using the instantaneous images from experiments. The images were post processed to find the separated phase's upper and lower boundaries and the centerline as the midpoint. However, it should be noted that

39

the centerline identified in our study is different from previous studies because of the fact that we illuminate the center plane by the laser and the lobes of the counter rotating vortex are off this plane and in general would not pass through the laser. Meanwhile, they occasionally pass through the laser and can be seen as intermittent dye patches, which we neglected. Figure 14 presents an instantaneous image illustrating this procedure. Red lines show the centerline we defined from the boundaries that are displayed by the blue line.
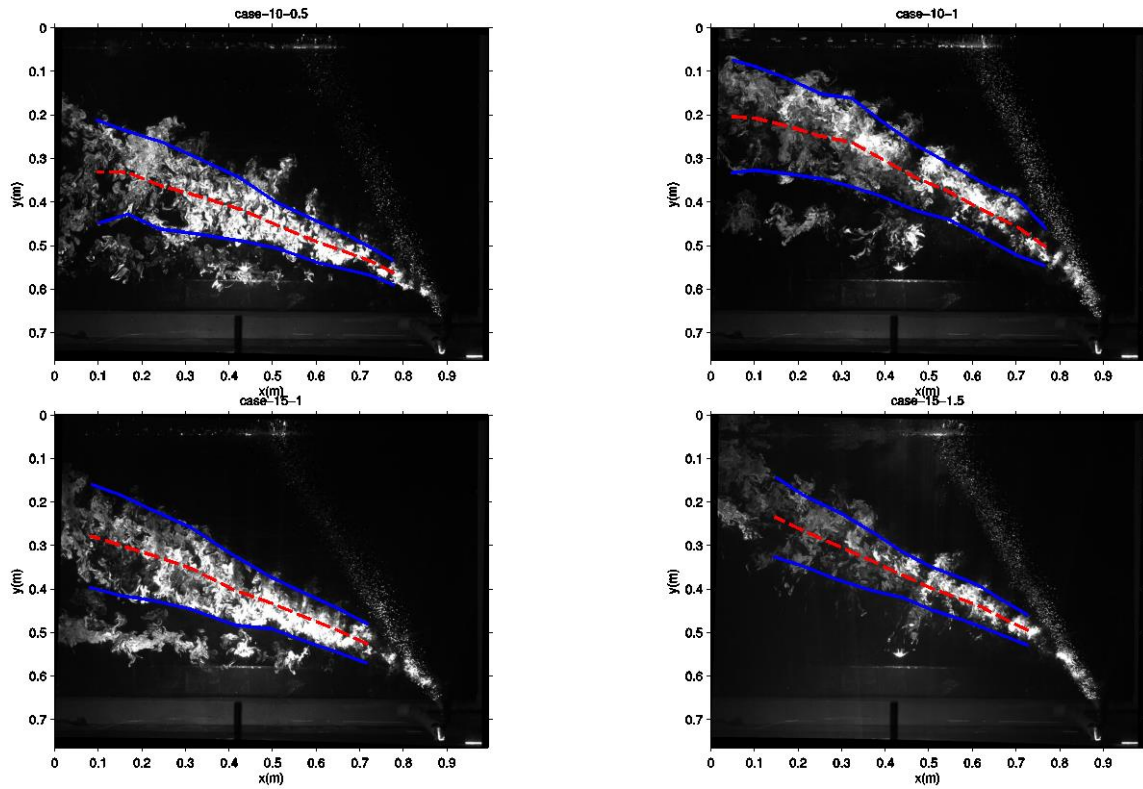
Figure 14. Experiments showing bubble plumes in crossflows. Red dashed lines show the identified centerline in the center plane dye distribution

Figure 15 presents the comparison between the slopes of the center dye distribution centerline and the asymptotic power laws. Similar to the behavior of the

velocity data, the centerline trajectories appear to deviate from ALP and follow the 2/3 power law of the ALT. This behavior is explained by the fact that the separated phase is in a vertically advecting frame of reference, where all the fluid above the separated plume is experiencing the vertical velocity resulting from the vertical momentum it acquire while passing through the bubble curtain; whereas, in a single phase plume or jet in a crossflow, all the streamlines above the buoyant jet are flat until they intersect the plume.
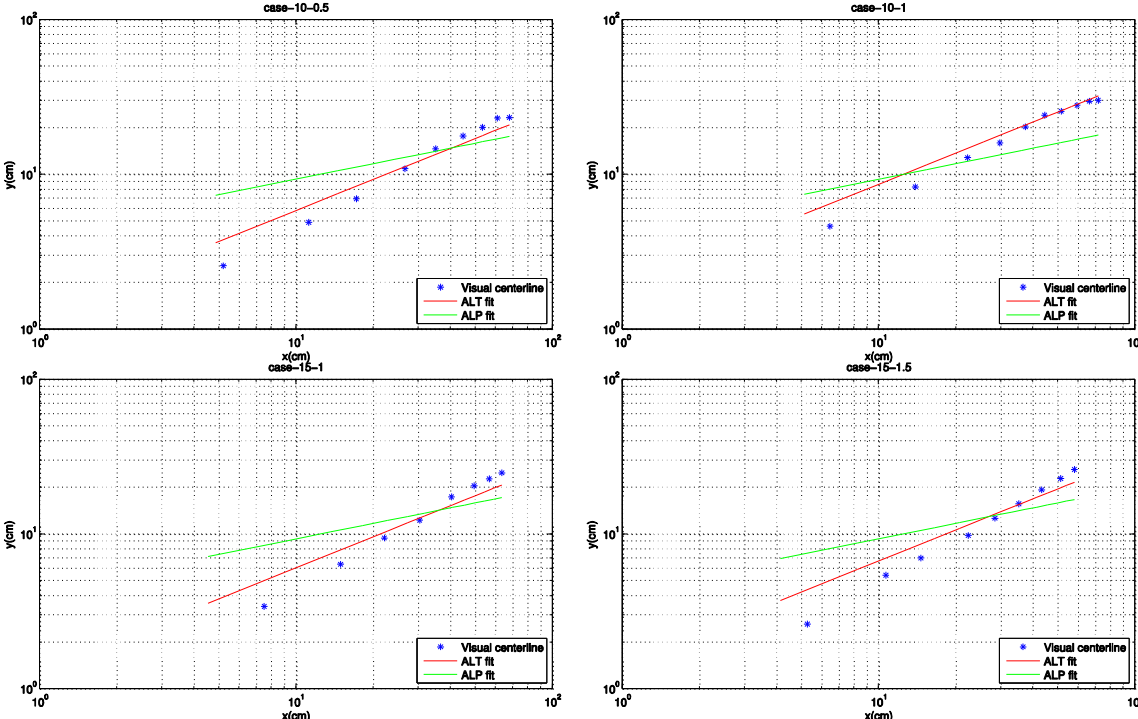
Figure 15. Visual centerline trajectories and their asymptotic fits

Since integral plume models predict the trajectory of the maximum velocity without knowledge of the vertical velocity in the wake above the separated plume, these results suggest that trajectories from jet models after bubble separation may under-

41

predict the rise. The data conform better to the 2/3 slop of the ALT most likely due to the upward velocity of fluid separated above the separation height. This fluid presents a background flow field that would be ignored in a single jet integral model. Hence, it is important to predict the magnitude of the vertical velocity in the wake of a bubble plume above the separation height. In addition, these data are helpful to CFD modelers, who may be able to validate to the results in this region of the flow where self-similarity is not valid.

2.5.3.   *Vertical velocities*

Measured time averaged velocity field information of bubble plume and its wake in crossflow have been shown in Figure 16 for different cases. Velocity vectors are overlaid with the color contour plots of the vertical components of velocity to better quantify and map the vertically-accelerated fluid. These figures show only 4% of the measured velocity vectors for clarity; warmer colors represent the region of upward flow, and solid black lines identify regions that contain bubbles. As similarly reported by Manasseh et al. (1998) and Socolofsky and Adams (2002) the bubble plume approximately follows a straight line downstream of the injection location. Persistent vertical velocity components in the bubble-column and the wake of the bubble column is evident in each case. As noted earlier, crossflow velocity continuously streams the flow to the bubble column where the bubbles impart a vertical kinematic momentum flux to the flow; afterwards, the water leaves the bubble plume carrying the vertical momentum gained from the bubble column, and this process leads to a vertical motion downstream which is shown in the figure by the warm colors. The induced vertical motion is more

significant for cases with weaker crossflow and larger bubble flow rates, hence, longer

contact time between the bubbles and water. Also, for weak crossflow cases, the

entrainment capture zone extends over the whole water column, resulting in no separated

plume. As the crossflow gets stronger and the bubble flow rate decreases, vertical

momentum spreads over a larger region above the separated plume and decreases value.
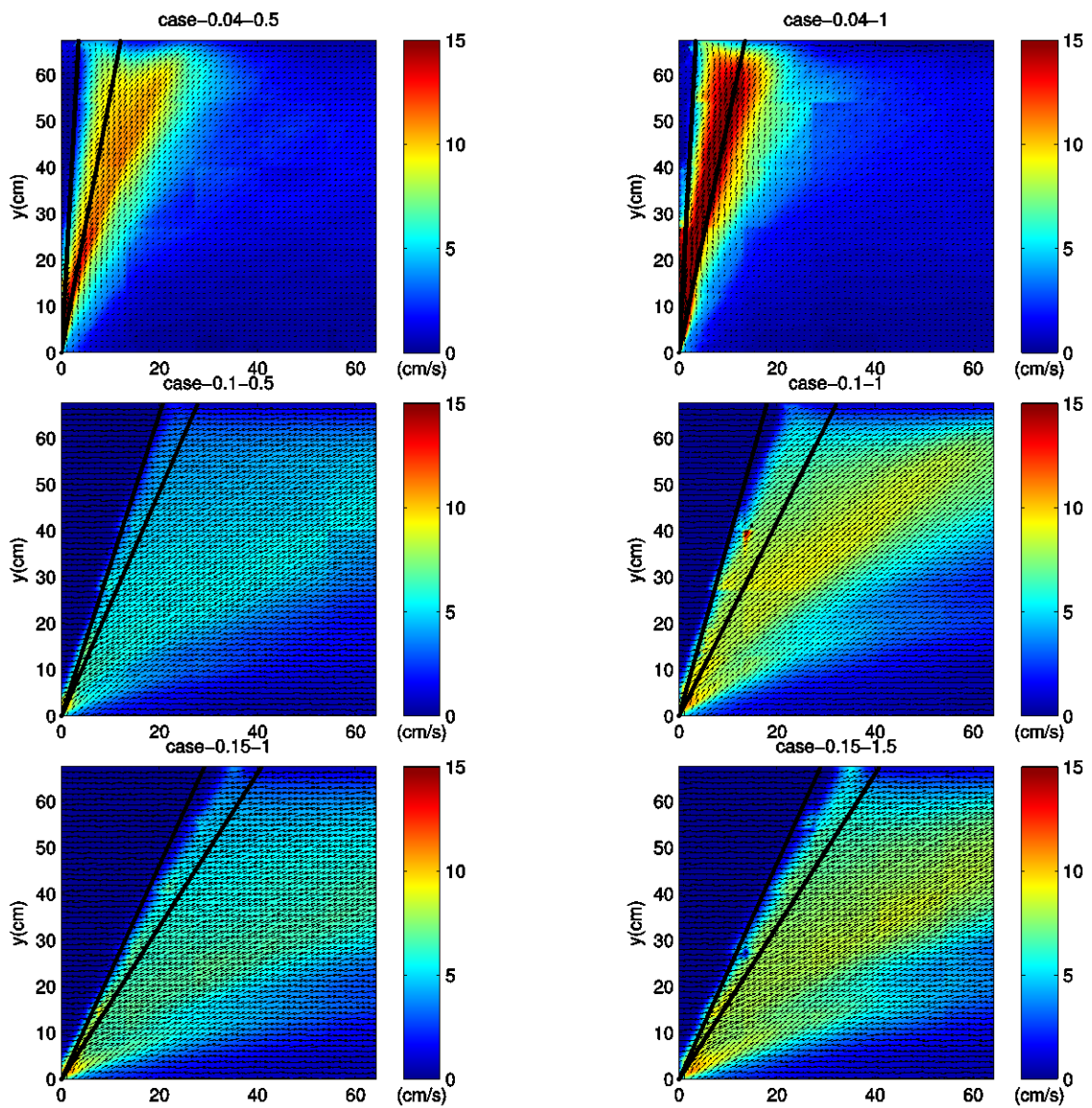
Figure 16. Velocity vector fields overlaid on the color contours of vertical component of velocity

To better exemplify how the vertical velocity profiles look at different heights for different cases, vertical velocity profiles measured at four different heights above the diffuser are shown in Figure 17 for cases (0.04-1) –with largest separation height-, (0.1-1) – lowest separation height-, and (0.15-1). In the weak crossflow case, the plume width is relatively narrow and peak velocity decay can be observed along the plume centerline as the plume width grows with height. On the other hand, for the strong crossflow cases with smaller separation height, vertically-accelerated flow is experienced by the whole wake region, and the PIV field obtained does not extend far enough downstream to see the return to zero vertical velocity.
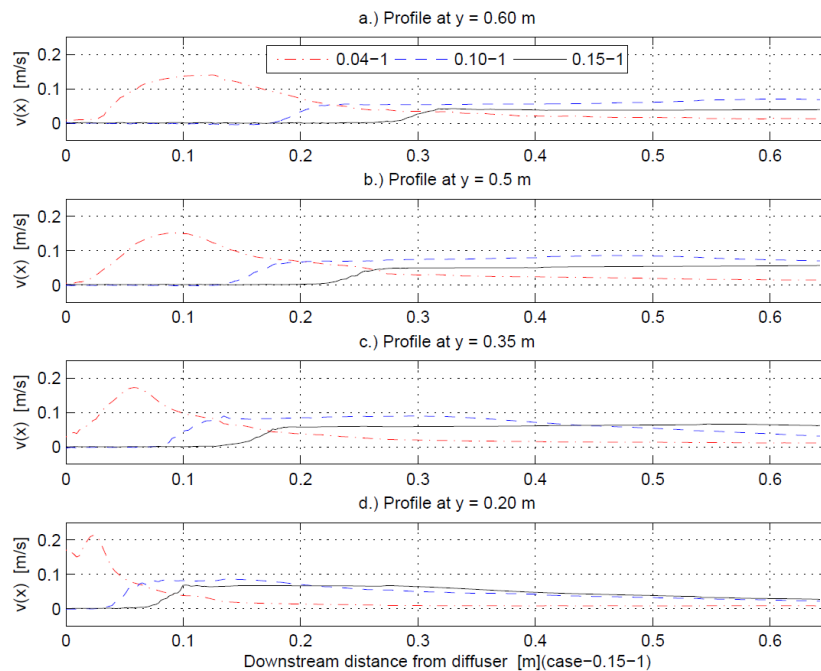
Figure 17. Vertical velocity profiles for 3 different crossflow and 1.0 l/min bubble flow rate

The significant region of vertically-accelerated flow in the plume wake was first reported by (Hugi, 1993). He showed that the crossflow appears to significantly amplify

the overall vertical flux induced by a bubble plume, even though the upward velocities are smaller than in stagnant water. He viewed the region of vertically-accelerated flow in the plume as a wake behind an upwardly-rising bubble column. In the case of extreme crossflow, the bubble column bends close to the horizontal and rises as a line thermal, with a vertical wake throughout the region below the rising bubble column. Based on this definition, (Hugi, 1993) defined a new coordinate *y'* as the vertical distance between a given point y and the centerline of the bubble column y_c. In his analysis, the centerline is given solely by the rise velocity of the bubbles, so that

$$y_c = \frac{u_s x}{u_\infty}$$

(5)

(Hugi, 1993) assumed y_c value to be a relevant coordinate even if it corresponds to a location above the water surface. Likewise, he obtained another length scale similar to the characteristic plume length scale in the absence of stratification ($D = \frac{gQ_g}{4\pi\alpha^2 u_s^3}$), where he used crossflow velocity and vertical component of the velocity in the denominator yielding

$$D_h = \frac{B}{u_\infty v^2}$$

(6)

He attempted to collapse the velocity profile data in the wake of a bubble plume using these two coordinates. The top plot in Figure 18 presents velocity profiles obtained at $y = 0.545$ m for his experiments. However, the drawback of this parameter space is that it remains dimensional and height dependent on the vertical location above the diffuser where the profiles were obtained. The bottom plot in Figure 18 presents velocity

45

profiles at $z/h_s = 1.2$ for each experiment in Table 1 using a similar parameter space as Hugi's. Velocity profile data in this figure seems to collapse quite well for the strong cases where crossflow velocity can better approximate the line thermal and agreement is less for the weak crossflow.
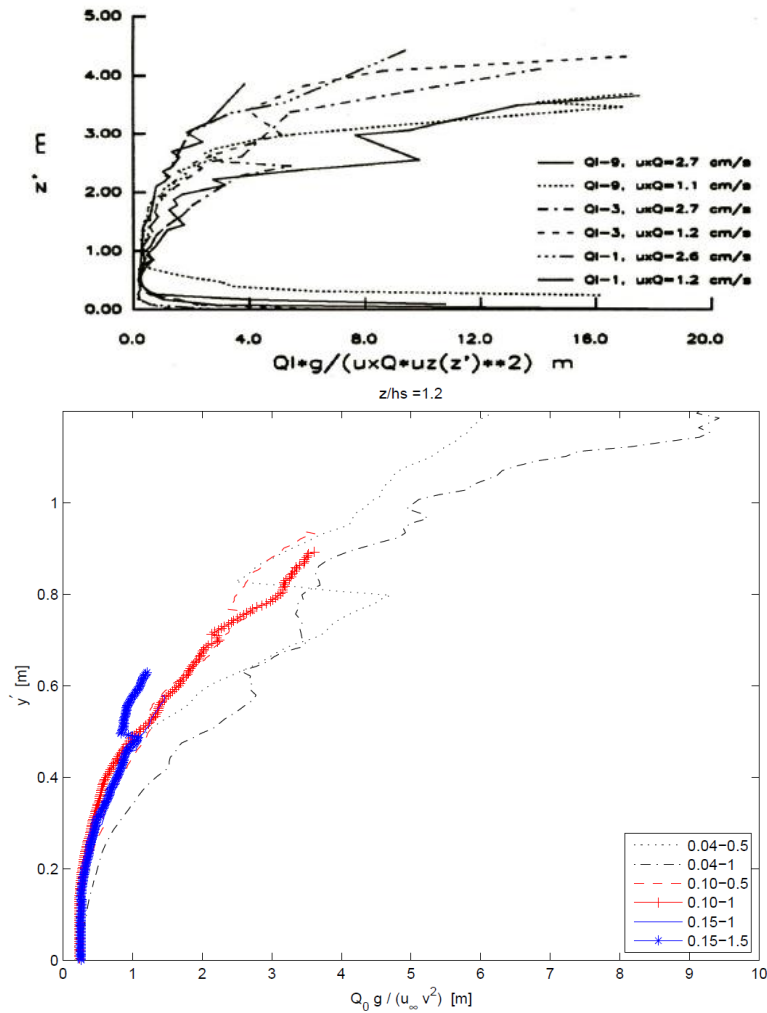
Figure 18. Top plot: Velocity profiles obtained at $y = 0.545$ as measured by Hugi, (1993), adopted from (Hugi, 1993) . Bottom plot: Plot of the vertical velocity component in the modified coordinate system, reprinted from Hugi, (1993). The profiles lines are for each experiment based on the velocity profile at $h_s/z = 1.2$ obtained at the corresponding z above the diffuser.

2.5.4.   Trajectories of water ejected at all levels and predictions of dynamics above hs

To provide a better understanding of the transport above the separation height we present the observations of the fluid that enters the plume at different heights. Figure 19 depicts the path of the streamlines entering the bubble plume at different heights and eventually released by the plume in three representative experiments with different crossflows and same bubble flow rate. As shown before, water enters the plume horizontally and leaves the plume with an increased vertical velocity. Vertical velocity of water inside the plume decreases toward the water surface due to the boundary interaction, and should be ignored. Close to the diffuser, trajectories are steeper than those closer to the water surface where they are ejected with smaller ejection velocities. As is evidenced in Figure 19, the streamlines remain straight and parallel; this further demonstrates that the vertical velocity which will be translated to the upward flow in the wake, can keep its vertical momentum approaching the water surface.

As the crossflow gets stronger, entrained water leaves the plume and gets ejected rather than being contained and transported inside the plume. In these experiments, the average vertical transport after the separation height is 3.6 cm for case (0.10, 1) and 2.3 cm for case (0.15,1). Prediction of the vertical transport and the residence time of the entrained water in the plume is of interest for applications such as lake aeration. As the residence time increases, oxygen in air bubbles have more time to dissolve into flowing water through the air-water interface of bubbles. Hence, residence time can impact the concentration of dissolved gases downstream.
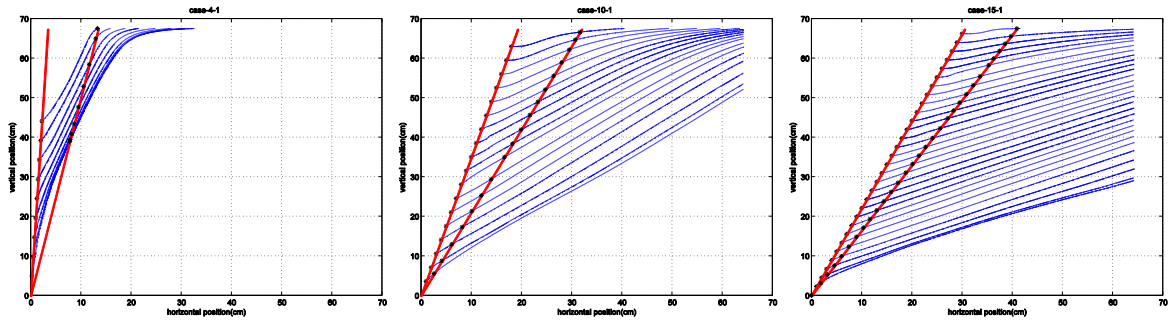
Figure 19. Trajectories of water ejected at different levels for same bubble flow rate and different crossflows, at 1NL/min air flux

Presently, available integral plume models are capable of predicting the velocity of the bubble plume's continuous phase and discrete phase until the separation height after which the bubbles are considered to be advected on their own buoyant velocities and the ambient currents. As shown in Figure 19, our observations illustrate that streamlines are deflected vertically due to the bubbles. Here we present a conceptual model to predict the vertical velocity responsible for this deflection. We assume at any level above the separation height, the flux of the flow across the bubbles are equal, i.e. the flux of the ejected water from the leeward side is equal to the flux of the entrained water from the windward side, Further, we assume bubbles impart the vertical velocity on the fluid inside the bubble plume by momentum transfer balanced by their drag (or, equivalently, their buoyancy). This assumption is verified by the observation of the parallel streamlines above the separation heights (Figure 19), which indicates that the plume is at a quasi-steady state of losing materials at the same rate as they are coming in. Thus, the bubble plume is considered to be "exhausted", implying that all the entrained fluid is ejected from the plume and does not stay in the plume.

To develop a predictive model, we consider a control volume of water with the height of dz and radius b and a horizontal velocity equal to the ambient velocity, which crosses a bubble plume as shown in Figure 20.
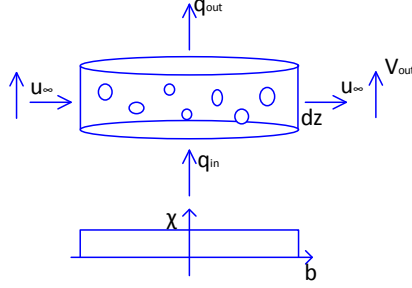
Figure 20. Schematic of control volume considered in exhausted plume analysis

While passing through the bubble plume, this control volume experiences the buoyancy or drag force of the bubbles, and we assume it exits without any changes in its horizontal velocity, but with an increased vertical momentum as a result of the buoyant force. Conservation of momentum over this control volume yields a relationship for this vertical velocity. The simplified force-momentum conservation can be written as:

$$V_{out} * \left(u_\infty * (2bdz)\right) - V_{in} * \left(u_\infty * (2bdz)\right) = \chi \pi b^2 dz \frac{\Delta \rho}{\rho} \qquad (7)$$

where V_{out} is the vertical velocity upon existing the bubble plume, and V_{in} is the vertical velocity before entering the bubble plume, which is zero. The right hand is essentially the buoyancy force exerted from the bubbles, where χ is the void fraction, as is defined in (Socolofsky et al., 2008) as $\chi = \frac{\dot{m}_p}{\rho_p(\pi b^2(u_s+u_p))}$ where u_p is the vertical velocity at the middle of the bubble plume. Substituting χ and $u_p = \frac{1}{2} V_{out}$, as we assume a linear velocity distribution in the bubble plume due to the nearly uniform void fraction

observed in bubble plumes (Seol and Socolofsky, 2008b), the solution of equation (8) yields the vertical velocity of the continuous phase as

$$v_{out} = A*(-u_s + \sqrt{u_s^2 + \frac{\dot{m}_p(\rho - \rho_p)g}{\rho\rho_p u_\infty b}}\ )$$

(8)

where A is the coefficient found to be 1.159 from linear regression between the model and the measurement.

Figure 21 compares the model results with the experiment data at the downstream bubble column edge. It should be noted that data are taken above the separation height and the surface effects have been identified from the velocity gradient at the surface and excluded from the comparison data for each case. In Figure 21, the highest velocities belong to the case with the weakest crossflow and correspond to lower elevations in the plume. To quantify the difference between the predicted and observed vertical velocities, we use the mean absolute percentage error (MAPE) which is a measure of predicting the accuracy in statistics. MAPE is defined as

$$MAPE = \frac{1}{n}\sum_{t=1}^{n}\left|\frac{M_t - P_t}{M_t}\right|$$ where M_t is the measured value and P_t is the predicted value.

MAPE results are shown in the figure legend for each case and indicate that the agreement is better than 20% deviation in all cases between this simple model and the experimental results.
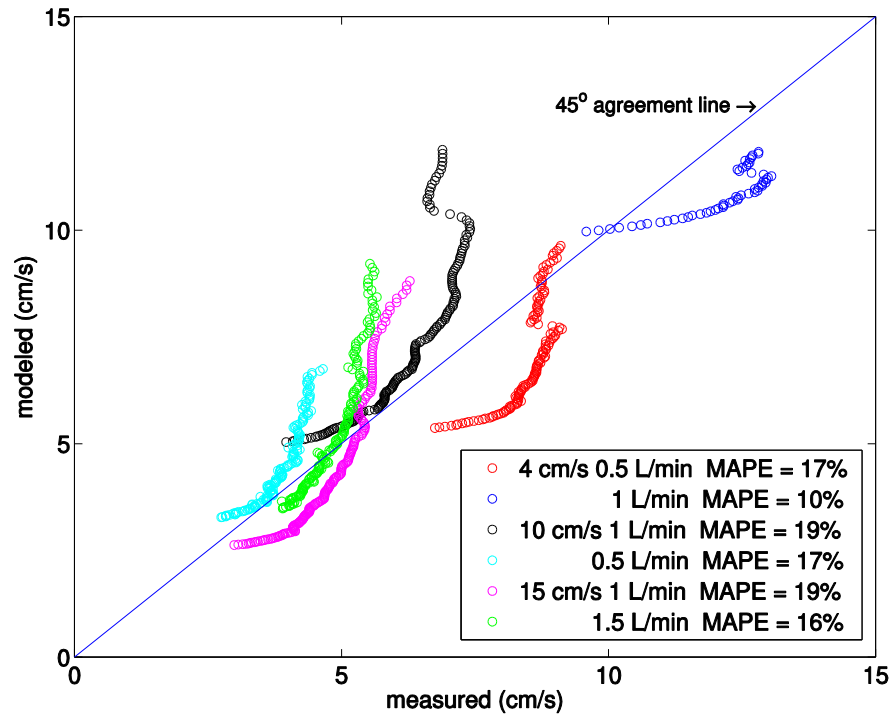
Figure 21. Comparison between modeled and measured vertical velocities in exhausted plume region of flow

2. 6.   Conclusion

This paper presented laboratory experiments of bubble plumes in uniform crossflows. Twenty-five fields of views were used to cover the whole field of interest in the plume center plane starting from the center of bubble diffuser and mapping an area of 65.5cm X 68.5cm. Image processing techniques were applied to eliminate bubble signatures. The PIV technique was used to quantify the whole velocity field of the continuous phase, where recirculation current was generated by a forced current. Further measurements include dye visualization using LIF in which crossflow was simulated using a towed source. The important conclusions from these measurements are summarized as follows:

51

- Comparison between the results from two different sets of experiments which simulate ambient current in different ways supported the analogy of the towed plume to that of a real current and showed that the towed source in stagnant water can represent a fixed source in crossflow.

- Fluid exiting the plume has vertical momentum throughout the water depth gained from the plume's buoyancy force.

- Observation showed that no secondary bubble plume would form above the separation height and bubble plumes are considered to be "exhausted" of entrainment, in other words, in this region, plume is at the steady state of losing materials at the same rate as they are coming in.

- Quantified trajectories of the separated continuous phase deviates from the scaling power laws for the advected line puff, which is shown to be experienced by the trajectories of pure jets in crossflows; this is due to the induced vertical velocities that exist in the wake flow field above the separation height. This will result in the under prediction of the rise for the separated plume given by integral models such as Socolofsky and Adams (2002)

- A conceptual model based on the simplified force-momentum conservation was developed to predict the vertical velocities induced by the plume above the separation height. The simple model results correlates well with our experimental observations.

3. TURBULENT PROPERTIES OF A WAKE BEHIND A ROUND BUBBLE PLUME IN CROSSFLOWS

3. 1.   Overview

This study presents results from the analysis of the velocity field and turbulence statistics measured downstream of a round bubble plume in the presence of crossflows. Experiments were conducted in a glass-walled flume equipped with a recirculation system to generate the background flow. The two-dimensional Particle Image Velocimetry method was used to measure the velocity field and turbulence intensities in the wake of the bubble plume. Profiles of turbulence intensities and Reynolds stresses are presented, and the effects of bubbles on turbulence generation are investigated experimentally. From the profiles of mean velocity and second order turbulence statistics, we found the following. Existence of bubbles affects the mean flow, generating an upward mean velocity and augmenting the turbulent intensity. Mean flow kinetic energy of the wake was found to be affected by the bubble injection rate and crossflow velocity. The wake turbulence is anisotropic with anisotropy being increased by increasing the cross flow and bubble flow rate. Finally, we observed that the vortex pair structure of the separated plume can be detected by identifying the location of maximum Reynolds stresses.

3. 2.   Introduction

Bubble plumes are highly turbulent flows in nature which can result in efficient mixing in many applications. When bubble plumes are exposed to crossflow, separation

may occur, where fluid entrained at the base of the bubble plume may separate from the trajectory of the bubble column at a certain separation height, depending on the plume and crossflow parameters (Socolofsky and Adams, 2002b). A sample experimental image showing the separation height is given in Figure 22. Figure 22 also illustrates several other features of the flow field for a bubble plume in a moving ambient, including the separated bubbles, separated entrained plume in the downstream wake, and the wake region above the separation height. In this study, we investigate the turbulence nature of the flow field throughout the wake. Understanding the mixing processes and the flow induced by a bubble plume in crossflow is of importance for the design and optimization of many of their applications. For example, lake destratification and aeration systems that use bubble plumes are open to the questions of to what extent the bubble plume mixes the stratified ambient and enriches the oxygen concentration. Although turbulence properties in bubble plumes have been studied in quiescent conditions, less attention has been paid to the turbulence properties of the induced flow in the presence of the crossflows. The purpose of the present work is to account for this need by using velocity data obtained from a set of Particle Image Velocitmetry experiments. These results are important to understand the fundamental turbulent nature of the wake and can be used for verification of modeling approaches in CFD codes for bubble plume analysis.
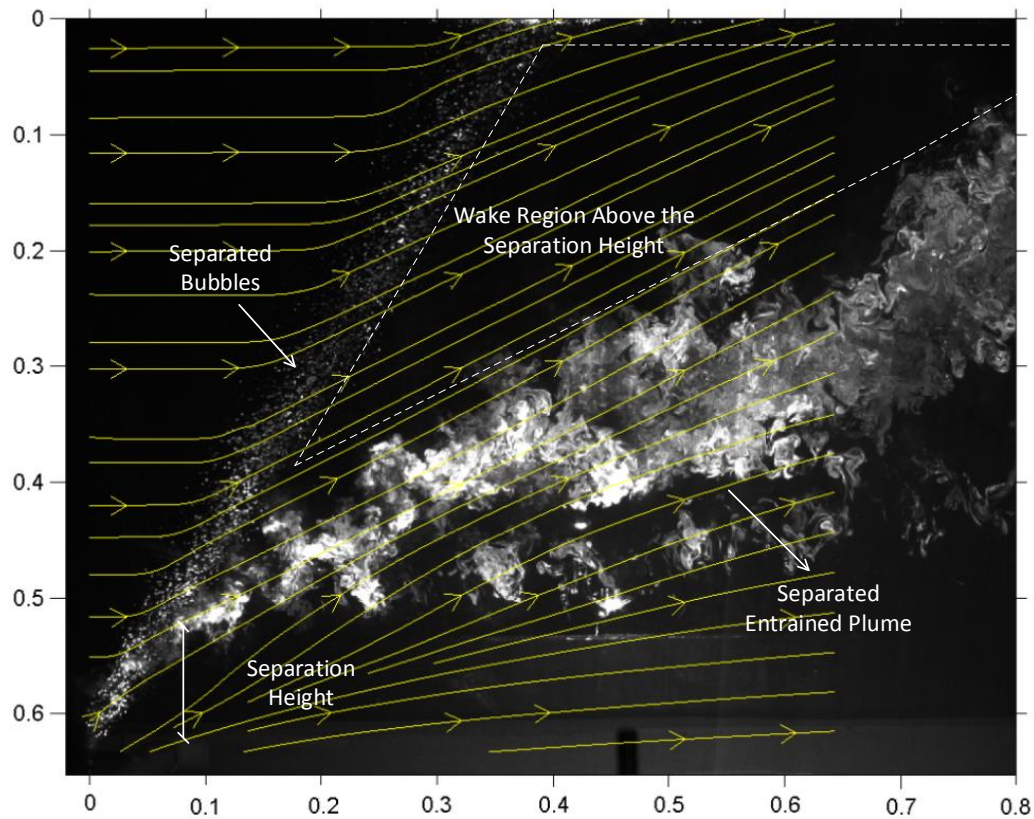
Figure 22. Definition image for a bubble plume in crossflow

Turbulence properties in bubble plumes in quiescent conditions have been measured in several studies. (Tekeli and Maxwell, 1978) did one of the first works and reported values of turbulence intensities in bubble plume in a medium-scale, bubble-plume facility. (Simiano et al., 2006) used PIV methods and reported average turbulent intensities and mean turbulent stresses within a bubble plume near its source. (Bryant et al., 2009b) applied PIV methods to quantify plume-scale turbulence properties in a bubble plume farther from the source, into the asymptotic regime of the plume dynamics. (Bryant et al., 2009b) observed that the presence of bubbles in the flow can modulate the turbulent energy spectrum in the inertial subrange, which had been

observed previously for point-wise measurements (e.g., Lance and Bataille, 1991; Rensen et al., 2005). (Bryant et al., 2009b) also found the greatest vortex size and energy density in the shear layers at the edge of the round plume, indicating that shear instability is the dominant process of large-scale turbulent and coherent structure generation in pure bubble plumes. These studies provide important insight on the turbulence structures inside and outside the bubble plumes in the quiescent condition. However, they did not investigate the turbulence properties of the flow in the wake downstream of a bubble column in a moving environment.

Turbulence in obstructed flows has been studied in open channels. (Nepf, 1999; Nepf et al., 1997) performed laboratory experiments and measured turbulence intensities in presence of vegetation and showed that vegetation affects the turbulence intensity through converting mean kinetic energy into turbulent kinetic energy linked to the wake generation behind plant stems. The model they proposed for this effect predicts that turbulence intensity increases with the introduction of sparse vegetation but then decreases with increasing population density as mean flow speed becomes reduced. Bubbly flow may be similar to the flow through stems; in a frame of reference moving with the bubbles, bubbles resemble the stems, except that they are three dimensional. Hence, similar effects may be observed in the bubble plume wake.

To add insights to the turbulent properties and scales in the bubble plume wake in the presence of crossflow and to investigate how the turbulence behaves in the wake region, this paper applies PIV to identify variance structure of velocities including mean turbulent stresses and turbulent intensities in the bubble plume wake in the presence of a

current. The laboratory and data processing methods are reported in section 3.3, which details the designed experimental setup and the data analysis methods. Section 3.4 presents the results section of the measured PIV data to show the instantaneous and turbulent flow properties. The summary and conclusions are presented in section 3.5.

3. 3.   Laboratory experiments

3.3.1   *Experiment setup*

The experiments were conducted in a glass-walled flume 35 m long by 0.9 m wide and 1.2 m deep in the Fluid Dynamics Laboratory of the Zachry Department of Civil Engineering at Texas A&M University. The tank is equipped with a recirculation pump system to simulate different ambient currents. In order to destroy the jet structure of the inflow at the flume entrance, an array of bricks was placed immediately after the inflow (Ghisalberti and Nepf (2002)). A homogeneous grid of porous plates was then used to smooth the velocity profile as suggested by Stoker (1946). Flow straighteners made out of PVC pipes with a diameter of 2.54cm and length of 70cm were used to eliminate the large scale turbulence and secondary currents. The bubble plume was located 19 times the water depth downstream of the flow straightener. To generate the bubble plume, a 1.4 cm -diameter aquarium airstone was used at a height of 14.5cm above the flume bottom.

We chose the bubble flow rates as $Qo = 0.5$, 1 and 1.5NL/min to match the previous experiments with zero crossflow (D.-G. Seol et al., 2007). The bubble flow rates at standard pressure and temperature were monitored by a gas mass flowmeter. The

57

generated air bubbles had a median diameter d_{50} of 2.4 mm as measured by Lai and

Socolofsky (2015) in a similar setup, with a corresponding slip velocity of 24 cm/s (Clift

et al., 2005). Three different ambient currents (u_∞), i.e. 4, 10 and 15 cm/s were simulated

in a way that combined with the bubble flow rates, could span a range of separation

heights (i.e., no separation, weak separation, and strong separation). Table 2 summarizes

the full range of experimental conditions measured in this section.

Table 2. Parameters of the crossflow experiments

Crossflow Velocity, u_∞ (m/s)	Water Depth, H (m)	Bubble Flow rate, Q_o (Nl/min)	B (m^4/s^3)	Slip Velocity, u_s(m/s)	H/D	H/h_s
0.04	0.68	0	0	-	-	
		0.5	7.663e-5	0.17	3.54	2.43
		1	0.0001533	0.18	2.1	1.36
		1.5	0.0002299	0.20	1.92	1.13
0.1	0.68	0	0	-	-	
		0.5	7.663e-5	0.17	3.54	5.23
		1	0.0001533	0.18	2.1	3.1
0.15	0.68	-	0	-	-	
		1	0.0001533	0.18	2.1	4.25
		1.5	0.0002299	0.20	1.92	3.58

The center plane of the bubble plume was illuminated by a laser sheet formed

from a continuous Argon-ion laser (Spectra- Physics) and associated optics. A mirror

was placed on the flume bottom to make the horizontal laser sheet vertical. The flume

water was seeded with neutrally buoyant homopolymer polyamide particles

(manufactured by Vestonic) of mean diameter 56 micron and of specific gravity 1.03.

Flow images were captured by a high speed Phantom camera mounted on a

three-dimensional traverse and positioned perpendicularly to the light sheet. The camera

frame rate was 200Hz and the exposure time was 300 microseconds, capturing upto 2000 frames per measurement burst (limited by physical RAM of the camera). The resolution of the camera was 1024×1024 pixels with a gray scale dynamic range of 10 bits. In order to cover the whole field of interest, 25 fields of view (FOV) were used starting from the center of the bubble diffuser. Each FOV had a dimension of 15×15 cm with 1.5 cm overlap. Figure 23 shows a schematic of the raster of camera FOVs and the reconstruction of the grid plate image captured from each camera FOV after geometric correction. Measurements commenced in FOV(1,1) and followed an S-pattern through FOV(5,5). The light patches surrounding each individual image in the reconstruction indicate the overlap for each camera FOV. Note that the last column of frames had an overlap of 5cm due to the limitation on the maximum range of the traverse.
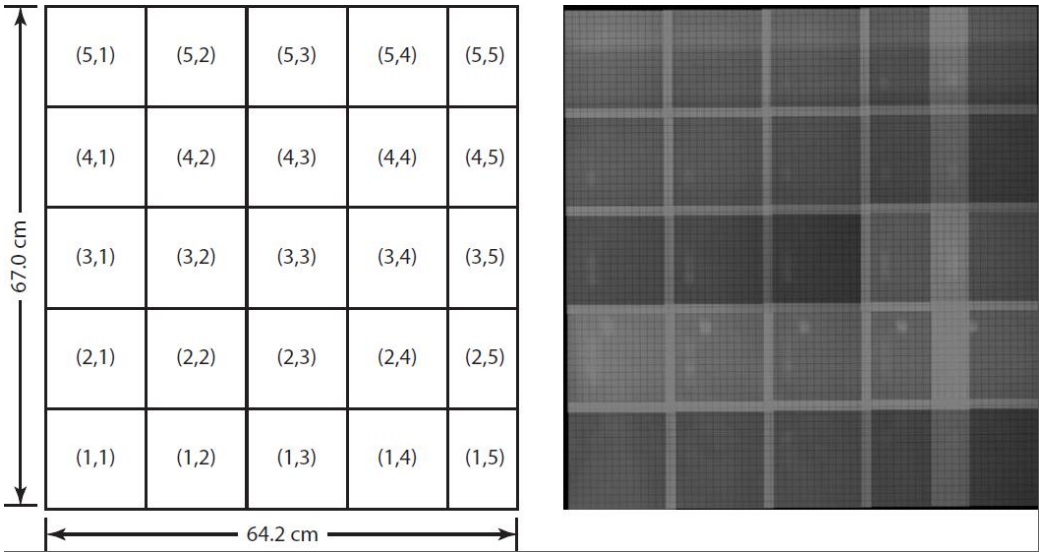
Figure 23. Layout of the FOVs showing the full measurement plane (64.2 * 67.0 cm). The left image shows the naming convention for each FOV (e.g., (1, 1) for the first row and the first column), and the right image shows the corrected images of the calibration grid plate.

Image sequences for the PIV analysis were acquired in 2000-image bundles, each representing 10 seconds of experimental run time. To get a stable mean velocity, experiments were repeated three times at each FOV, which resulted in 30 seconds of data, or 6015 images at each flow rate and crossflow combination. Hence, PIV sequences are neither synoptic from FOV to FOV nor are the data contiguous over the whole 30 s at each measurement point; therefore, we rebuilt the flow field from statistical averages of the results, including mean velocity, turbulence intensity, and Reynolds tresses. Figure 24 shows the schematic setup of the experiments.
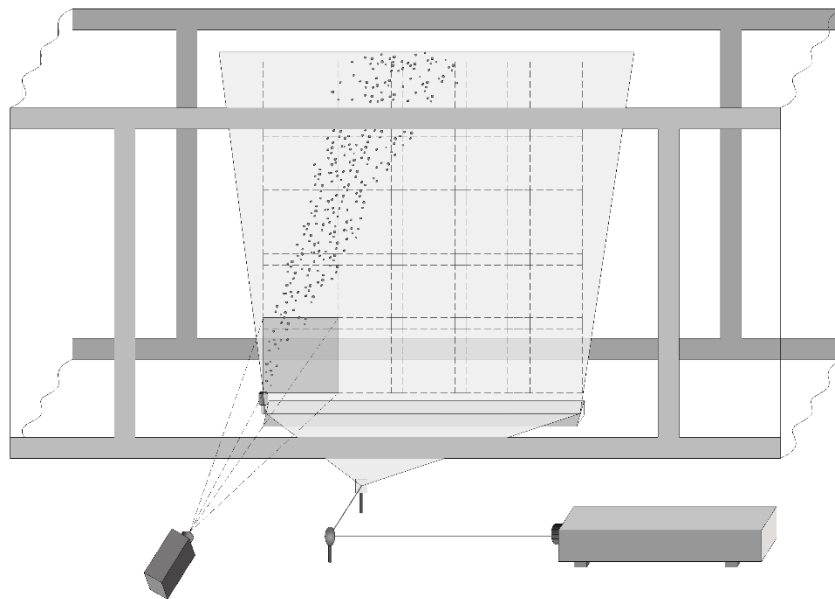
Figure 24. Schematic of the PIV setup

3.3.2   Image preprocessing

Bubble signatures were removed from the raw images before applying the PIV algorithm to calculate the continuous phase velocities using a size and brightness

discrimination method for separating the bubbles as previously explained in Section 2. Because of the removal of the bubbles, data at the plume core for each picture would be insufficient. This insufficiency is circumvented by time averaging over the total experiment duration of 30s, thereby obtaining the mean velocity inside the plume core. Also, the bubble region suppresses the amount of laser light passing through the bubbles; consequently, instantaneous and turbulence data are too noisy at the region upstream of the bubble column.

3.3.3   PIV analysis procedure

The LaVision Davis software package was used to perform the PIV processing and obtain the velocity vector field. Velocities were calculated from the regular cross-correlation PIV algorithm using a multiple pass interrogation window with 50% overlap. The iterations used an initial window size of 64 by 64 pixels and a final interrogation window size of 32 by 32 pixels, yielding a uniform vector grid of 2.3 by 2.3 mm. To remove the vectors that do not accurately represent the flow field, a median filter was applied to the resulting velocity field by comparing each vector to the root mean square of the 8 surrounding vectors. A sample of the resulting instantaneous velocity field for one camera FOV is shown in Figure 25.
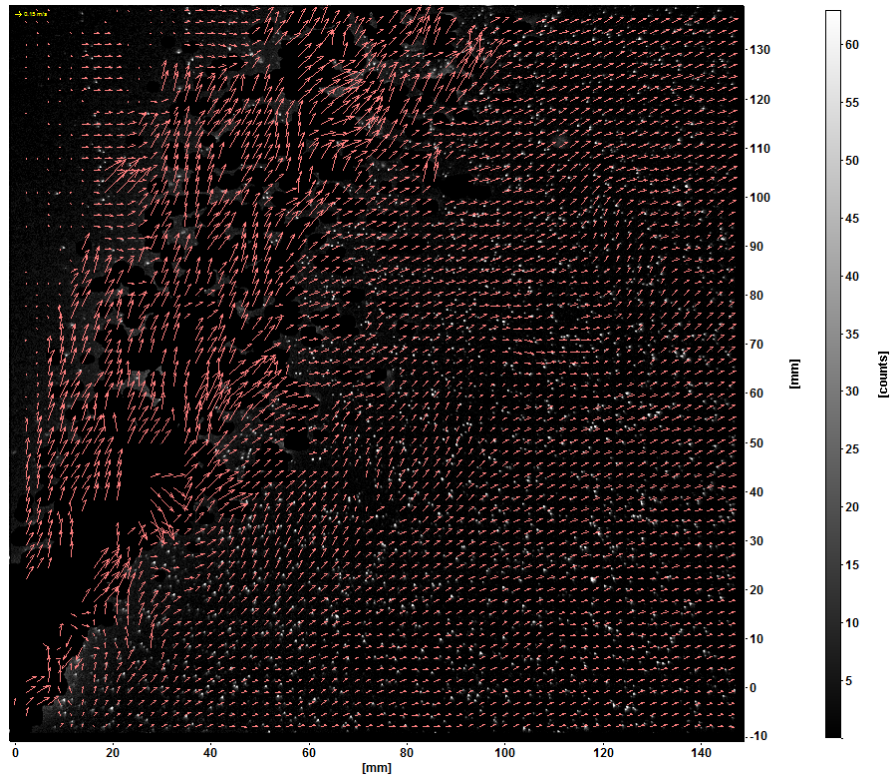
Figure 25. Instantaneous velocity field for FOV(1,1) for the PIV measurements of case 0.15-1.5

3. 4.   Results

The results presented in this section investigate mixing in the wake to shed light on the understanding of the role of bubbles in injecting turbulence in the wake region when crossflow is present.

3.4.1   Turbulent intensities

Turbulence intensity is computed from

$$i_t = \frac{\sqrt{\overline{u'^2} + \overline{v'^2}}}{|U|}$$

(9)

where u' and v' are the velocity fluctuations in the x and y directions, respectively and $|U|$ is the mean crossflow. The results shown in this section were obtained from ensemble averaging over 6015 instantaneous velocity measurements at each point. Figure 26 shows the turbulence intensity fields for different cases of crossflows and bubble flow rates. High values of t_i can be observed at the overlap region of PIV fields, which is an artifact of the PIV process due to its high uncertainty at the edges of each FOV. However, the trends are still significant and we did not remove this data even though the uncertainties are higher.

The observations show that turbulence intensities increase with increasing the bubble flow rate but then decrease with increasing the ambient current. The solid lines in the figure outline the bubble column. The thick plus signs show the trajectory of the maximum time-averaged velocity, which follows the upper third of the plume of entrained water that separates at the separation height (Rezvani and Socolofsky 2015, Socolofsky and Adams 2002). The regions of highest turbulence intensity are consistently below this trajectory line and correlate with the edges of the upward rising separated fluid in the wake (as identified in corresponding experiments using dye; (see Figure 22), indicating that the velocity shear between the bottom of the separated plume and the ambient exhibit the greatest turbulence intensities. Observations show that mixing is primarily within the plume generated by the rising bubbles where bubbles increase the turbulent intensity by an order of magnitude comparing to the case where there are no bubbles.

The graphs of turbulence intensity further show that before introducing the

bubbles (top row of Figure 26), there is a region with high turbulence intensity at the left

corner of the plot which is due to the separation caused by the diffuser structure. Note

that the flume bottom boundary layer is well below the region covered by these

measurements. In cases with no bubble plumes, turbulence intensity is negligible over

the flow field except for the diffuser structure affected region; hence, this is a low-

turbulence forced current.
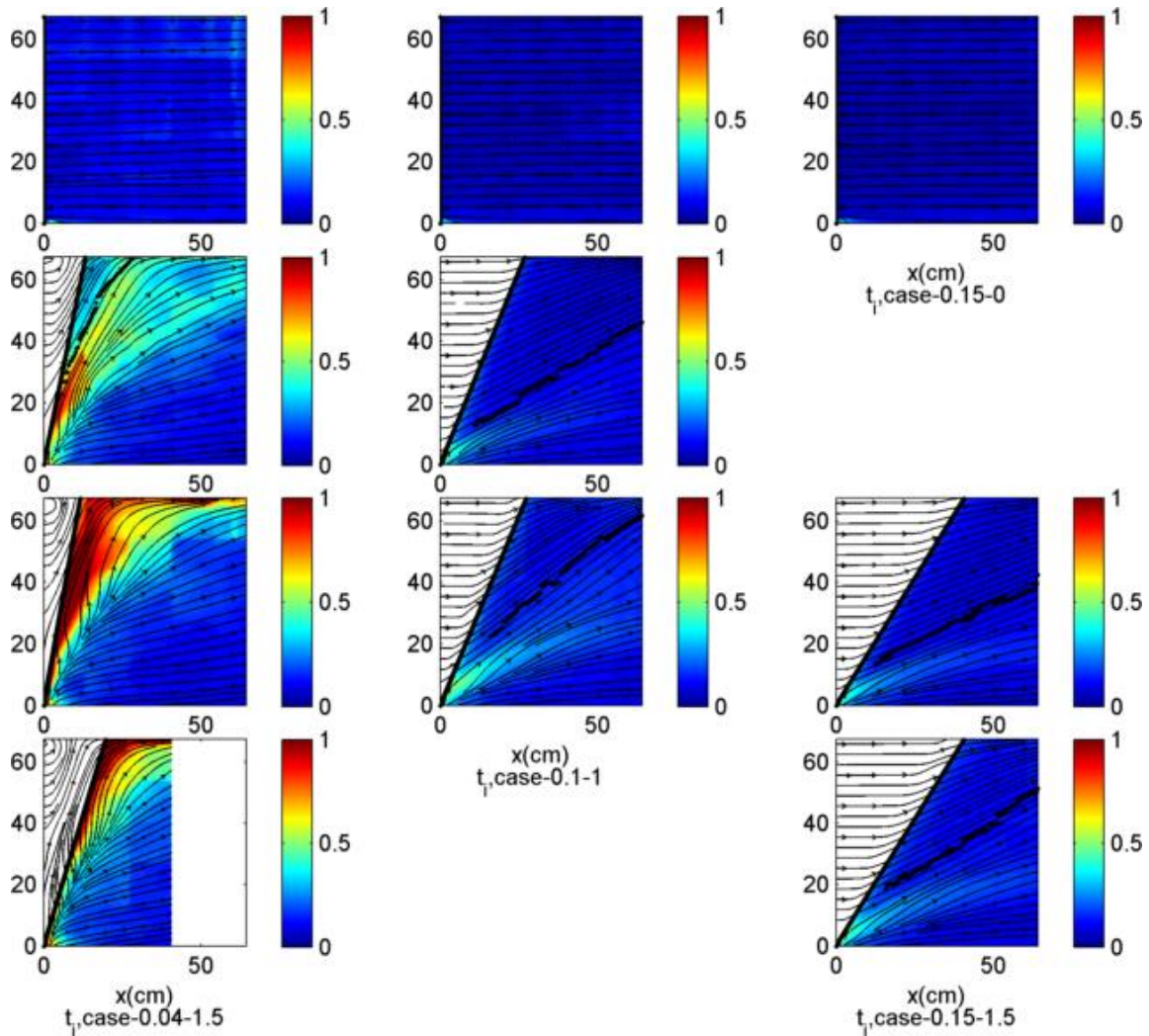
Figure 26. Plots of turbulence intensity for different cases of crossflow and bubble flow rate together with streamlines of the time average velocity, and trajectory of the maximum time average velocity.

Figure 27 compares vertical profiles of turbulence intensities at different current velocities and bubble flow rates and reveals the changes in the turbulence intensity at two non-dimensionilzed locations of $x/h_s = 2$ and $x/h_s = 2.5$. For this figure, the surface recirculation zone has been removed. For comparison, the vertical axis is normalized by the separation height for each case. As evident in the figure, the main shape of the profiles is similar across experiments using this axis scaling. In general, turbulence

intensity increases due to the introduction of the bubbles. As Q increases, the turbulence intensity increases due to the increased blockage by the bubbles, providing higher degree of bubble wakes. This observation is in agreement with similar measurements for the flow through vegetation, where (Nepf et al., 1997) observed enhanced turbulence intensity as the population density of vegetation increased. Meanwhile, average turbulence intensity decreases as the crossflow increases likely due to a reduced contact time between the crossflow and the bubble column. The profiles of the turbulence intensities also suggest that the flow consisted of two regions. Near the separation height $\frac{y}{h_s} = 1$, the turbulence intensity shows a maximum value. This region is associated with the separated plume of water entrained near the source and which has the longest contact time with the bubbles. Above and below this area, the turbulence intensity remains elevated as water must flow through the bubble column to enter the wake.
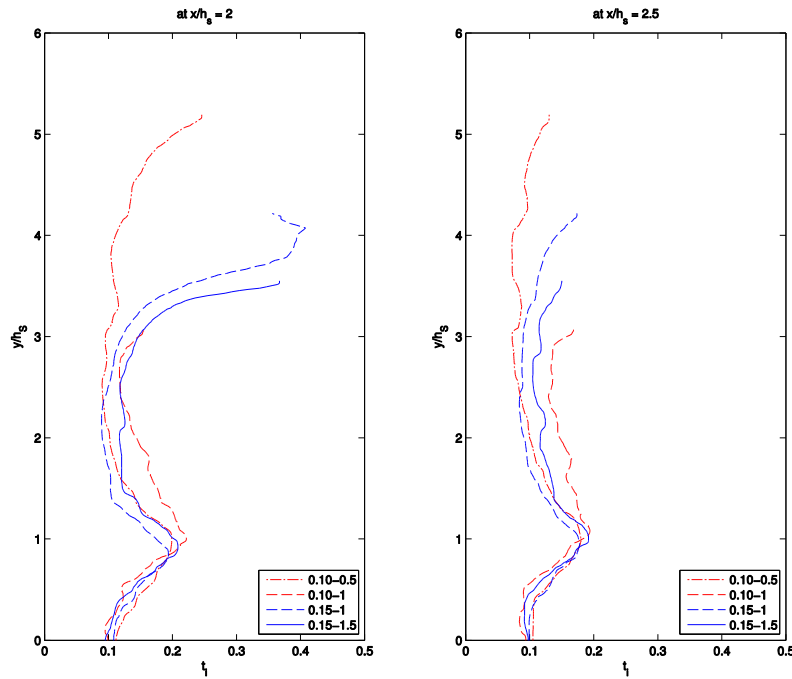
Figure 27. Vertical profiles of turbulence intensities at a) x/hs = 2 and b) x/hs = 2.5

3.4.2 Reynolds stresses

Reynolds stresses are understood as a source of turbulent transport and stirring, and based on the Reynolds analogy for mass transfer, higher mixing can be anticipated at locations of higher Reynolds stresses. Figure 28, Figure 29, and Figure 30 show the R_{uu}, R_{vv}, and R_{uv} components of the Reynolds Stresses, respectively, for different cases in this study. These plots show the clear shear-flow boundary between the upward-rising bubble plume, the separated plume fluid, and the wake flow outside the plume. For the case of weak separation, the shear-flow boundary is confined close to the bubble core, and for the cases with lower separation heights, this boundary flows with a mild angle into the downstream wake. By comparison to the wake structure, the regions of highest Reynolds stresses also lie on the lower boundary between the upward-rising separated plume and the background horizontal wake flow. It is also evident that throughout the

67

region of rising fluid in the downstream wake, mixing is enhanced, showing elevated

Reynolds stresses. Comparison between the horizontal and vertical components suggests

that agitation covers a wider area in the vertical fluctuations, suggesting there is a

linkage directly to the vertical bubble motion and bubble wakes.
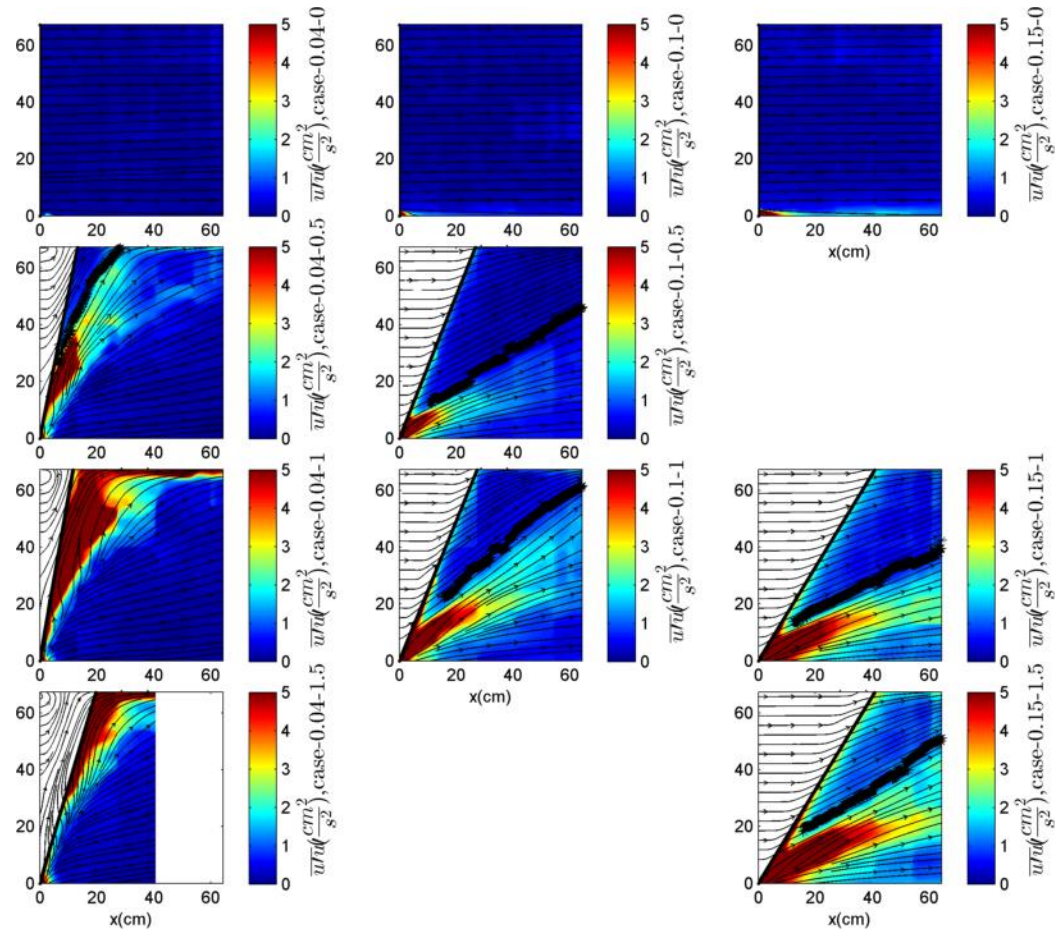
Figure 28. uu- Component of the kinematic Reynolds stresses together with the streamlines for the time average velocity field, and trajectory of the maximum time average velocity.
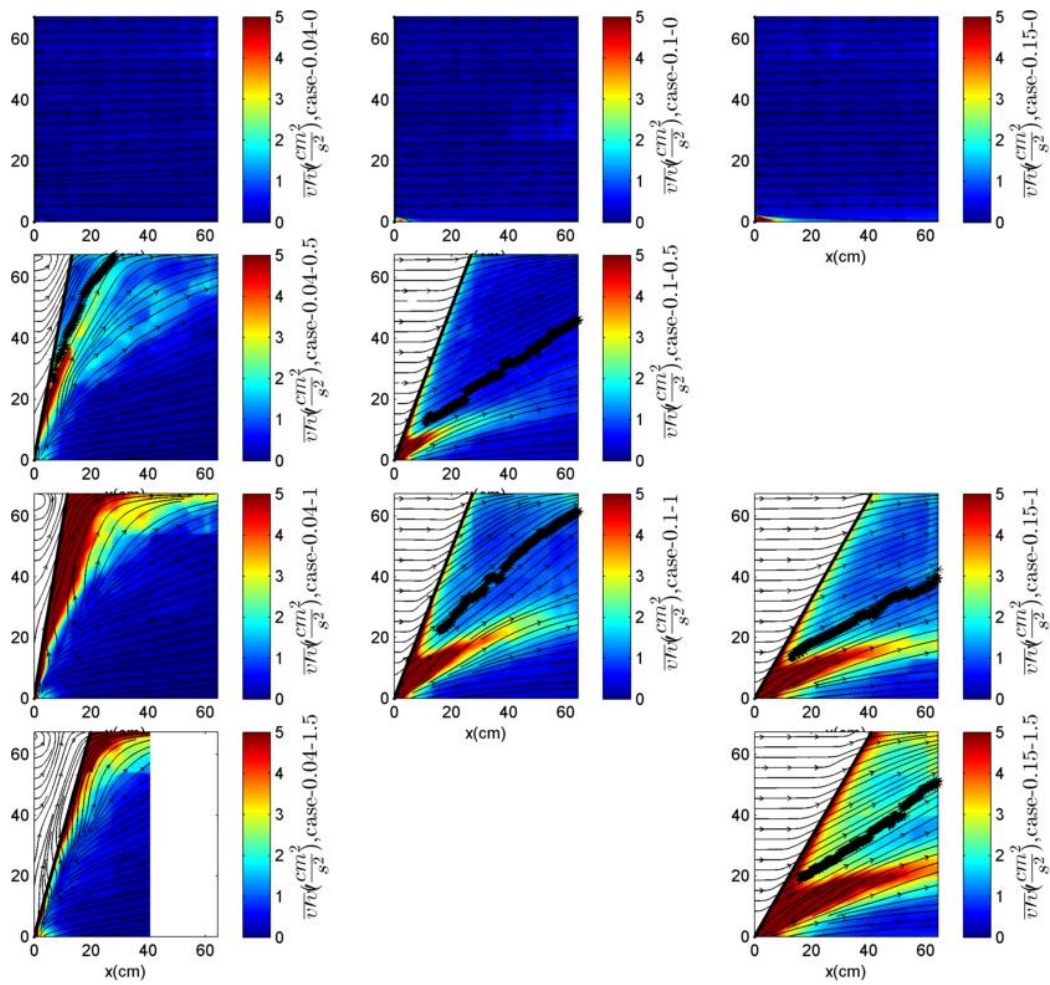
Figure 29. vv-Component of the kinematic Reynolds stresses together with the streamlines for the time average velocity field, and trajectory of the maximum time average velocity.
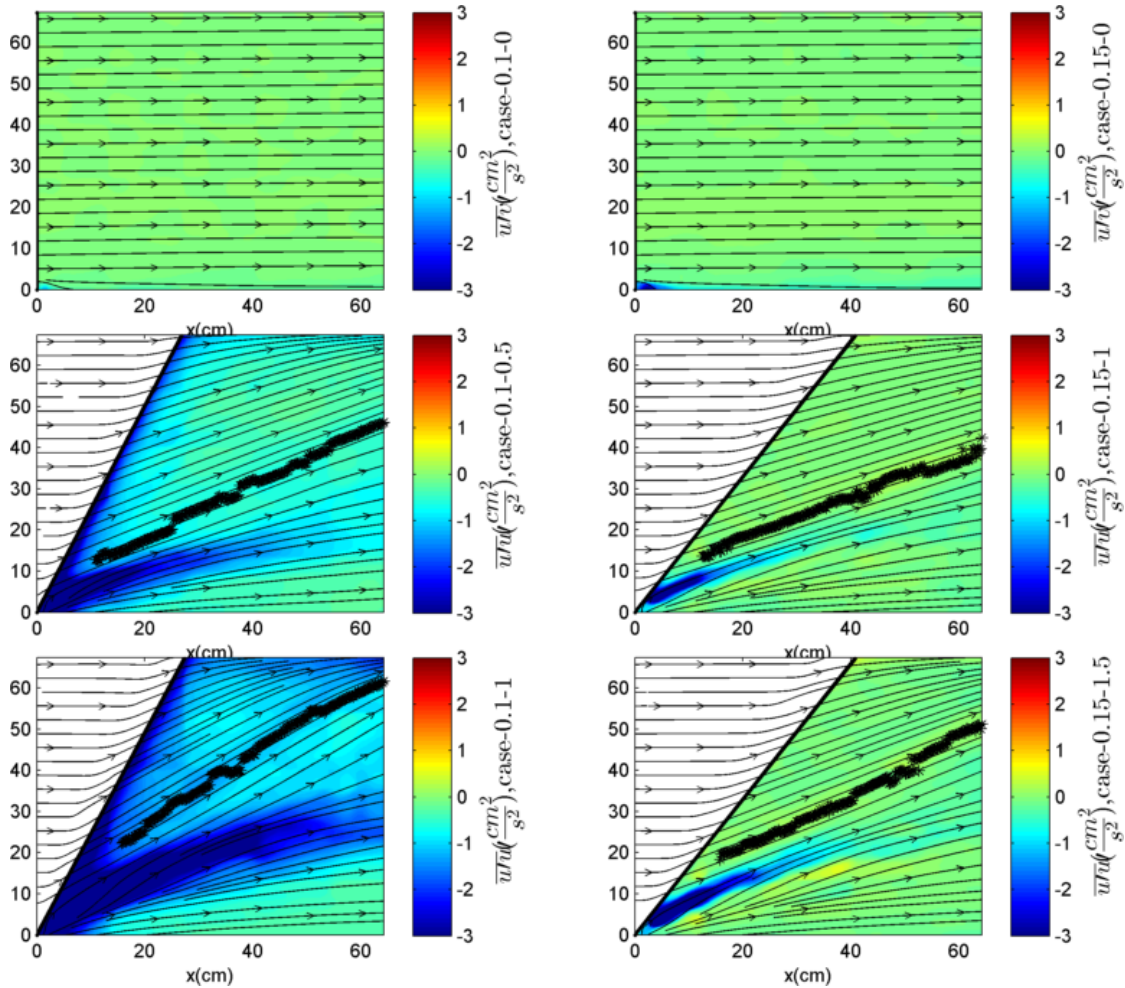
Figure 30. uv-Component of the kinematic Reynolds stresses together with the streamlines for the time average velocity field.

3.4.3 *Isotropy*

Figure 31 presents the difference between the vertical and horizontal as a metrics for isotropy in the wake region. As shown in the column of plots, the background flow is essentially isotropic with some anisotropy created due to the existence of the diffuser structure at the bottom left of the measurement domain, which becomes larger by increasing the crossflow. With bubble injection, different degrees of separation between the weak and strong crossflow cause different behavior in the wake region. Hot color

regions depict where vertical fluctuations are larger and cool color regions stand for regions with larger horizontal fluctuations.

For the cases with strong crossflow, yellow regions cover a larger area in the wake. This region is created due to the vertical momentum that is injected by the bubbles, and the crossflow transports it downstream; i.e., vertical velocity is added to the fluid going through the bubble column and streams into the wake. There is a distinct blue region in the middle of the separated plume, which shows that this region has higher horizontal fluctuations. Meanwhile, it should be noted that these components do not belong to the principal axis of the Reynolds stress tensor, and for the separated plume and for further interpretations, the coordinates on the centerline and principal axis for each point should be computed. Below the separated plume, there is a region with high vertical fluctuation which is showing the high entrainment region. That is where entrainment is coming in and water is being entrained from the below. Flow becomes smoothed out below this region.

It can be seen in the figure that the introduction of bubbles creates anisotropy in the wake region. Anisotropy is noted to increase with increasing gas flux and with increasing crossflow. Anisotropy introduced by bubbles has been observed in stagnant bubble plumes where Simiano et al., (2006) reported strong anisotropy in the plume area in his experiments. These plots further indicate that the separated plume is unique from the rest of the wake, with transport being different above and below the separation height.
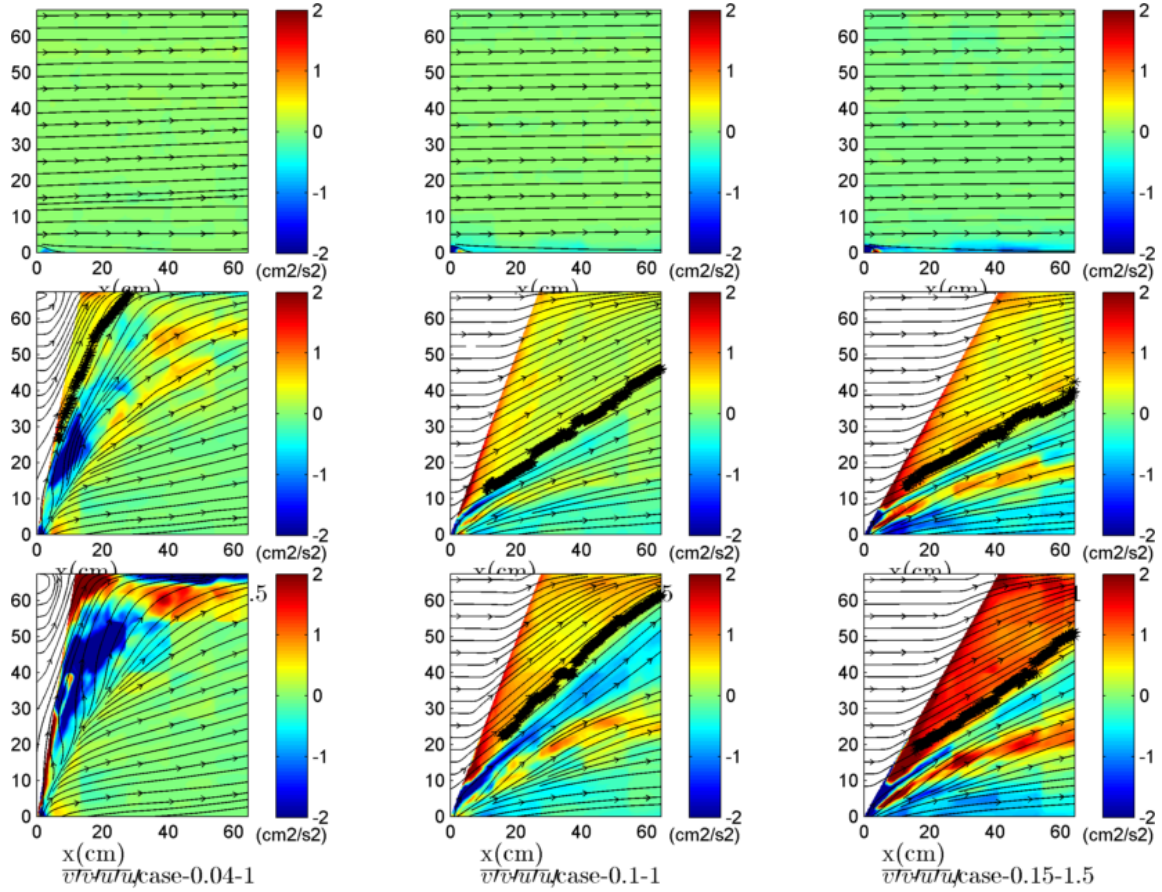
Figure 31. Plots of $\overline{v'v'} - \overline{u'u'}$ together with the streamlines to the time average velocity field, and trajectory of the maximum time average velocity.

3.4.4   *Mean flow kinetic energy*

In order to investigate the distribution of kinetic energy that is input from the bubbles in the wake region, we compute the kinetic energy of the mean velocity field defined by $K = \frac{1}{2}\left(\overline{U^2} + \overline{V^2}\right)$. Figure 32 shows the difference between the K field with the bubble column and that of the corresponding current field without bubbling; warm colored regions show the areas with elevated kinetic energy. Although overall, horizontal velocities are decreased in the wake, the increased values of kinetic energy stem from the increased vertical velocities linked to the effect of the bubbles. The

72

generated mean flow is in agreement with Lai and Socolofsky (2015), study who show that the potential energy lost by a bubble rising in a water column after reaching its terminal velocity is transferred to the water surrounding it. In a bubble plume, the potential energy loss in the bubbles results in generation of mean flow as well as turbulence. Some observations can be made here. First, kinetic energy is highest in the separated plume, where water has had the longest contact time with the bubbles. Second, the wake region above the separated plume is also significantly affected as water must flow through the bubble column to reach this region. As the bubble flow rate increases the amount of energy introduced in the wake increases.
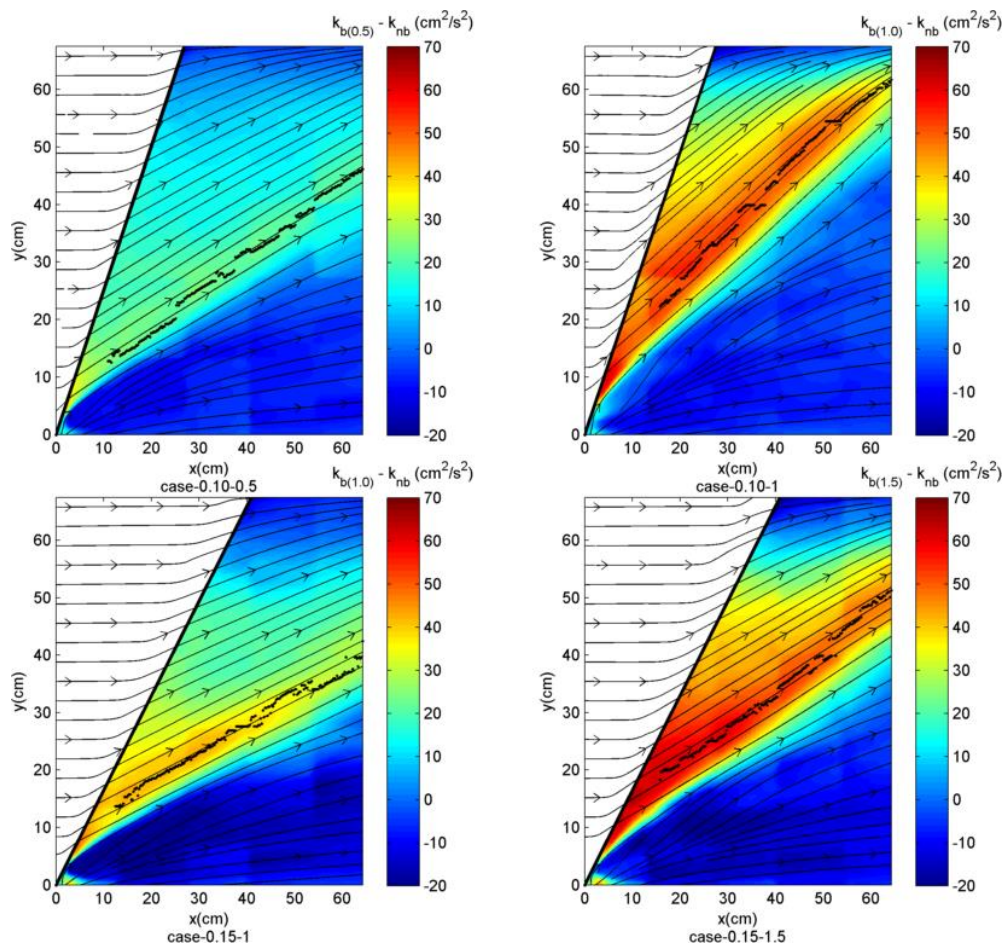
Figure 32. Difference in kinetic energy due to the introduction of bubble plumes together with the streamlines of the time average velocity and trajectory of the maximum time-averaged velocity, and trajectory of the maximum time average velocity.

3.4.5 *Identification of vortex pair structure from the Reynolds stresses*

As already shown in Figure 33, the measurements in these experiments have been carried out on a vertical plane through the centerline of the diffuser and resulting plane-wake structure. Previous numerical simulations and lab experiments in single phase flow (e.g., (Tian and Roberts, 2003)) predict and show the existence of the vortex pair in the section view of a jet in crossflow, which is delineated schematically in Figure *33*. A similar vortex structure is expected for the separated plume in the wake of a

74

bubble column. The signature of this vortex pair has been seen in the above results, where elevated turbulence intensity and Reynolds stresses are observed at the base of the separated plume. TO verify this interpretation, we present results from similar experiments with dye injection used to track the separated plume, visualized on the same plume centerline by Planar Induced Fluorescence (PLIF). Observations of the PLIF image sequences demonstrate this structure by the sudden appearance of dye patches which were transported by this vortex pair into the centerplane by weak side-t-side meandering of the plume. These bottom traces of dye can visualize the vertical extent of these vortices.
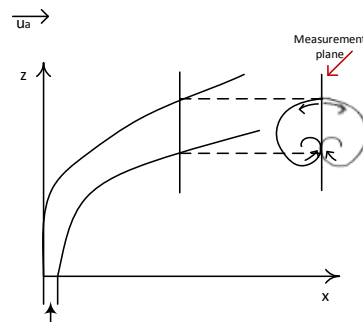
Figure 33. Schematic of a jet in crossflow showing the cross section vortex pair

Figure 34 shows representative instantaneous LIF images together with the location of the maximum vertical and horizontal turbulent Reynolds stresses. As delineated in the figure, the maximum Reynolds stresses correspond with the bottom, intermittent dye region. These dye patches are not visible in all PLIF images, and indeed, we are capturing some of the intermittency on the two lobes of the vortex pair created because of the side to side wondering of the plume which in turn is augmenting the

Reynolds stresses. This suggests that the maximum Reynolds stresses are associated

with the bottom of the vortex pair. Hence, the maximum Reynolds stresses appear to

show the convergence zone at the base of the vortex pair. Meanwhile, the trajectory of

the maximum averaged velocity magnitude is located at the top of this vortex pair

structure.
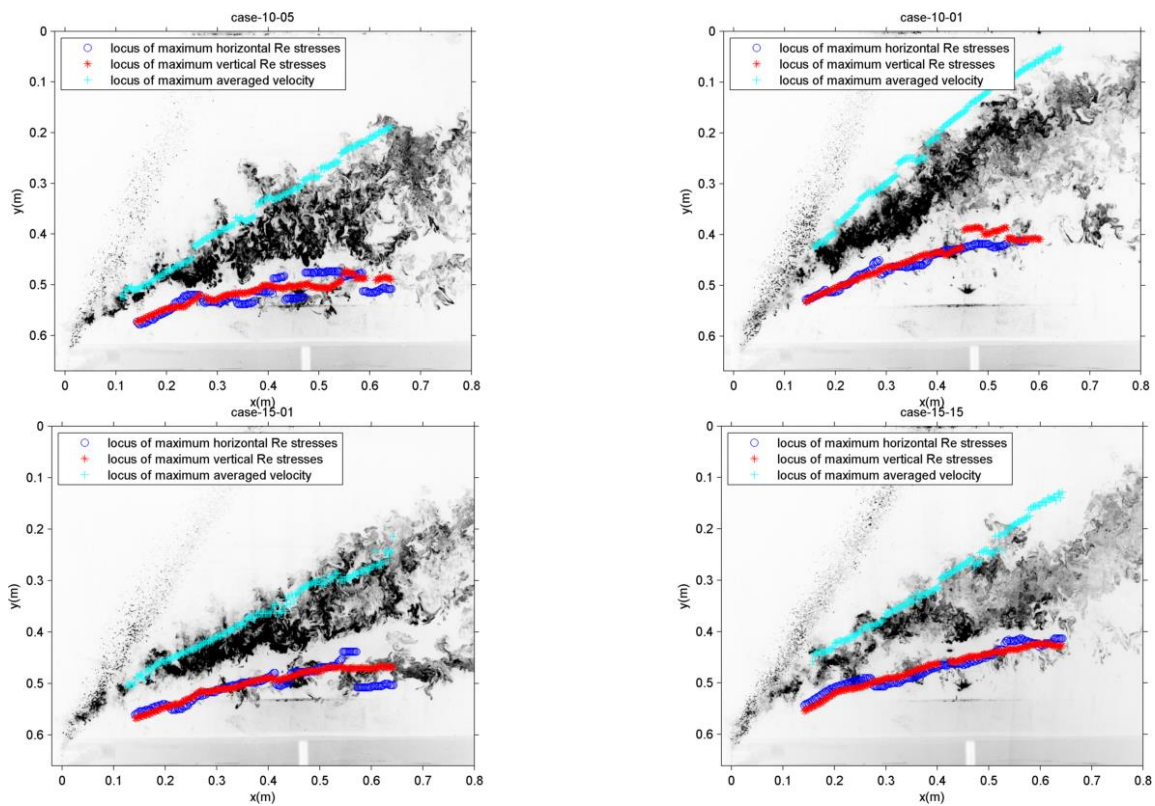
Figure 34. Locations of the maximum Reynolds stresses and averaged velocities together with the corresponding instantaneous PLIF images.

3. 5.   Summary and conclusion

This paper presented laboratory experiments of bubble plumes in uniform

crossflow. Instantaneous velocity information in the downstream wake of a round bubble

plume in presence of crossflows was obtained using PIV measurements. These data were

used for examining the properties of turbulence in the wake of the bubble plume. Turbulence intensities and Reynolds stress terms were obtained from the instantaneous velocity data. Results showed that bubbles can modify the liquid turbulence, and turbulence intensity increases with the increase in the introduction of bubbles and decreases with the increase in the crossflow. Profiles of turbulence intensities and Reynolds stresses showed that maximum values occur at the bottom interface of the separated plume and ambient fluid. The difference between the vertical and horizontal fluctuation was studied as an issue of isotropy. Observation showed that agitation covers a wider area in the vertical fluctuations, while the separated plume is shown as a distinct region with higher horizontal fluctuations. Furthermore, increasing the bubble flow rate and crossflow would increase the anisotropy of the wake turbulence, where the background flow is initially isotropic before introducing the bubbles. The distribution of the increase in the kinetic energy of the mean flow induced by the bubbles was also shown. The increase is not uniformly distributed, but is concentrated in the separated plume and the downstream region above the separation height. Moreover, observations show that the location of the maximum Reynolds stresses corresponds to the base of the vortex pair structure for the separated plume.

4. FIELD STUDY OF LAKE SEDIMENT OXYGEN UPTAKE IN TWO AERATED LAKES: ROLE OF CURRENTS AND TURBULENCE IN THE BOTTOM BOUNDARY LAYER

4. 1.   Overview

This paper presents the results of field measurements for two field campaigns conducted in two different lakes with different natural currents and bubble plume aeration installations. The gas flow rates of the diffusers in each lake were manually varied during each campaign to study the oxygen response if the lake to aeration. The effects of artificial and natural currents on the sediment oxygen uptake were also studied through *in situ* measurements of temperature, dissolved oxygen profiles, current velocities and wind data. Analysis of all the data showed that the bubble plume oxygenation influences the sediment oxygen uptake mainly by increasing the oxygen concentration of the hypolimnion, thereby increasing the concentration gradient and diffusive flux at the sediment-water interface. Also, changing the bubble flow rate can excite internal waves, which in turn generate unsteady currents. Finally, we validate a physics-based predictive model for the flux of oxygen across the sediment-water interface as a result of mixing induced by the natural and bubble plume induced artificial currents. A hydrodynamic model, based on the film-renewal model, was applied, which predicts the boundary layer thickness and oxygen uptake rate based on the ambient turbulence. An analytical model was needed for these weak turbulence environments to relate the measured turbulence dissipation rate to the eddy renewal time. Validation of

the model to the field measurements showed that the large eddy model best predicted the observed oxygen uptake.

4. 2.   Introduction

Low Dissolved Oxygen (DO) concentration in the hypolimnia of lakes and reservoirs is a significant global concern and is undesirable due to its negative impacts on water treatment, cold-water fisheries (Wu et al., 2003), and water quality downstream of hydropower dams (Little and McGinnis, 2001). Chemical, biological, and physical mechanisms all act to reduce DO in lakes and reservoirs. Excessive amounts of phosphorous increase the production of organic matter, which eventually dies and settles to the lake bottom, where oxygen depletion occurs during decomposition. At the same time, stable density stratification, particularly in the summer, limits the connectivity between the hypolimnion and atmosphere, thereby inhibiting DO replenishment by surface aeration, which likewise leads to low DO. In managed lakes, hypolimnetic oxygenation (HOx) systems are increasingly utilized to replenish DO while preserving the dimictic nature of the lakes (i.e. thermal stratification). Oxygen depletion, however, may be affected by the oxygenation since the sediment oxygen uptake is regulated by increased oxygen concentration and near-sediment hydrodynamics. Consequently, HOx systems have been historically undersized because of the underestimation of the oxygen uptake magnitude during aeration (Beutel, 2003). In the case of bubble plumes, which are commonly used for oxygenation (Wüest et al., 1992), two important questions are: to what extent do the currents generated by the operation of the bubble plume along with other natural phenomena affect the sediment-oxygen uptake, and how does the uptake

depend on the bottom turbulence and oxygen concentration profiles in the hypolimnion. Here, we address these questions by analyzing currents and turbulence properties measured in the boundary layers of two different aerated lakes during multiple, interdisciplinary field campaigns that varied the bubble plume operation. Successfully managing the water quality of lakes and reservoirs is crucial to the global water economy, and the importance of this work lies in understanding of the role of bubble plumes on altering the sediment oxygen uptake and developing predictive tools for numerical models of managed lakes.

Sediment-water fluxes occur within the Diffusive Boundary Layer (DBL) which is the millimeter-scale layer just above the sediment. The flux of oxygen at the sediment-water interface (SWI) J_{O2} can be predicted by Fick's law as

$$J_{O2} = -D \frac{\partial C}{\partial z} \tag{10}$$

where D is taken as the molecular diffusivity since turbulence vanishes in the viscous sublayer at the interface, C is the oxygen concentration, and z is the vertical coordinate. Substituting the analytical solution for the one-dimensional transport equation in quiescent conditions ($\frac{C(z,t)-C_{SWI}}{C_{bulk}-C_{SWI}}$ = 1- erf ($\frac{-z}{\sqrt{4Dt}}$)) for C in Equation (11), and taking the diffusive boundary layer thickness $\delta_{DBL} = \sqrt{2Dt}$, the flux can be expressed as

$$J_{O2} = -D \frac{(C_{bulk}-C_{SWI})}{\delta_{DBL}} \tag{11}$$

where C_{bulk} and C_{SWI} are the oxygen concentrations within the bulk fluid outside the DBL and at the Sediment-Water Interface (SWI), as depicted in Figure 35, and δ_{DBL} is the characteristic DBL thickness. The concentration at the sediment-water interface

remains close to zero due to the near instantaneous oxygen consumption by

biodegradation in the sediments, therefore, the sediment oxygen flux is controlled by: 1)

the concentration within the bulk fluid (C_{bulk}), which is controlled by the lake chemistry,

biology, and aeration by HO_x systems and 2) the theoretical thickness of the DBL, which

is affected by the hydrodynamics and turbulent mixing in the BBL (Lorke et al., 2003).
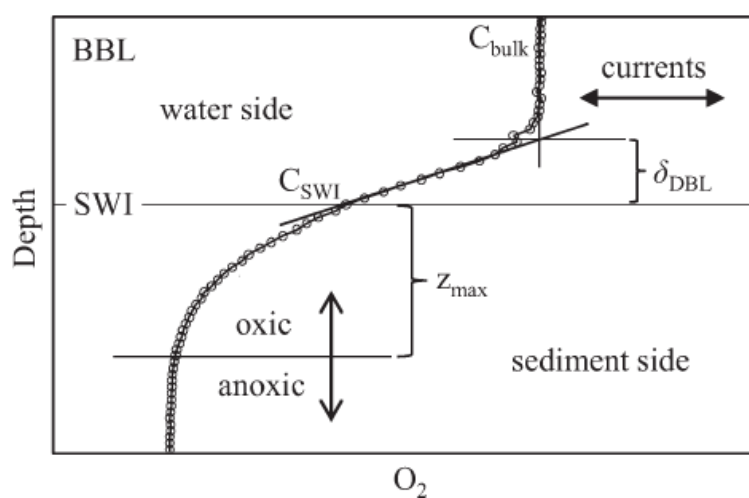
Figure 35. Key components of a DO profile across the SWI (reprinted from Bryant et al., (2010a). Z_{max} is the depth of the oxic zone in the sediment side. On the water side, BBL, DBL and oxygen concentrations at the SWI and bulk of water are demonstrated.

Previous studies showed the importance of hydrodynamics on the thickness and

structure of the DBL(Jørgensen and Revsbech, 1985, Roy et al. 2002). The increase in

the sediment oxygen uptake as a result of increased water velocity near the sediment

surface has been observed in laboratory experiments using sediment core incubations

(Beutel, 2003; Josiam and Stefan, 1999; Moore et al., 1996). In their field study, Lorke

et al. (2003) showed J_{O2} responds to changes in the near-sediment turbulence and

proposed that the turbulence characterized by the dissipation rate is the primary driver

for flux changes in less energetic and periodically forced systems such as lakes. Bryant et al. (2010) observed the same influence from turbulence in response to natural seiche activity; using oxygen microprofiles, they observed a significant response from J_{O2} to near-sediment turbulence on hourly time scales.

This study performs experiments in two morphologically different lakes, aerated with bubble plume diffusers. Bubble plumes solve the low DO problem in the hypolimnion by successfully adding oxygen. Even so, they may stimulate the uptake of oxygen by increasing oxygen concentrations and by adding energy through flow induced by the bubble plume buoyancy, which may generate near-field turbulence locally, close to the diffuser, and large-scale currents, especially in winter times when stratification may be destroyed by the diffuser, and these should be considered in the HOx design and operation. McGinnis et al. (2004) showed the enhanced mixing in the bubble plume near field induced by diffuser operation using field observation and computer simulations. Computer simulations by Singleton et al. (2010) showed the circulation of hypolimnetic water that could be stimulated by the bubble-plume oxygenation systems even at low gas flow rates. Gantzer et al., (2009) showed these HOx-induced increases in turbulent mixing, which they identified by higher warming rates, may cause excessive hypolimnetic oxygen uptake in small reservoirs which is similar to the effects of the seiche-induced turbulence, shown to cause significant variability in the sediment oxygen uptake (Bryant et al., 2010a). Later, Bryant et al. (2011) observed the effect of these large-scale currents in a small sheltered reservoir through the behavior of the SWI far field of the bubble plume diffuser upon turning the diffuser off. In their field study, J_{O2}

rapidly decreased upon turning off the diffuser, yet, it took nearly 8 days for the diffuser to replenish the water overlaying the sediment with oxygen after the diffuser was turned back on.

Despite the current broad application of bubble plumes in lakes, little is known about if /how turbulence changes caused by bubble plume operations affect J_{O2} in the field, where J_{o2} can be significantly affected by natural turbulence as well. Bryant et al. (2011) assessed *in situ* how HOx-induced variation in near sediment mixing and oxygen concentrations influence J_{O2} by correlating the J_{O2}, current velocity, and mixing calculated from the oxygen data; they observed high levels of correlations and they proposed HOx operation may have a strong influence on the mixing and sediment oxygen uptake. However, hydrodynamic data was restricted in their study due to the lack of near-sediment velocity measurements, and turbulent dissipation rates were calculated from J_{O2} and δ_{DBL} measurements, thus were not independent. They used a correlation between δ_{DBL} and the viscous boundary layer as is proposed in Wüest and Lorke (2003) and then estimated friction velocity from the correlation between the viscous boundary layer thickness and the friction velocity (Schlichting, 1979). Finally, they calculated dissipation rates from the friction velocities using the law-of-the-wall assumptions. Nonetheless, as shown by Lorke et al. (2002), this assumption may not be valid for the oscillatory unsteady BBL flow common in lakes. To overcome this weakness, in this paper we directly measure the dissipation rates from high resolution velocity data near the DBL.

Furthermore, it would be beneficial for the numerical models and for designing bubble plume diffusers to more accurately predict the induced sediment oxygen uptake. The current best practice is the use of an induced hypolimnetic oxygen uptake multiplier as a factor of safety (Beutel, 2003; Moore et al., 1996). Several models are proposed in the literature to predict the flux of gas across the interface (Lorke and Peeters, 2006; Socolofsky and Jirka, 2005;O'connor et al. 2009). Since models exist in the literature for boundary exchange that include the near-sediment velocity and turbulence, the purpose of this study is to assess the performance of these models using simultaneous *in situ* field measurements of J_{O2}, velocity, and turbulence to study the link between bubble plume operation and boundary exchange.

To address these gaps, we investigated the physical processes that control oxygen uptake in two distinct lakes exhibiting low bottom velocities and negligible inflows and outflows that are aerated by bubble plume diffusers. These lakes have different morphology and wind forcing so that they experience different coherent motions and internal waves near the sediments. Using high-resolution chemical and hydrodynamic data, we acquired direct measurements of J_{O2}, velocity, and turbulence and analyzed the results to test the hypothesis that bubble plume operation will stimulate oxygen uptake and that this partly results from currents induced by the bubble plume; oxygen uptake is also assumed to increase during oxygenation due to the elevated oxygen concentration in the hypolimnion, and this work attempts to quantify the contribution from these two mechanisms. To this end, we discuss the temporal variability of the oxygen uptake rate and investigate if and how the bubble flow rate provides a physical control for the

84

observed variability. In the end, we synthesis these data to produce a predictive model for J_{O2} that depends on the turbulence in the hypolimnion.

This paper is organized as follows. Section 4.3 presents the study sites, measurement methods, diffuser operation, and the campaign schedule. In section 4.4, we use concentration measurements at the SWI to compute J_{O2} and introduce the main predictive models we will consider. Section 4.5 presents the observations of the lake physics including fine-scale BBL turbulence, meteorological forcing, lake mixing state, and basin scale motions. This section also discusses the interplay of the dynamics across these many scales and the resulting behavior in the BBL. Section 4.6 synthesizes these measurements to validate a predictive model for J_{O2} and compare the J_{O2} dynamics to bubble plume diffuser operation. The final section, section 4.7, presents the summary and conclusions along with recommendations for future modeling studies in these lakes.

4. 3.   Materials and methods

4.3.1   *Two contrasting lake study sites*

We carried out field measurement campaigns in Carvin's Cove Reservoir, Virginia (CCR) in 2013 and in Lake Hallwil (LH), Switzerland in 2012. These are different lakes with different natural currents and aeration installations, which provide us with different flow regimes. Lake properties are summarized in Table 3. For each field campaign the diffuser operation was varied per the design goals given in section 4.3.5.

Table 3. Characteristic features and diffuser systems of the two lakes under study

Parameter	CCR Value	LH Value
Maximum depth (m)	21.3	46.5
Mean depth (m)	9.6	28.9
Surface area (m^2)	2.5×10^6	9.9×10^6
Total water volume (m^3)	24×10^6	285×10^6
Diffuser geometry	linear	circular
Number of diffusers	2 lines	6
Diffuser dimensions (m)	1250 m long (with average separation distance of 75 m)	6 round diffusers (6.5 m diameter) arranged with equal spacing around a 300 m diameter circle
Average diffuser depth (m)	21	46
Gas flow rate to all diffusers (Nm^3/h)	68	46-148 (O_2), 180 (air)
Elevation (m amsl)	357	449

CCR is located in southwestern Virginia and is the main drinking water supply for the county of Roanoke, Virginia, USA. CCR is eutrophic and relatively shallow, with a maximum depth of 23 m, a width of about 600 m, and a length of about 8000 m. CCR is mildly susceptible to wind-driven forcing, but is also protected by the surrounding hills and has weak inflows. The oxygenation diffuser in CCR reservoir consists of two, parallel line-source diffusers, located along the edge of the deepest region of the hypolimnion near the reservoir dam. The CCR HOx system injects pure oxygen over a wide range of flow rates which facilitates operational flexibility. Bubbling occurs in the summer months, when seasonal stratification leads to oxygen depletion, with the goal to minimize soluble Fe^{2+} and Mn^{2+} in the source water (Gantzer et al., 2009). Figure 36 shows the plan view and bathymetry of CCR.
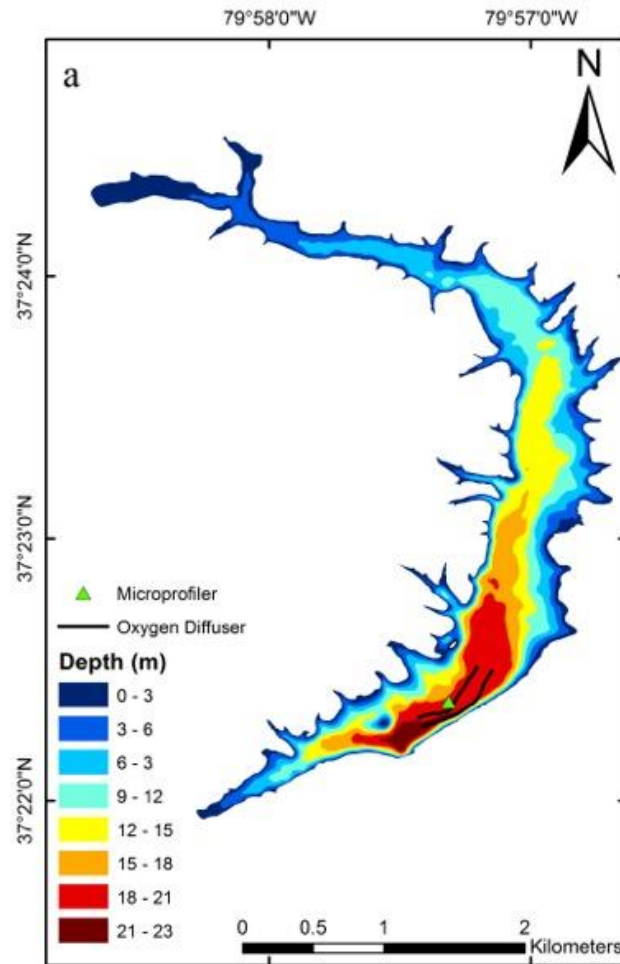
Figure 36. Map of Carvins Cove Reservoir (CCR)

Lake Hallwil (LH) is a deep, medium-sized natural lake located north of
Lucerne, Switzerland. LH is eutropic. It is 8.3 km long, 1.4 km wide, and has an average
depth of about 29 m with a maximum depth of about 47 m. Figure 37 shows the
bathymetry of this lake. River-induced currents are insignificant in this lake as the mean
inflow rate is 2.3 m^3/s. LH is surrounded by low mountains along its main axis on both
western and eastern sides and therefore, strong winds are predominantly along the lake's
main axis. LH undergoes thermal stratification in the summer and often experiences
strong, wind driven seiche cycles. During the stratified period, it becomes anoxic in the

hypolimnion as a result of high oxygen consumption. In order to aerate the hypolimnion,

diffusers are arranged in a circle of six pods at the deepest region of the hypolimnion,

near the center of the lake (see Figure 37 for details). The system delivers pure oxygen

gas in summer oxygenation mode and can pump air or oxygen in winter as needed.
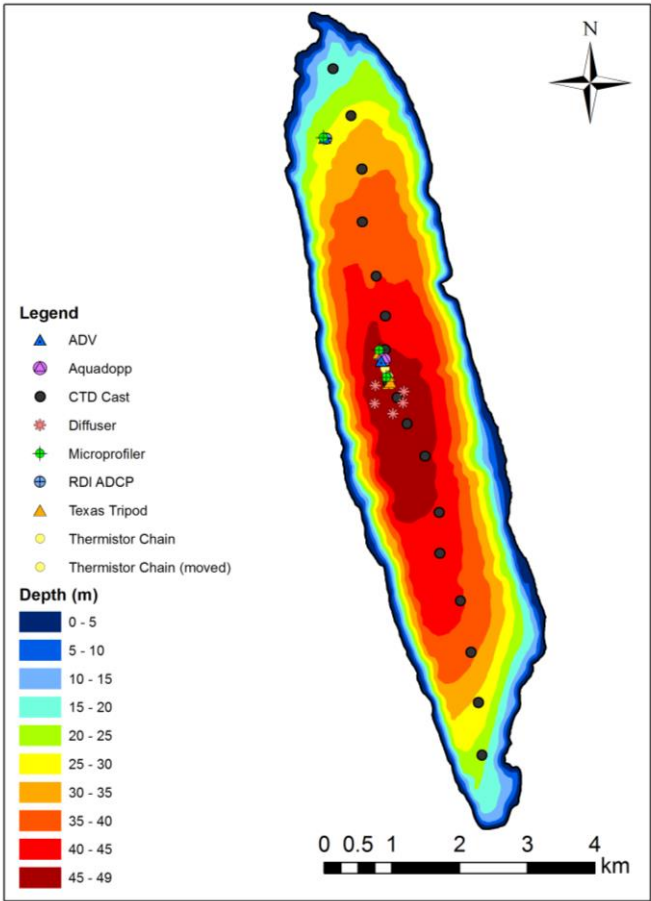
Figure 37. Bathymetry of Lake Hallwil. Diffusers are shown in the map

We used a combination of instruments moored at various locations in the

hypolimnia of these lakes to observe and assess the effects of oxygenation in each field

campaign. Figure 36 and Figure 37 show the locations of the mooring sites (marked as

the microprofiler). The remaining sections describe these instruments and the logistics of the field campaigns.

4.3.2   *Oxygen microstructure at the lake bottom*

A bottom lander equipped with a microprofiler measured fine-resolution profiles of oxygen and temperature above and through the SWI (Bryant et al., 2010b). The microprofiler (Unisense MP-4) was equipped with two microsensors (one Clark-type oxygen sensor and one thermocouple temperature sensor, Unisense A/S). The profiler acquired complete profiles every 50 minutes at steps of up to 0.1mm from 10 cm above to 0.5 cm below the SWI, deep enough to reach zero DO in the sediment. Resolution was set to be 10-mm from 10 cm to 1 cm above the SWI, 1-mm resolution from 1 cm to 0.5 cm above the SWI, and 0.1mm resolution from 0.5 cm above to 0.5 cm below the SWI. A detailed analysis of the oxygen measurements from these field campaigns can be found in Bierlein et al. (2015).

4.3.3   *Hydrodynamic measurements in the bottom boundary layer*

An Acoustic Doppler Velocimeter (ADV, Nortek Vector) was deployed on a separate frame close to the microprofiler to continuously measure the three-dimensional velocity in a small measurement volume. The ADV was mounted such that the measuring volume was about 15-20 cm above the SWI, varying among deployments; sample rate also varied by deployment, fixed at 16 or 8 Hz. The temporal resolution was adequate in each deployment to capture the structure of the turbulence statistics into the inertial subrange of the flow.

To capture the spatial structure of the bottom boundary layer, a high-resolution Acoustic Doppler Current Profiler (ADCP, Nortek Aquadopp with high resolution firmware) was moored above the sediment-water interface in a down-looking orientation on the same frame as the ADV. With the ADCP, we could measure the very low current velocities in the BBL of these lakes with rather high spatial and temporal resolution. We operated the ADCP in high resolution mode, which is designed to offer high accuracy at small cell sizes. The instrument measured vertical profiles of the three-dimensional current velocity from 1.4-1.6 m above the bottom to the sediment-water interface with a vertical resolution (bin depth) of 20-40 mm, depending on the deployment. The side-lobe interference region was identified from the amplitude measurements by locating the point that the amplitude starts to increase due to the simultaneous side-lobe and main-lobe returning energy (Owen, n.d.). This region is the bottom blanking distance, which extended up to nearly 10 cm from the bottom and was excluded from the data. The ADCP was operated in 30 minutes burst mode with 1024 samples per ensemble at the rate of 2-4 Hz. As part of the data quality assessment, we used the data from the ADCP to check its coherence with the data from the ADV. The result of this comparison showed a high rate of correspondence in the measured velocities.

Both the ADV and ADCP were mounted on a single tripod, which was designed and constructed following manufacturer recommendations for each instrument (e.g., material, placement, and mounting) and to minimize hydrodynamic disturbance from all supports. In order to acquire longer time series, we used extra battery canisters. A

schematic figure of the tripod used in the LH 2012 campaign is shown in Figure 38. A

similar tripod was constructed for the CCR experiment in 2013.
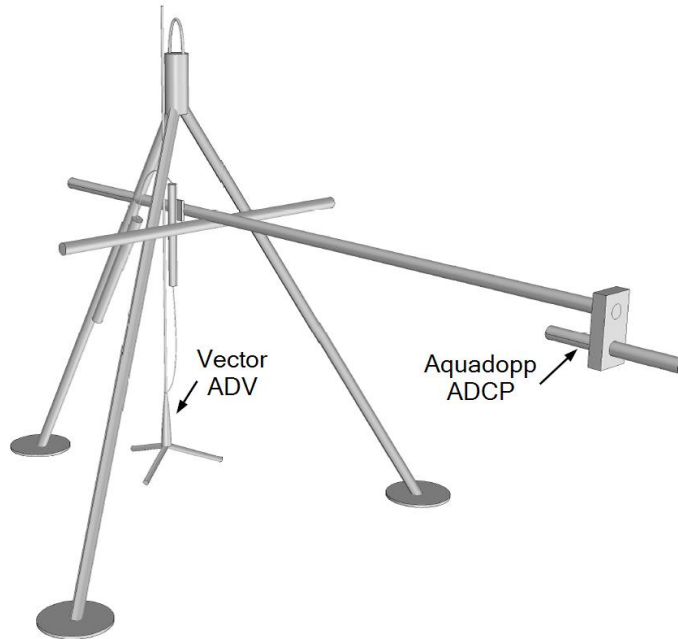
Figure 38. Tripod housing the Vector ADV and Aquadopp ADCP system used in LH in 2012.
Instruments were mounted downlooking.

4.3.4 Weather, lake temperature structure, and CTD measurements

Environmental conditions (i.e, ambient weather conditions and the lake thermal

structure) were also monitored during the campaigns. To monitor the meteorological

forcing, weather station was installed during each campaign to record wind speed and

direction, air temperature, and relative humidity.

To measure the temporal variability of the thermal structure of each lake,

thermistor chains were moored at fixed points near the bubble plumes during the

campaigns. Each chain consisted of different numbers of thermistors which were

attached to a weight at the bottom and float at the top. The types and resolutions of the

thermistors used were: TR1060 (logging temperature at 0.1 Hz) for LH in 2012 and RBRsolo (logging temperature at 1 Hz) for CCR in 2013. The vertical spacing between sensors was arranged according to the vertical temperature gradient in a way that more thermistors were placed in the thermocline region. The associated depths were 10, 16, 22, 28, 34, 40, and 46 m for LH and 2.5, 6.5, 7.5, 8.5, 9.5, and 17.5 m for CCR.

A Conductivity, Temperature, and Depth CTD (SeaBird SBE-19 Plus) probe, sampling at 4 Hz was also used to obtain higher spatial resolution of the temperature profile as well as profiles of DO and conductivity. Profiles were taken at pre-defined sampling stations following a regular schedule throughout the field campaign.

4.3.5 *Bubble plume operation and deployment of instruments*

During each measurement campaign, we varied the diffuser flow rate to study the effects of the bubble plume operation and the lake response to different modes of oxygenation. Table 4 lists the diffuser operations during the field campaigns. This scheme provided us with oxygen fluxes over a wide range of ambient conditions.

The locations of each of the moored instruments varied for each lake and for each measurement campaign. Locations of moored instruments have been pinned on Figure 36 and Figure 37, relevant information and schedule of the respective deployments are summarized in Table 4.

Table 4. Schedule of the campaigns

Hallwil 2012	15-May	18-May	20-May	21-May	22-May	23-May	24-May	26-May	28-May	30-May	1-Jun
Microprofiler							Moved to 300m site @1400 (WPT 619)	Moved to 25m Depth site @1200 (WPT 623)	Moved to 30m site @1445 (WPT 626)		Removed @1500
Velocity mooring	Removed @1040 to replace feet. Redeploy at 1140 (WPT 596)		Removed @1030		Deployed near Microprofiler (WPT 614)		Moved to 300m site @1400 (WPT618)	Removed @1000	Deployed at 30m site @1055 (WPT625)		Removed @1215
Thermistors							Adjusted 30m chain (WPT 620)				Removed @1230
Diffusor		OFF @1200		ON @1700						OFF @1330	
Met Station					Continous recording						

CCR2013	25-May	26-May	27-May	28-May	29-May	30-May	31-May	1-Jun	2-Jun
Microprofiler		Deployed @ 1010							Retrieved @ 1145
Velocity Mooring		Recording @ 1500							Retrieved @ 1055
Thermistors	Deployed @ 1400								Retrieved @ 1005
Diffuser	18 SCFM		Adjusted to 40 SCFM @ 1120	Adjusted to 30 SCFM @ 1030	Adjusted to 20 SCFM @ 1115	Adjusted to 10 SCFM @ 1035	Off @ 1035	On @ 1040, adjusted to 13.5 SCFM	
Met Station	Deployed 24 May								Retrieved 6 June

4. 4. Direct measurements of oxygen uptake

4.4.1 Direct calculation of oxygen flux from profiler data

Oxygen fluxes were calculated from the *in situ* oxygen microprofiles. Oxygen microprofiles were obtained approximately every 50 minutes based on the profiling scheme mentioned in (4.3.2). For each profile, J_{O2} was calculated using two approaches. Firstly, from the water-side portion using the direct method (Bryant et al., 2010b):

$$J_{O_2,water} = -D_w \left. \frac{\partial C}{\partial z} \right|_w = -D_w \frac{(C_\infty - C_0)}{\delta_{DBL}}$$

(12)

where D_w is the molecular diffusion coefficient of O_2 in water (m^2 d^{-1}), $\left. \frac{\partial C}{\partial z} \right|_w$ is the

oxygen gradient in the DBL immediately above the SWI (mmol m^{-4}), C_∞ is the DO

concentration in the bulk water in the BBL, immediately above the DBL (mmol m^{-3}), C_0

is the DO concentration at the SWI (mmol m^{-3}), and δ_{DBL} is the thickness of the DBL

(m).Figure 39 shows how δ_{DBL} and the other parameters were defined for a

representative micro profile of oxygen. Second, J_{O2} was estimated using the sediment-

side of the DO microprofile through an analogous equation:

$$J_{O_2,sediment} = -\varnothing D_s \left. \frac{\partial C}{\partial z} \right|_s$$

(13)

where ϕ is the sediment porosity (m^3 voids m^{-3} volume), D_s is the molecular diffusion

coefficient of O_2 in the sediment pore-water (m^2 d^{-1}; estimated as $D_s = \phi D_w$) and $\left. \frac{\partial C}{\partial z} \right|_s$

is the oxygen gradient immediately below the SWI (mmol m^{-4}). Measurements of ϕ

(0.96 for CCR; 0.94 for LH) were made from sediment cores collected from both lakes

during field sampling campaigns conducted prior to those described in this study.

The location of the SWI was determined by visually examining each profile to

identify the linear region in the DBL and the change in slope associated with the

difference in porosity between the water column and the sediment. Standard deviations

of the measurements at each point in the microprofiles were also used to aid and verify

the correct positioning of the SWI, since the standard deviation in the measurements should decrease as the microsensors approach the SWI.

Because the exact location of the boundary layer thickness can be somewhat ambiguous to discern in the oxygen microprofiles, we used the effective DBL approach proposed by Jørgensen and Revsbech, (1985). This method extrapolates the oxygen gradient at the SWI until the DO concentration is equal to C_∞, using this distance as δ_{DBL} (see Figure 35). More details of the oxygen flux calculations can be found in Bierlein et al. (2015), and a sample of the measured fluxes is shown in Figure 39.
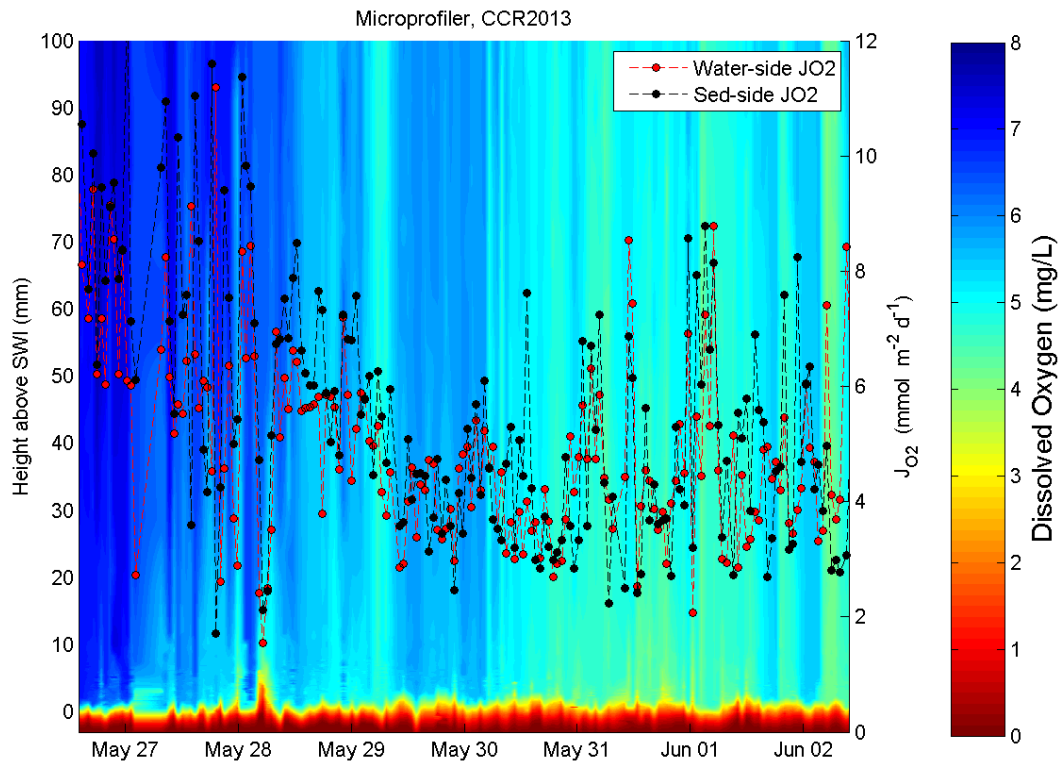
Figure 39. Time series of J_{O2} overlaid on DO for CCR2013

4.4.2   Correlation of J_{O2} estimates with turbulence models

Models to predict J_{O2} seek to correlate D and δ_{DBL} with properties of the flow in the DBL or bulk properties of the hypolimnion. The standard boundary transfer equation is $J_{o_2} = -k_l \left(C_\infty - C_0 \right)$ where k_l is the transfer velocity, effectively given by D/δ_{DBL}. Hence, k_l depends on both the thermodynamics (D) and flow conditions in the BBL (δ_{DBL}). Several models are available in the literature to predict k_l from the molecular diffusivity and various flow properties of the overlaying water column. Here, we consider two models, each based on different assumptions about the physical behavior of the DBL. In the first type of model, film theory (Lewis and Whitman, 1924), it is assumed that ambient currents and turbulence work to limit the diffusive growth of δ_{DBL}, so that δ_{DBL} is a constant over time scales comparable to the longest time scales of the turbulence. The direct measurement presented in Section 4.4.1 is an example of this model, where δ_{DBL} is measured for each lander profile. Predictive models relate the thickness of δ_{DBL} to the boundary layer characteristics near the interface. Lorke and Peeters, (2006) present a synthesis of these types of models and show that the Batchelor length scale L_b is an appropriate scale for δ_{DBL}, yielding

$$\delta_{DBL} \propto L_B = 2\pi \left(\frac{\nu D^2}{\varepsilon} \right)^{1/4}$$

(14)

where ν is the viscosity of water and ε is the eddy dissipation rate of the local turbulence. This leads to

$$k_l = \frac{1}{2\pi} \left(\frac{D^2 \varepsilon}{\upsilon} \right)^{1/4}$$

(15)

The challenge for this method is in measuring or estimating ε near the DBL.

For flows where the law-of-the-wall is valid, ε can be replaced by the shear velocity u_*, and hence, related to the shear stress at the interface. For unsteady flows the correlation with ε itself can be used, where epsilon should be evaluated at the top of the viscous sub layer, at a height equal to the local Kolmogorov length scale of the overlying turbulence (Lorke and Peeters, 2006). The advantage of this latter approach is that it does not rely on the law-of-the-wall, which requires a fully developed, steady turbulent boundary layer.

The second type of model assumes that the DBL thickness is continually growing and shrinking under the unsteady action of the turbulence in the boundary layer. An example of this model is the film renewal model (Higbie, 1935), where δ_{DBL} grows following molecular diffusion into a quiescent ambient until a turbulent eddy penetrates the DBL and removes all the fluid, replacing it with fluid with concentration equal to C_∞, after which molecular diffusion resumes into the refreshed water. The effective boundary layer thickness is found from the time average flux over each refreshment cycle, and k_l is given by

$$k_l = \sqrt{\frac{4D}{\pi t_r}}$$

(16)

where t_r is the time scale of a refreshment cycle. The challenge in this model is in estimating t_r.

Theoretical models for t_r relate the refreshment rate to different time scales of the local, overlying turbulence. In the small eddy model, it is assumed that eddies at the Kolmogorov scale (with $t_k = (v/\varepsilon)^{0.5}$) are responsible for refreshing the DBL, leading to

$$k_l \propto \sqrt{\frac{4}{\pi}}\left(\frac{D^2\varepsilon}{\upsilon}\right)^{\frac{1}{4}}$$

(17)

This model has the same power-law dependence in D, ε, υ as the Lorke and Peeters (2006) model; hence, they assume the same underlying physical processes. In the large eddy model, it is assumed that eddies with the large eddy turn-over time scale are responsible for refreshing the interface. One estimate of the large eddy turn-over time scale, $t_I = \dfrac{l_0}{u_0}$, is based on the local turbulent kinetic energy, $k_{TKE} = \dfrac{1}{2}(\overline{u'^2} + \overline{v'^2} + \overline{w'^2})$ and the turbulent dissipation, yielding $t_I = k_{TKE}/\varepsilon$; u', v', and w' are the turbulent velocity fluctuations in the x, y, and z coordinate directions and the over-bar represents a time average. This scale results in

$$k_l \propto \left(\frac{4D\varepsilon}{\pi k_{TKE}}\right)^{\frac{1}{2}}$$

(18)

This result has a different power-law dependence and D and ε and does not include υ; hence, it hypothesizes a fundamentally different physical process than the Lorke and Peeters (2006) and small eddy model. The turbulent kinetic energy k_{TKE} relates to the energy input from the overall large-scale flow, and should be measured or estimated from numerical simulations. Both the Lorke and Peeters (2006) and the small eddy model propose the same functional relationship, but with a different leading coefficient.

Hence, these methods are identical. Lorke and Peeters (2006) compare their model to a wide range of data that suggest the model fit coefficient is of order 1. Thus

$k_l = \frac{1}{2\pi}(\frac{D^2\varepsilon}{\upsilon})^{1/4}$ fits the data. We will use this version of this model along with the large

eddy model to compare with our measured results.

Using the daily averaged fluxes measured by the lander as described in 4.4.1, we can calculate the corresponding film renewal frequency (time scales of the renewal) using equation 16. These are presented in Table 5.

Table 5. Daily averages for hypolimnetic oxygenation system (HOx) flow rate, sediment oxygen uptake rate (J_{O_2}), dissolved oxygen difference, transfer velocity, and estimated renewal time from film-renewal theory for a) CCR2013, b) LH 2012

A					
Date	Flow (m^3 h^{-1})	-J_{O2} (mmol m^{-2} d^{-1})	(C_{bulk}-C_{SWI}) (umol L^{-1})	K_l (m/s)	t_r (s)
5/26/2013	30.59	7.579	88.75	9.88*10^{-7}	1759.4
5/27/2013	67.96	6.025	90.50	7.71*10^-7	2894.8
5/28/2013	50.97	5.263	90.83	6.71*10^-7	3821.7
5/29/2013	33.98	4.199	104.15	4.67*10^-7	7893.6
5/30/2013	16.99	4.296	84.07	5.91*10^-7	4912.5
5/31/2013	0	4.755	77.58	7.09*10^-7	3415.9

B					
Date	Flow (m^3 h^{-1})	-J_{O2} (mmol m^{-2} d^{-1})	(C_{bulk}-C_{SWI}) (umol L^{-1})	K_l (m/s)	t_r (s)
5/16/2012	220.87	3.984	141.19	3.27*10^-7	15396.5
5/17/2012	220.87	2.919	53.59	6.30*10^-7	4133
5/18/2012	0	3.480	20.29	19.85*10^-7	416.77
5/24/2012	220.87	18.689	108.67	19.90*10^-7	414.56
5/25/2012	220.87	11.607	50.15	26.79*10^-7	228.9
5/26/2012	220.87	16.823	50.46	38.58*10^-7	112
5/27/2012	220.87	13.929	100.22	16.08*10^-7	644.63
5/29/2012	220.87	11.679	54.00	25.03*10^-7	262.14
5/30/2012	0	8.589	65.33	15.22*10^-7	709.36
5/31/2012	0	5.869	39.47	17.21*10^-7	554.5
6/01/2012	0	7.253	41.97	19.99*10^-7	410.84

The renewal times in Table 5 range from 112 seconds to 4.27 hours. These times are quite long, and are consistent with fact that lake bottoms are generally low-energy, affected by a wide range of scales of motion. In the following section, we present measurements of the different time scales that existed in these lakes during the measurement campaigns using the hydrodynamic measurements to understand whether the renewal time scales can be predicted from specific events in the hydrodynamic data.

Specifically, we present results for the turbulence characteristics of the BBL currents, internal motions, and the time-average boundary layer velocity profiles.

4. 5. Physics observations in the lake hypolimnion

4.5.1 Turbulence characteristics

Figure 40 shows the raw time series measurement of three current components measured by the ADV at 15 to 20 cm above the SWI in CCR and LH.
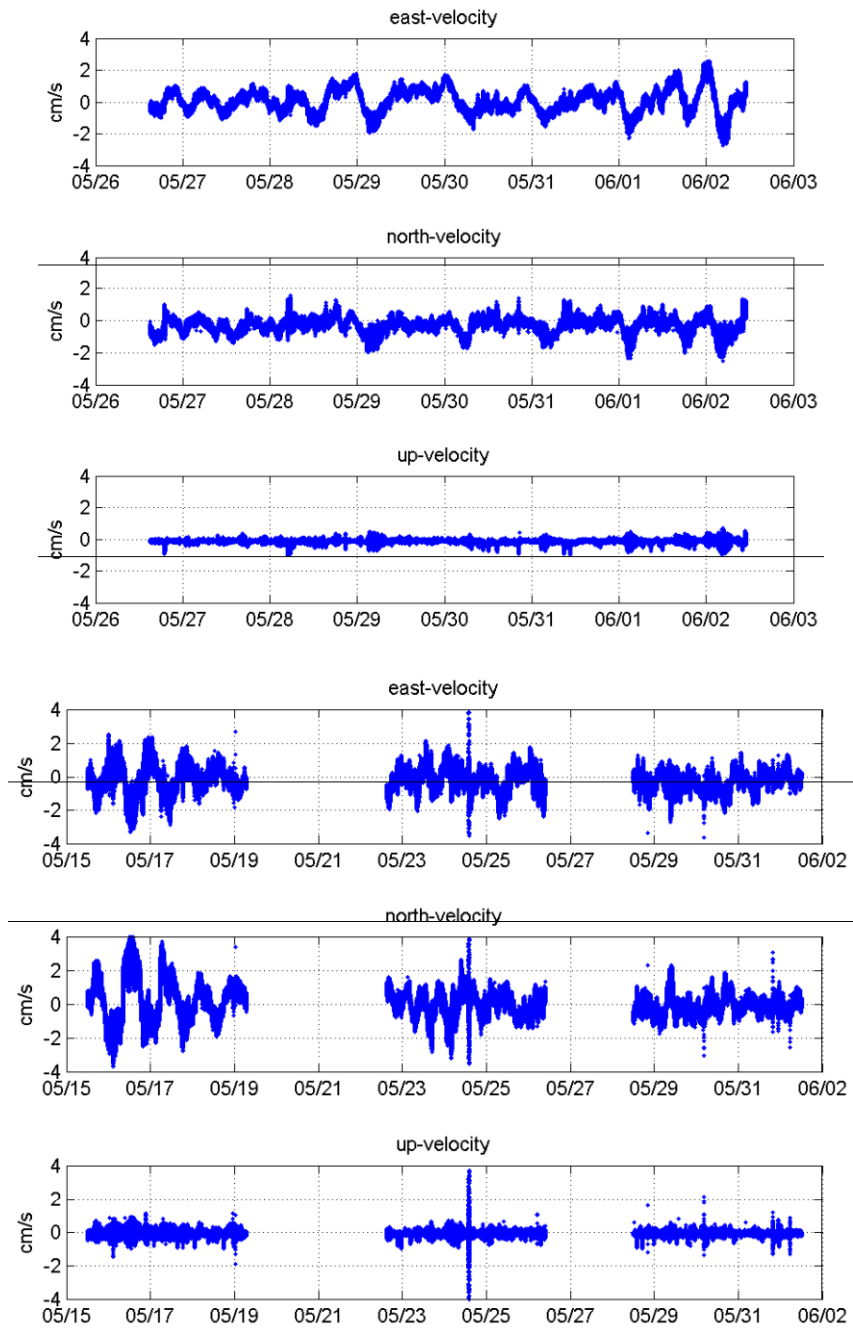
Figure 40. Components of current velocities a) at 20 cm above SWI for CCR2013 and b) at 15 cm above SWI for LH2012

An important parameter for the boundary exchange models in Section 4.4.2 is the dissipation rate of turbulent kinetic energy ε. We estimated ε from the ADV velocity

102

measurements using the inertial dissipation method (IDM). This technique is widely accepted and applied in oceanographic and atmospheric research (Grant, 1962; Lorke and Wüest, 2005; Bryant et al., 2010a). We estimated the dissipation from the inertial subrange of the velocity spectra, where, assuming eddies to be isotropic, the power spectra depends only on the wave number k (rad/m) and the rate of dissipation of turbulent kinetic energy k by:

$$E(k) = \alpha\, \varepsilon^{2/3} k^{-5/3}\ [m^3 s^{-2}] \tag{19}$$

where α = 1.56 (Sreenivasan, 1995) is the three dimensional Kolmogorov constant. Since the Vector (ADV) measures three dimensional current fluctuations at a fixed Eulerian point, we can calculate three one-dimensional spectra: E_{11} (spectra of the longitudinal current), E_{22} (spectra of the horizontal transverse current), E_{33} (spectra of the vertical current), each given by:

$$E_{11}(k1) = \alpha_1\, \varepsilon^{2/3} k^{-5/3}\ [m^3 s^{-2}] \tag{20}$$

$$E_{22}(k1) = E_{33}(k1) = \alpha_2\, \varepsilon^{2/3} k^{-5/3}\ [m^3 s^{-2}] \tag{21}$$

where $\alpha_1 = (18/55)\,\alpha$, $\alpha_2 = (4/3)\,\alpha_1$. Per (Pope, 2000).

To determine the longitudinal direction of the currents, we calculated the average velocity over an averaging period of 50 min, which corresponds to the measurement period of each oxygen profile. We accomplished this by rotating the velocities from the original frame of reference (i.e. east, north and up) into a new reference where the average of the transversal velocity component is zero over the averaging period.

Frequency domain spectra were calculated from the rotated velocity time series and then transformed to the wave number domain by invoking Taylor's frozen

turbulence assumption to convert statistically stationary measurements from frequency f

to wavenumber space (e.g., $U \frac{\partial}{\partial x} = \frac{\partial}{\partial t}$ and, k = 2πf/U, where U is the mean longitudinal

advection velocity over each 50 minute period). Taylor's hypothesis is considered valid

when eddies have negligible change as they move past a sensor. In other words, Taylor's

hypothesis could be acceptable when the turbulence intensity is small relative to the

mean current speed. Willis and Deardorff, (1976) suggest criteria for the validity of

Taylor's hypothesis such that σ_u <0.5 U, where σ_u is the standard deviation of the

fluctuation current speed u'. We evaluated this criterion for each measurement period as

is shown in Figure 41.
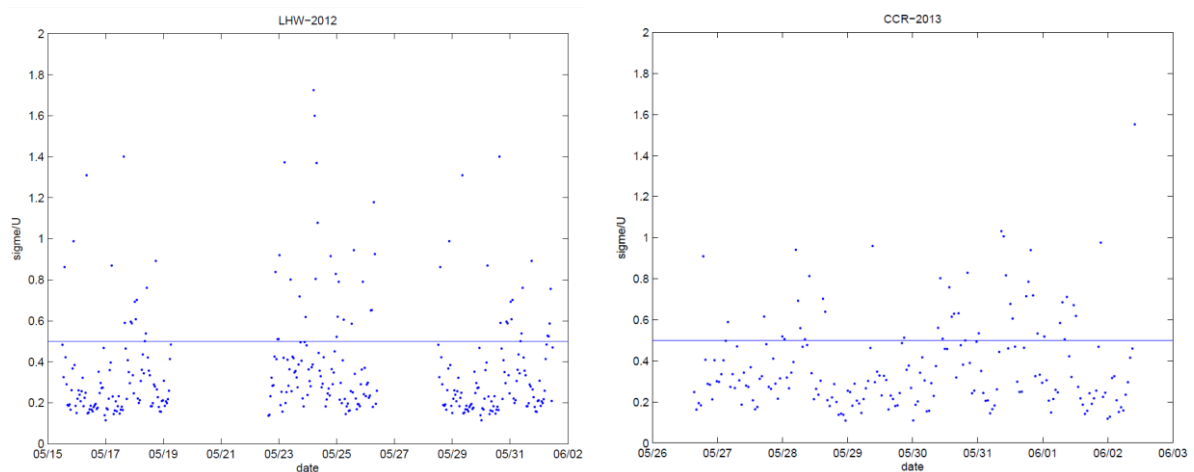
Figure 41. Ratio of turbulence intensity to the mean current speed to evaluate the validity of Taylor's hypothesis

According to this criterion, Taylor's hypothesis is valid more than 80% of the

measurement time. The fraction of violations for CCR 2013 was 21%. For Lake Hallwil

2012, the violation happened 13% in the first period of measurements, 24% for the

second period of measurements and 16 % for the third campaign. The occurrence of

violations seems to be isolated and randomly distributed; hence, we assume these have a negligible influence on the estimation of time series of ε.

As is shown in Figure 42, most of the time during the campaigns velocities are quite low, changing from 0 to 2 cm/s in each component. To evaluate whether the flow is turbulent during the measurements, we investigate the Taylor-scale Reynolds R_λ number, which is a parameter that has been widely used to classify turbulent boundary layer flows. R_λ can be used to ensure that the turbulence levels are high enough to develop an inertial subrange in the velocity spectra (Bluteau et al., 2011). R_λ is given by $R_\lambda = \frac{u'_1\lambda}{v}$ where λ is Taylor's microscale, which for isotropic turbulence is defined as: $\lambda = u'_1\sqrt{\frac{15v}{\varepsilon}}$. Saddoughi and Veeravalli, (1994) obtained a well-defined inertial subrange for $R_\lambda \geq 600$. Figure 42 shows the value of R_λ throughout our measurement campaigns. These data show that for CCR2013 14% of the times R_λ was smaller than 600 and that the occurrence was more in LH, with 45, 47, and 16 % of the times for each measurement period. Low values of R_λ occur in LH during the slack velocities generated by the basin-scale seiche. Turbulence is otherwise high and unsteady flows are known to be unstable; hence, we conclude that these lakes exhibit dominantly well-developed turbulent boundary layers.
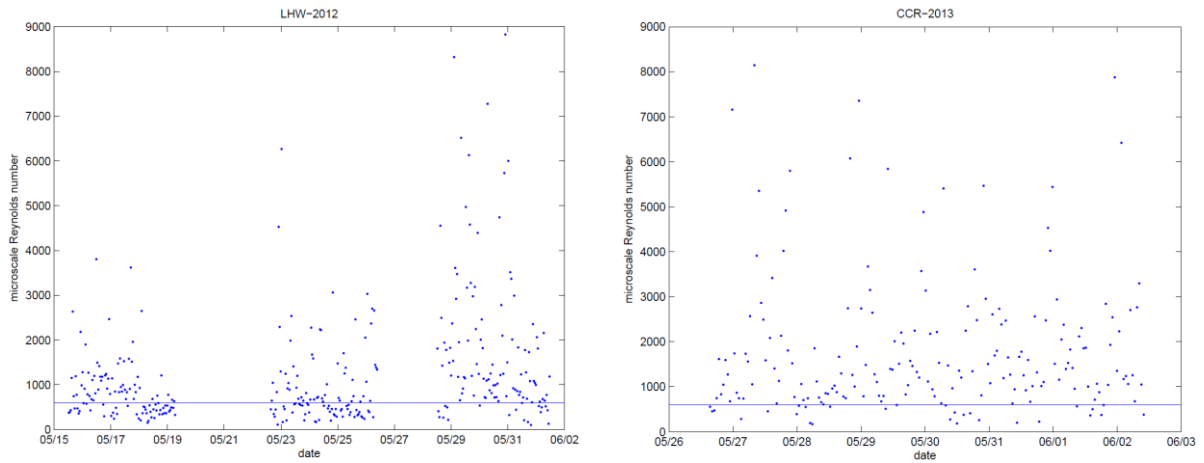
Figure 42. Taylor scale Reynolds number

The average power spectrum E_{11} for CCR2013 is shown in Figure 43. This averaged spectrum is calculated from 50 minute segments and then averaged over the full measurement period. The plot demonstrates the inertial sub-range span is almost a decade in frequency space, indicating the sampling period of the ADV is adequate to resolve ε .
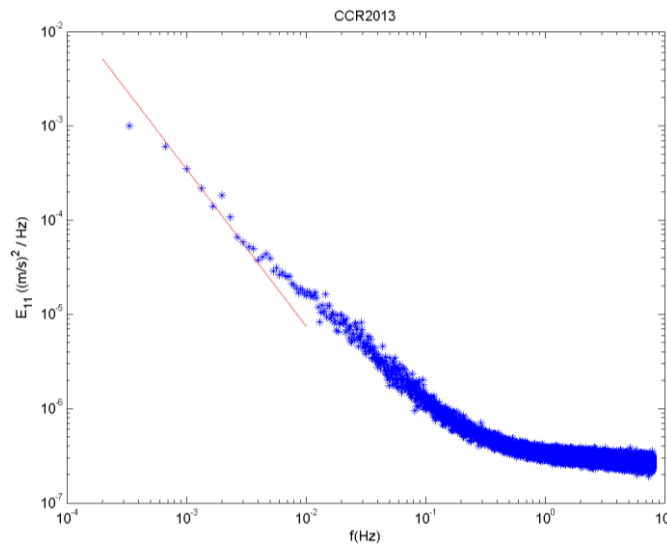
Figure 43. Averaged velocity spectra with the 5/3 slope based on 50 minutes segments (CCR2013)

106

For the IDM method, the power spectrum is multiplied by k $^{(5/3)}$ so that the resulting data are only dependent on ε in the inertial subrange (Bryant et al., 2010a). We then evaluate the dissipation rate as the average of the $E_{11}k^{5/3}$ in the inertial subrange since, as shown by Bluteau et al., (2011), the longitudinal velocity component is least affected by anisotropy of turbulence in density-stratified environments, such as lakes. The resulting longitudinal dissipation rates are shown in Figure 44 for the two lakes. Dissipation rates range between 10^{-11} and 10^{-8} W/kg, which is a typical value for a freshwater lake (Lorke et al., 2003; Wüest and Lorke, 2003).
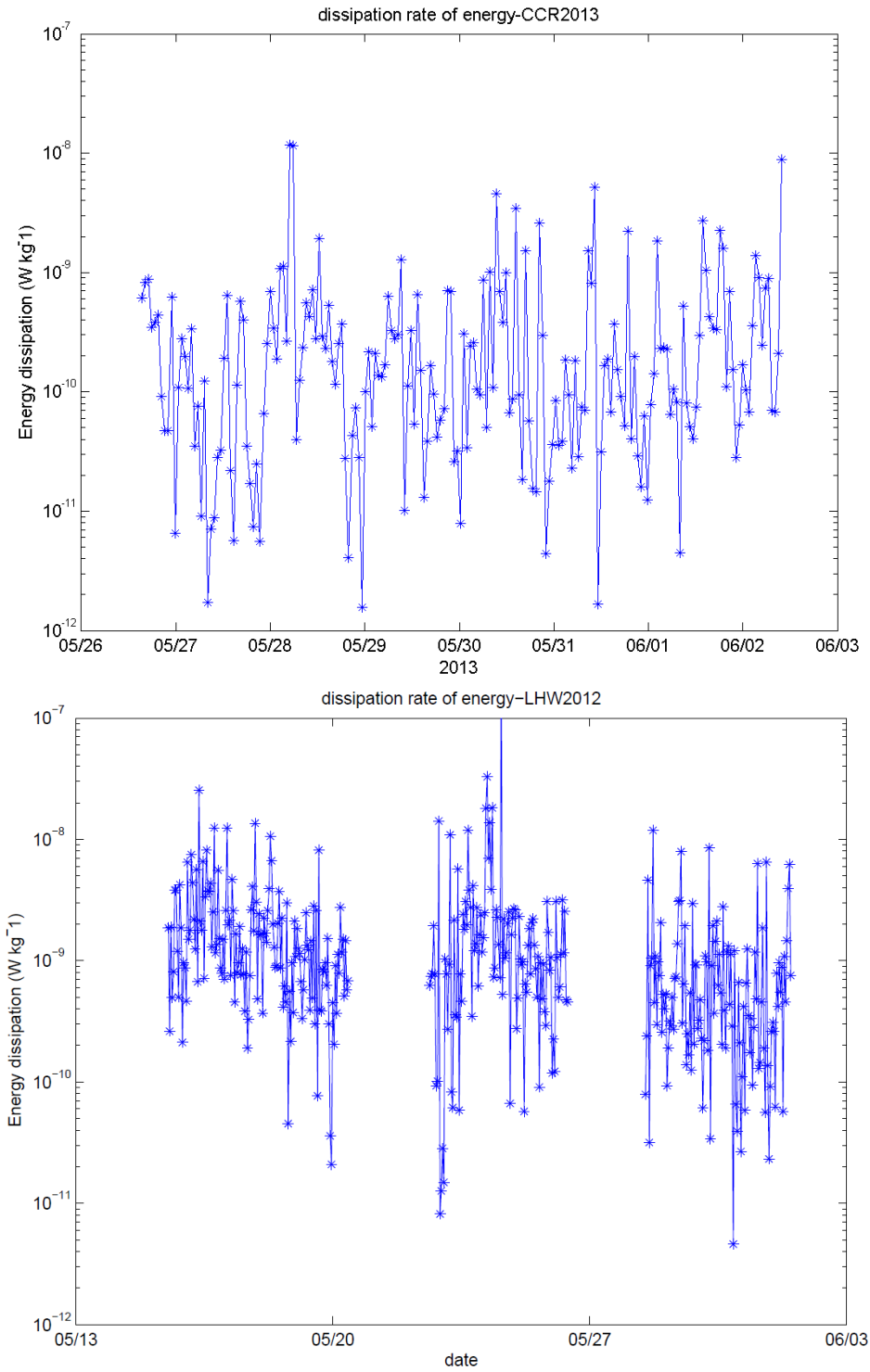
Figure 44. Time series of turbulence dissipation rates

4.5.2   *Estimating different time scales of turbulence*

The turbulent eddy dissipation rate ε is the only flow parameter required for the Lorke and Peeters, (2006) interface exchange model. For the film renewal model, we also require an estimate of the refresh period.

Several methods can be applied to measure the large eddy turn-over time scale. The first and simplest method is based on the Prandtl mixing layer theory, and assumes that the largest turbulent eddies at a point in a boundary layer are proportional to the distance away from the boundary, z. Laboratory turbulent boundary layer measurements show this behavior and lead to using the distance from the wall as an estimate for the integral length scale. Escudier (1966) assumed $l_m = \kappa y$ where l_m is the mixing length, and $\kappa = 0.41$ is Von Karman's constant. Time scales estimated using this approach with mean advective velocity as the integral velocity scale are less than of order one minute at a height of $z = 0.15$ m above the bed, the measurement location of the ADV, and are, comparable to the Kolmogorov time scale.

Doron et al. (2001) showed these integral length scales are associated with the vertical velocity fluctuations (not the horizontal velocity fluctuations) thus there can exist large-scale horizontal eddies (with vertical axes) whose sizes do not depend on elevation. Hence, this estimate of the large eddy turn-over time scale is a low estimate.

The second method calculates the integral time scale using the direct method. Current velocities measured by the ADV were used to derive the normalized autocorrelation function and its integral, the integral time scale, according to:

109

$$r(\tau) = \frac{\overline{u(t)u(t+\tau)}}{\overline{u^2}}$$

(22)

$$\text{T} = \int_0^\infty r(\tau)\, d\tau$$

(23)

Integral time scales T were obtained by considering the area of the correlogram $r(\tau)$ up to the first point where it reached the zero value. Integral time scale is calculated using 5 minutes segments of the time series (Figure 45), and the integral time scales obtained are less than a minute, consistent with results from mixing length theory. Holtappels and Lorke (2011) calculated the autocorrelation over 5 minutes of data from an ADV located 1 m from bottom in a lake and reported integral time scales in the order of 10 seconds. At the same time, using their reported dissipation rates, if we calculate the Kolmogorov time scale for the same time series, will result in around 20 seconds, which is twice as large as their estimated integral time scale based on the autocorrelation function. As the dissipation rates decrease, the estimated Kolmogorov time scales get even larger which implies there are larger integral time scales that may not be captured by ADV measurements, where noise or other deterministic events are interfering. This leads us to use a different theory, based on the dissipation rate and calculate the large eddy turnover size and compute the time that largest eddies last.
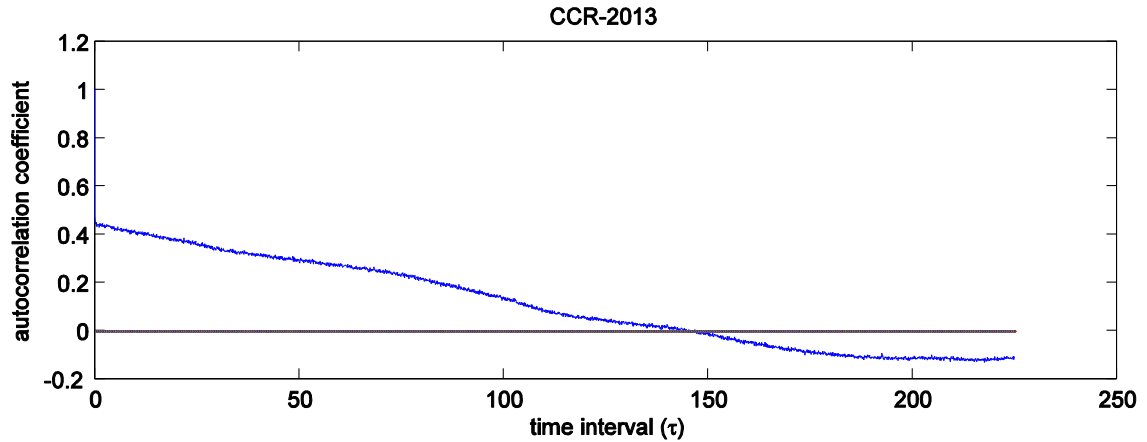
Figure 45. Autocorrelation coefficient calculated as a function of the time interval

Because of the very low ε, suggesting the possibility of long, large eddy turn-over time scales we applied a third method to estimate the large eddy turn-over time scale that does not require long time series of very low-noise data. This third method is based on the analytical formulas for estimating the large eddy turn-over times based on the dissipation rates. By definition, $t_l = \dfrac{L_0}{u_0}$ where u_0 and L_0 are characteristic velocity scales and lengthscales of the energy containing eddies. Pope, (2000) suggests taking $u_0 = k^{\frac{1}{2}}$. The large eddy turn-over length scale may be estimated in terms of Q and ε as $\varepsilon = A\dfrac{Q^3}{L_0}$

Hence; $L_0 = A\dfrac{Q^3}{\varepsilon}$ (Tennekes and Lumley, 1972). Following the concept of turbulent energy cascade where A is a constant which Mellor (1973) found to be equal to 1/15.5 (Asher and Pankow, 1986); Q is defined as the square root of twice the average turbulent kinetic energy, i.e.,

$$Q = (\overline{u'^2} + \overline{v'^2} + \overline{w'^2})^{1/2} = 2\ u_0 \qquad\qquad (24)$$

111

Estimates of t_I from the daily average dissipation rates based on this method are presented in Table 6. Theoretical time scales calculated using dissipation data. The theoretical equations are producing rather large time scales which were not obtained from the integral time scales calculated from velocity measurements. These estimates are of similar order to the renewal rates estimated in Table 6 in section 4.4.1 based on the direct measurements of J_{O2}. Hence, these values for the large eddy turn-over time scale appear consistent with the structure of the turbulence and the large eddy film renewal model.

Table 6. Theoretical time scales calculated using dissipation data

	Date	Kolmogrov time scale (s)	Integral time scale(s)-theory
CCR 2013	5/26/2013	79.38	3876.2
	5/27/2013	34.82	852.4
	5/28/2013	79.56	4846
	5/29/2013	51.81	1957.8
	5/30/2013	55.17	2132.4
LH 2012	5/16/2012	21.97	780.49
	5/17/2012	22.53	1007.05
	5/18/2012	24.52	631.67
	5/19/2012	35.10	823.77
	5/24/2012	11.59	1608.57
	5/25/2012	33.66	843.89
	5/26/2012	37.79	1490.8
	5/29/2012	31.38	1169.99
	5/30/2012	39.06	1284.034
	5/31/2012	52.36	1867.41

4.5.3   *Thermal stratification and internal motions*

An important mechanism controlling the lake response to external forcing (e.g., wind, inflows, outflows, and diffuser operation) is the thermal stratification. The stratification inhibits vertical mixing and sustains internal waves. Imberger, (1998) showed that most of the momentum and energy resulting from wind forcing is transferred to the basin scale internal wave motion, which becomes the primary store of energy available for currents and mixing in the deep lake water in the absence of significant inflows and outflows. While steady diffuser operations would only weakly affect internal waves (e.g., through a boundary or blocking effect), changes in diffuser operations may contribute to internal wave motion through the resulting changes in the buoyancy provided by the bubble plumes. In this section we analyze the thermistor chain, weather, and ADV data to understand the internal wave conditions in these lakes during the measurement campaigns and to determine whether the diffuser operation had any effect on basin-scale motions.

Figure 46 shows the raw thermister data versus time for both lakes at two thermister chain locations, one close to the diffuser and one farther away. The diffuser flow rate is also shown for the reference. Both lakes were strongly stratified during the measurements, having large temperature differences between the surface and bottom layers. When the diffuser is operational, the temperature fluctuations at each thermister are larger near the diffuser than farther away. This is true throughout the water column, but especially in the lower thermistor sensors. For example, the standard deviation of the temperature signal in the second to deepest thermister in LH (40 m depth) is 0.13 ºC

about 30 m from the diffuser and reduced to 0.09 ℃ about 120 m from the diffuser when

the diffuser is operating and was 0.11 ℃ at 30 m from the diffuser and 0.11 ℃ at 120 m

from the diffuser when the diffuser was turned off. This shows that close to the diffuser

there is a relative increase of 15 % in temperature variation for LH during bubbling.

The diffuser-induced variability close to the diffuser can also be observed in the

coherency spectra. Figure 47 shows the coherency spectra of the temperature signal at

9.5 m depth between the two thermister chain locations in CCR for two periods of

constant diffuser operations (i.e operating at 51 and 0 NCMH). Cohrence spectra were

found for 3 hour (10800 samples) window. The spectra were computed using 75%

overlapping windows where linear detrending and a hanning window were applied to

each window before computing the periodogram. The coherency spectra show that there

is more coherency in high frequencies when the diffuser is not operating, which

confirms that greater variability is induced by the bubbling. This type of variability has

been measured before in the nearfield of lake aeration plumes (McGinnis et al., 2004)

and results from the downward flowing dense water detrained from the bubble plumes

and falling to a level of neutral buoyancy.
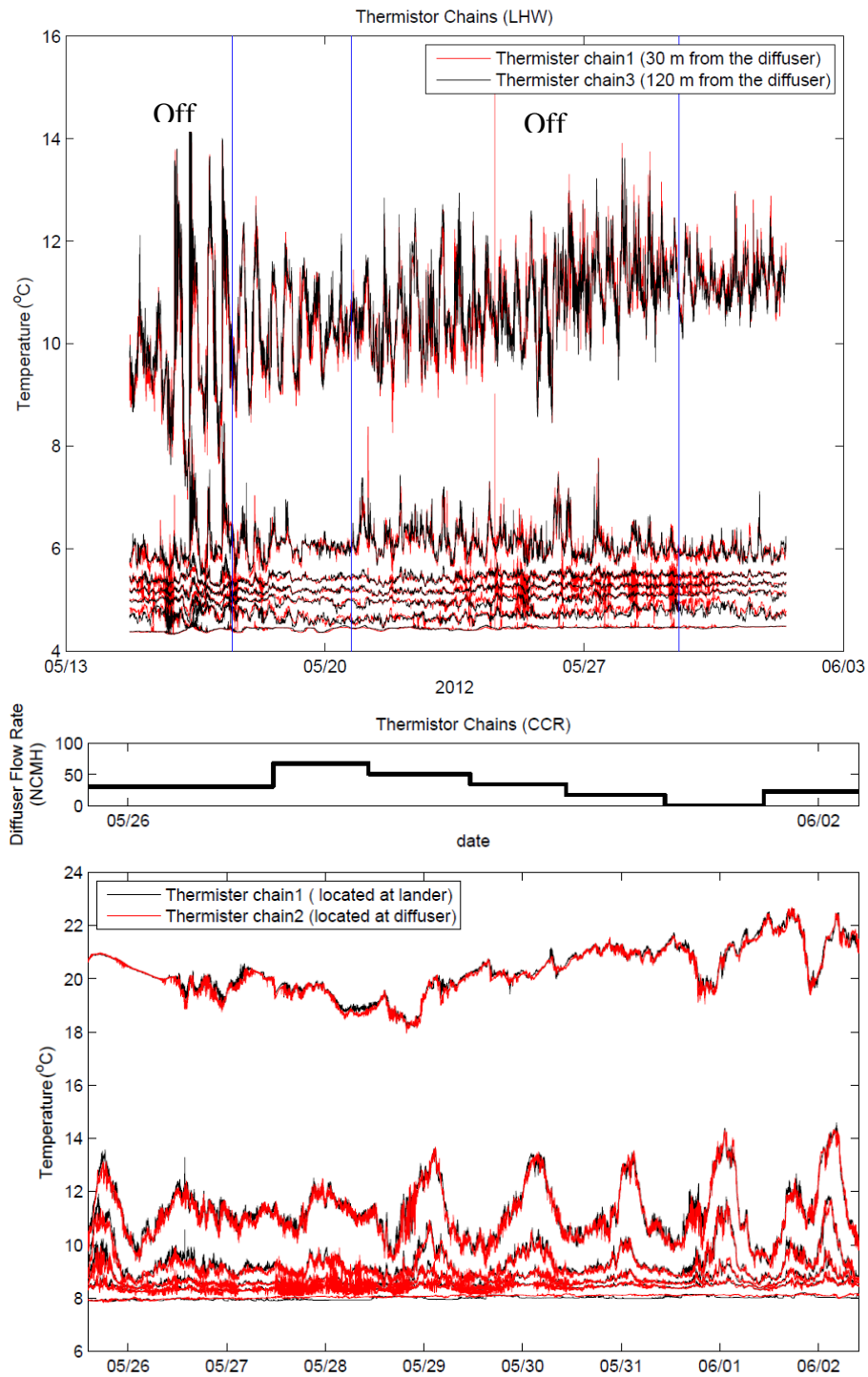
Figure 46. Comparison of temperature variations at 2 locations for CCR2013 (up) and LH2012 (down), the periods of off diffuser is specified on the figure for LH 2012
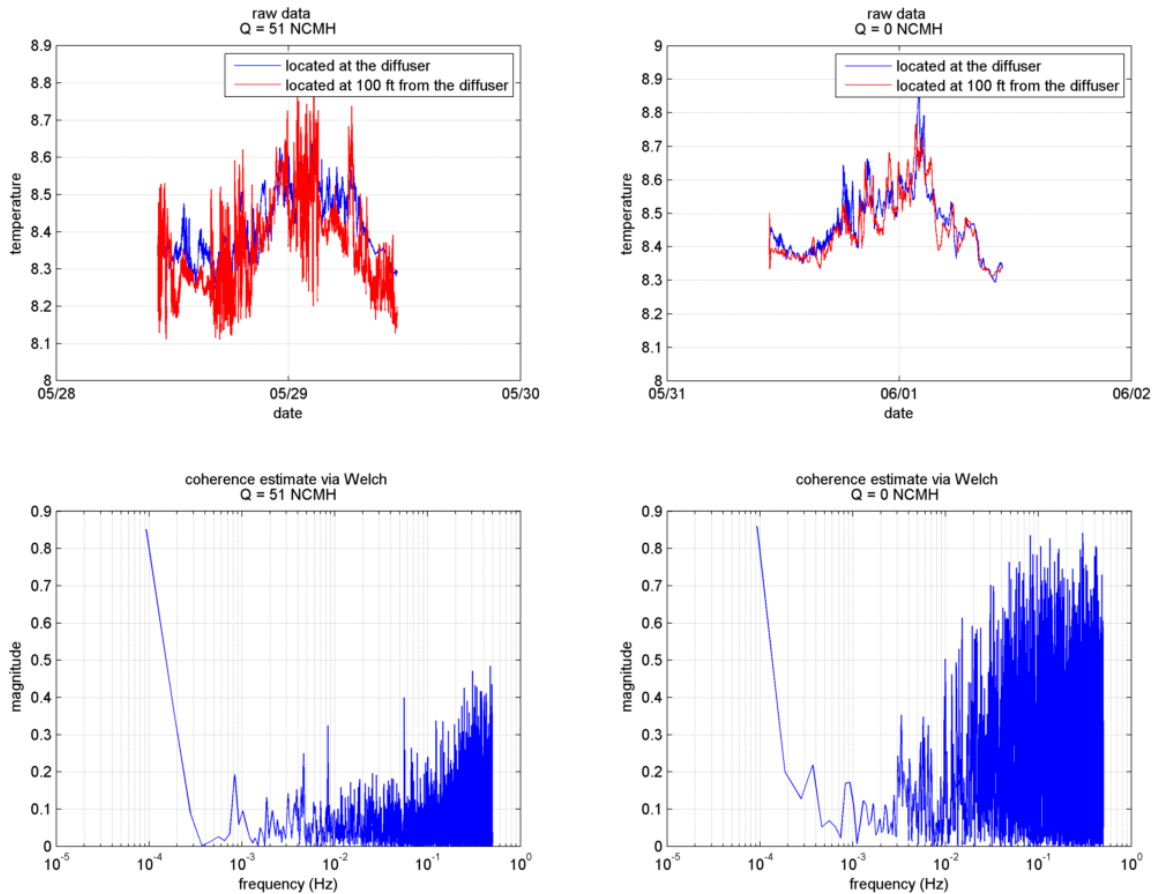
Figure 47. Magnitude-squared of coherence for CCR2013 when Q = 51 NCMH (left side) and Q = 0 NCMH (right side)

The ADV data further supports the fact that the mixing near the diffuser is more rigorous. As an example, consider the dissipation rates from the first deployment in LH as shown in Figure 48. Dissipation rates were evaluated using the velocity data measured at the tripod close to the diffuser (30 m from the diffuser) and the data set measured at the tripod deployed 200 m away from the diffuser. As Figure 48 shows, the dissipation varied between 10^{-8} to 10^{-11} Wkg^{-1} and were slightly enhanced close to the oxygenation system while the diffuser was operating. When the diffuser was turned off, there is no noticeable trend in dissipation differences between these two measurement locations.
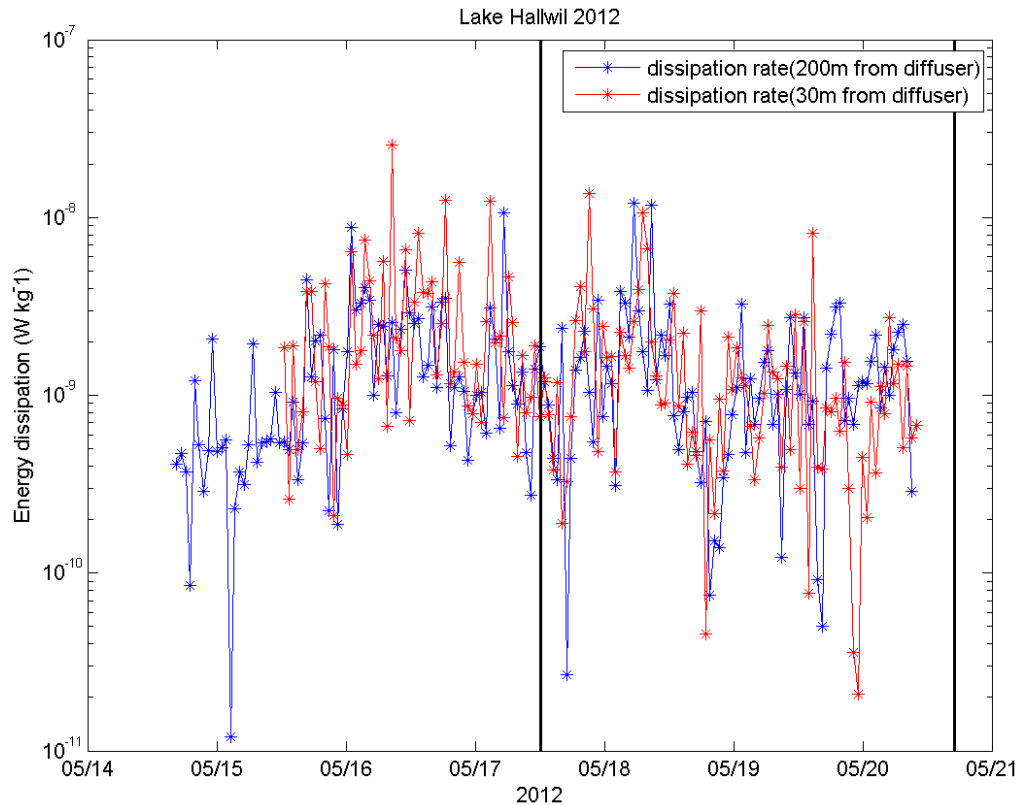
Figure 48. Time series of turbulence dissipation rates (first deployment LH2012), diffuser being turned off from 05/17 until 05/20

These measures have considered local mixing near the diffuser. As a first approximation of the bulk lake mixing status, we compute the empirical Lake Number L_N. This physical index can parse out the contribution of wind as a driver and explain the potential for diapycnal mixing events (Stevens and Imberger, 1996). L_N has been used to give an indication of the strength of the wind compared to stratification and describes the processes relevant to the internal mixing of lakes induced by wind forcing compared to a lake's complex stratification and bathymetry. Lower values of L_N demonstrate a higher potential for increased diapycnal mixing. We utilized the numerical code, Lake Analyzer

117

(Read et al., 2011), to obtain time series data for L_N from the wind, bathymetry, and temperature measurements. L_N is defined as:

$$L_N = \frac{S_T(Z_e + Z_h)}{2\rho_h u_*^2 A_s^{1/2} z_v}$$ (25)

where Z_e and Z_h are the depths to the top and bottom of the metalimnion, respectively, S_T is the Schmidt stability as defined in Read et al., (2011), ρ_h is the density in the hypolimnion, A_s is the surface area of the lake, z_v is the center of volume of the lake, and u* is the water friction velocity due to wind stress on the lake surface.

Figure 49 presents the time series of water temperatures and L_N for the two lakes over the field campaign. Strong stratifications in both lakes lead to L_N values being typically high, representing low likelihood of diapycnal fluxes. Both lakes have a similar range of L_N values, with means of order 10 and peaks of order 100 with the greater variability in LH. The lowest and highest values of L_N occur in LH, with significant diurnal variation. Values in CCR are more steady, or sustained; high wind speed averages for the first two days at CCR led to lake numbers below 10, followed by a sustained period below 30 for 4 more days when the wind ceased. Events with values below 10 in LH occur for two days near the beginning of the campaign and another two days later, with significant periods of elevated L_N (in the range of 30 to 80) between them. This suggests that LH is slightly more stable, with lower values of L_N lasting for a shorter duration and with sustained periods of slightly higher L_N between mixing events.
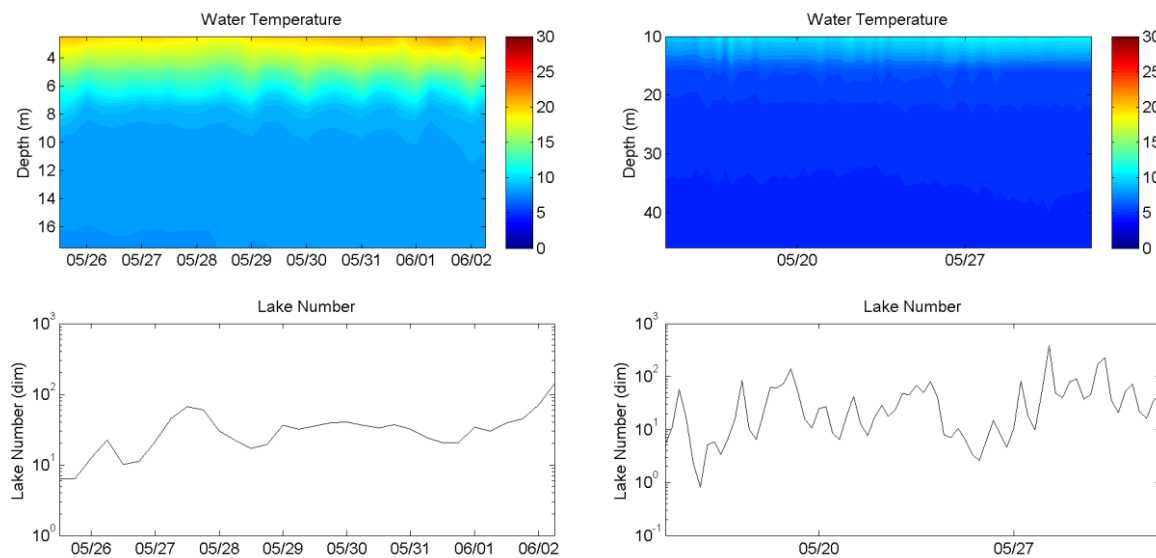
Figure 49. Time series of water temperatures and Lake Number and for CCR2013 (left column) and LH2012 (right column)

To study the energy and periodicity of the internal motions in each lake, we apply spectral analysis to isotherm or isopycnal displacements (Lemmin, 1987). We calculated the isotherm-depth fluctuations for CCR2013 for the 8.3 $^{\circ}$C and 9 $^{\circ}$C isotherms by linear interpolation of the multi-depth temperature data from the thermistor chain records. The time trace of the calculated isotherms are presented in Figure 50.
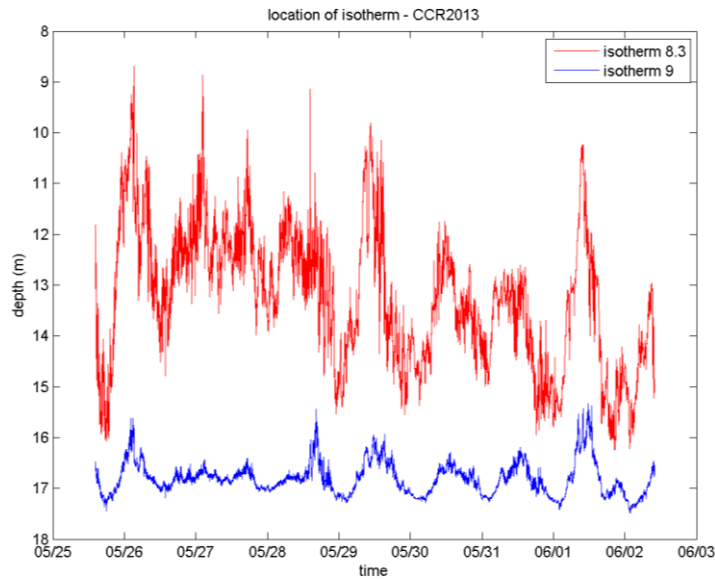
Figure 50. Selected isotherm-depth fluctuations for CCR 2013

The power spectra of these isotherm displacements are presented in Figure 51. Spectral densities are computed from thermister data over the whole duration of deployment and averaged over periods of 50 hours. Both lakes have different dominant frequencies and energy levels. The three most important frequency peaks for each lake are identified in the figure. These were 25 hr, 6 hr, and 2 hr for CCR and 12.5 hr, 5 hr, and 4.16 hr for LH. These differences in frequencies result from their different bathymetry and thermal structure. The spectra for CCR also shows a more pronounced peak in the low-frequency range around 1 cpd, suggesting that on average, there exist a greater basin-scale response and a slightly higher energy level in the spectra as a whole than compared to LH.
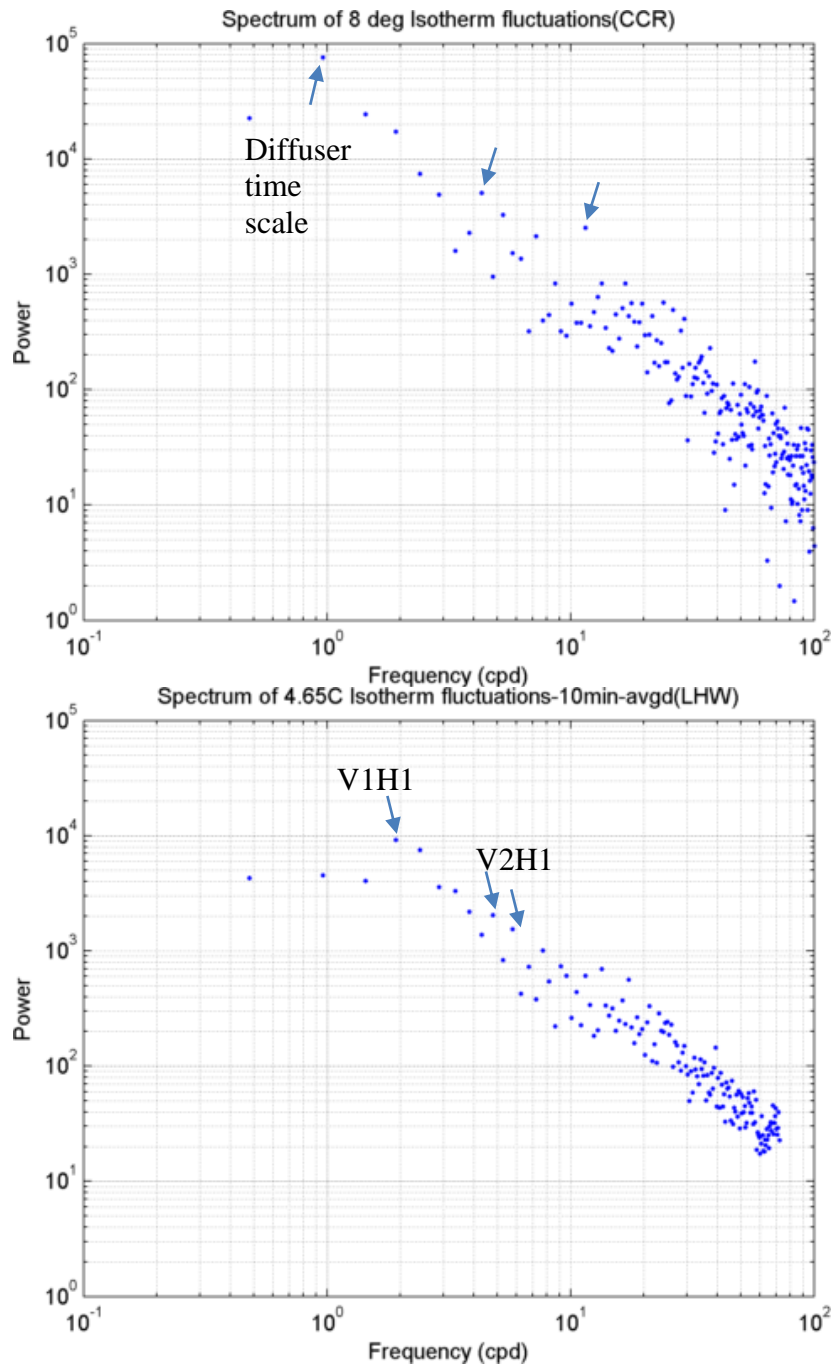
Figure 51. Spectra of isotherm-depth fluctuations

These internal motions are generated through complicated processes that combine the instantaneous stratification with the basin bathymetry and wind forcing.

One way to interpret the present results is through numerical simulations (Antenucci et al., 2000; Münnich et al., 1992). Gwaze (2003) identified the types of waves present in lake Hallwil by numerically approximating the seiching periods of the first vertical first horizontal (V1H1) and the second vertical first horizontal (V2H1) modes using a three layer model and the Merian formula. Results of their measurements revealed the presence of a dominant longitudinal V1H1 seiching mode with a period around 12 hours during the stratification season which is consistent with the first frequency peak observed from our spectra. The 5 hour peak period observed in our spectral analysis likely corresponds to V2H1 transverse mode. The appearance of this transverse mode indicates that the internal wave does not necessarily only travel along the long axis of the basin.

In addition to the unsteady winds setting up internal motion, we may also expect an influence from unsteady operation of the diffuser. When the diffuser is on, it could setup the thermocline, and turning it off or changing the diffuser rate could trigger internal motion as the thermocline sets down in proportion to the flow rate change. We expect this effect to be more noticeable in the isotherm spectra for CCR since the diffuser flow rate was progressively lowered on a daily basis during the campaign. In LH, the diffuser flow rate was changed twice (on then off), in an aperiodic way; hence internal wave effects would not be periodic.

Indeed, the spectral analysis for CCR shows a dominant peak at 25 hours, consistent with the period of diffuser operational changes. To explore the source of this peak, in Figure 52, we plot a comparison between the time series of the wind speed,

isotherm elevations, and diffuser operation in CCR. Beginning mid-day on May 28, a

significant feature of the isotherm displacement is an initial set down of the isotherms

followed by a wave peak about every 24 hours. This coincides with when the diffuser

flow began to change, and also tracks the expected physics for a diffuser-initiated seiche.

The wind forcing is also periodic, but exhibits several peaks each day and a stable mean.

Figure 53, for instance, shows the spectral analysis of the wind speed, and there does not

appear to be a significant energy peak at 24 hours. Hence, these data indicate that the 25

hour internal mode in CCR may have been excited by the diffuser operation.
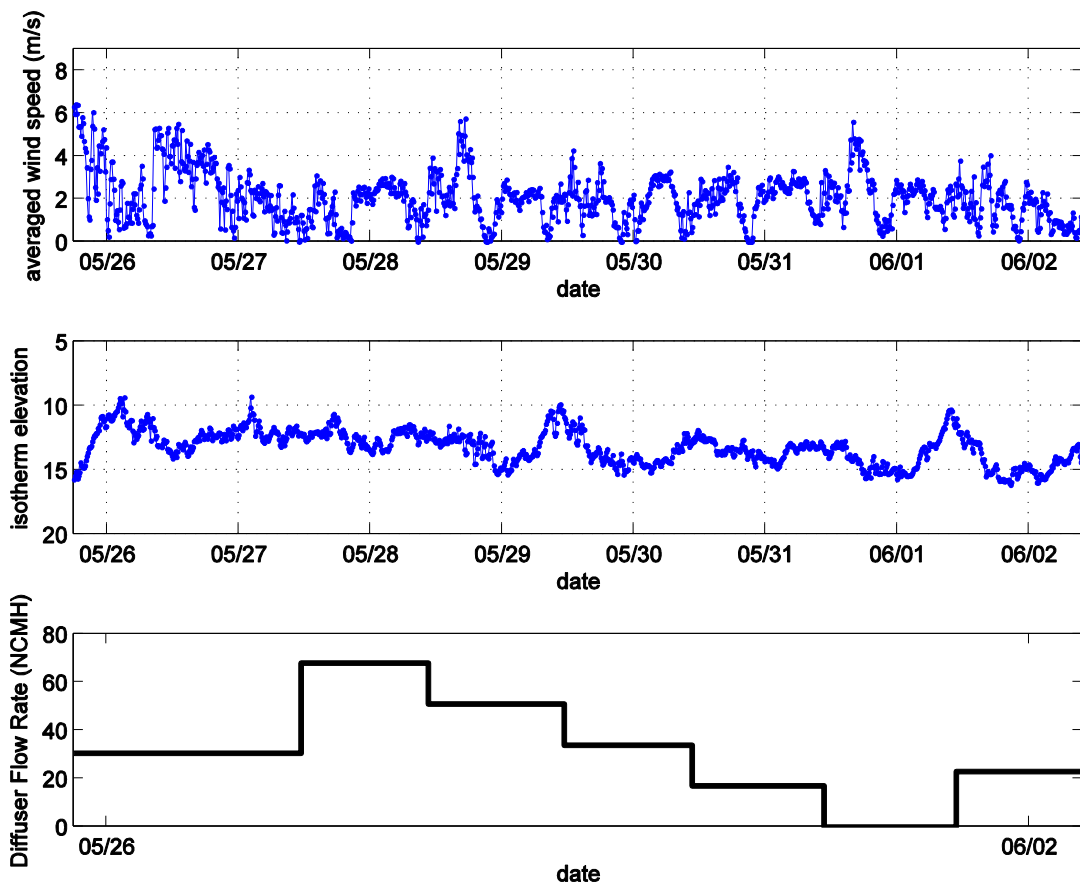
Figure 52. Time series of wind speed and isotherm elevations along with the diffuser operation
for CCR2013
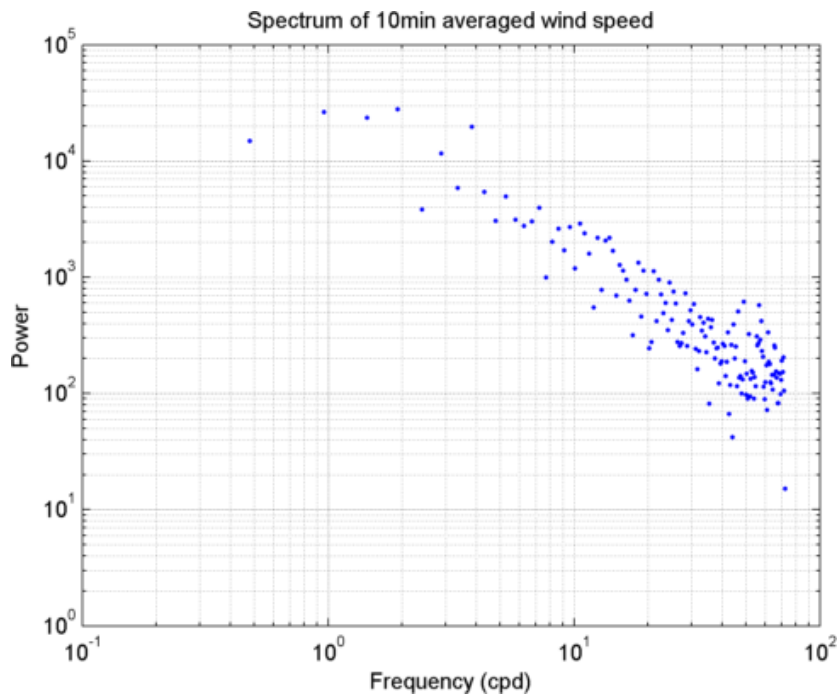
Figure 53. Power spectra of wind speed for CCR2013

4.5.4   *Bottom boundary layer response*

The internal wave motions result in periodic currents moving along the lake
bottom; similar features to the isotherm displacement can be seen in the ADV velocity
data in the BBL. Figure 54 shows the spectrum of the speed measured by the ADV in the
BBL over the whole measurement period in CCR. The same 25 hour peak is observed in
the ADV data as in the isotherm displacement spectrum, along with a few other peaks,
including a diurnal peak at 12 hours. Thus, this internal wave mode generates periodic
currents in the BBL that are superposed on other periodic motions.
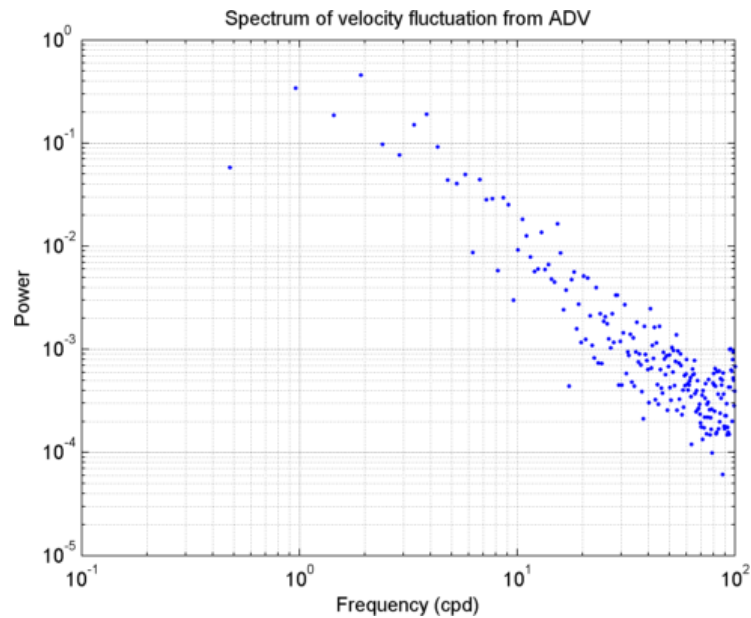
Figure 54. Power spectra of velocity fluctuations measured by Vector (CCR2013)

One measure of the mixing energy of the BBL flow is the dissipation rate already presented for the 50 minute data in Section 4.5.1, above. Another measure is the turbulent kinetic energy. The velocity time signals measured contain periodic motion and turbulent motion. To decompose the time signal into the periodic and turbulent motion, we use a triple decomposition approach. To extract the periodic motion, we applied a low-pass filter and selected a moving average with width of 60 minutes. This moving average was applied to the raw time series which was demeaned on a daily basis and produced time series that contain only the periodic motion. Turbulent kinetic energy was then calculated from the pure turbulent part of the flow, where the mean and periodic motion was removed, and was compared with the internal motion amplitudes to investigate the relationship between the existing turbulence and internal motions. The results are shown in Figure 55 for CCR2013. Each plot corresponds to one day of constant diffuser flow rate operation. The comparison shows an overall similar

125

magnitude of TKE of about 10^{-6} m^2/s^2 for all days. The amplitudes of the coherent

motions (as shown in the bottom panel) show a consistent wave with 24 hour period

superimposed with waves of shorter periods. The values of the TKE and amplitude of

the periodic motion are also correlated, with larger TKE corresponding to higher

amplitudes of the periodic motion.
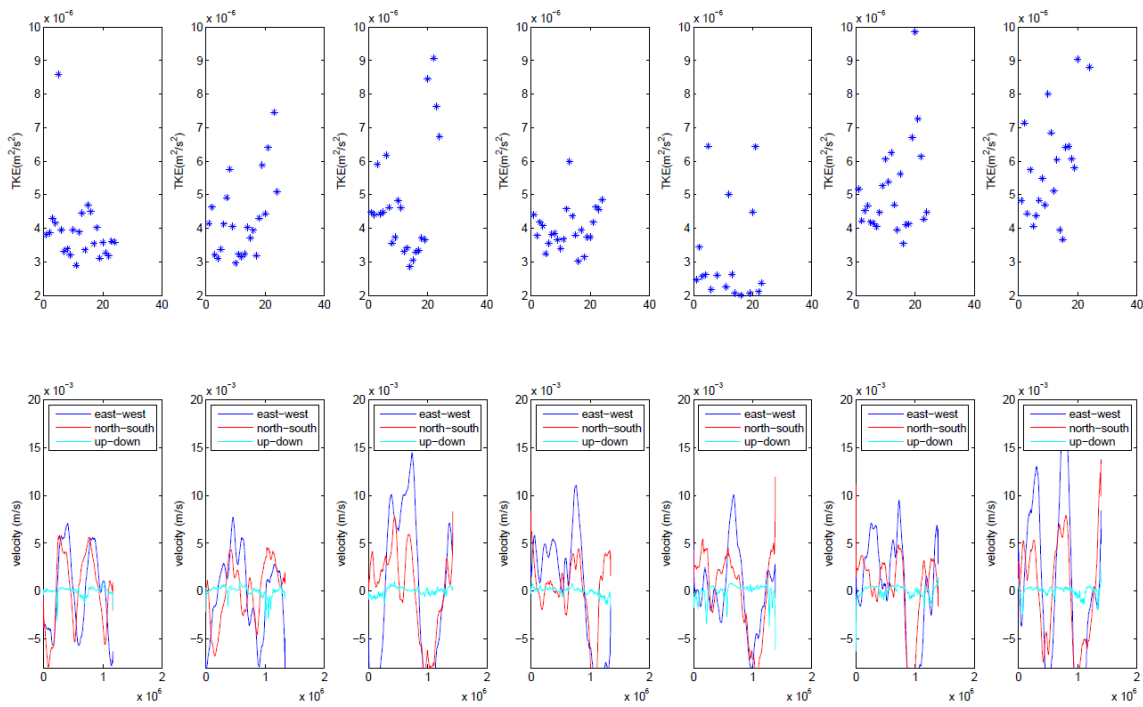
Figure 55. Plots of TKE and low-pass averaged velocity for each constant operation of diffuser
(CCR2013)

The unsteady velocity in the BBL is also visible in the ADCP data. Figure 56

shows the raw measurements from the ADCP for CCR2013.
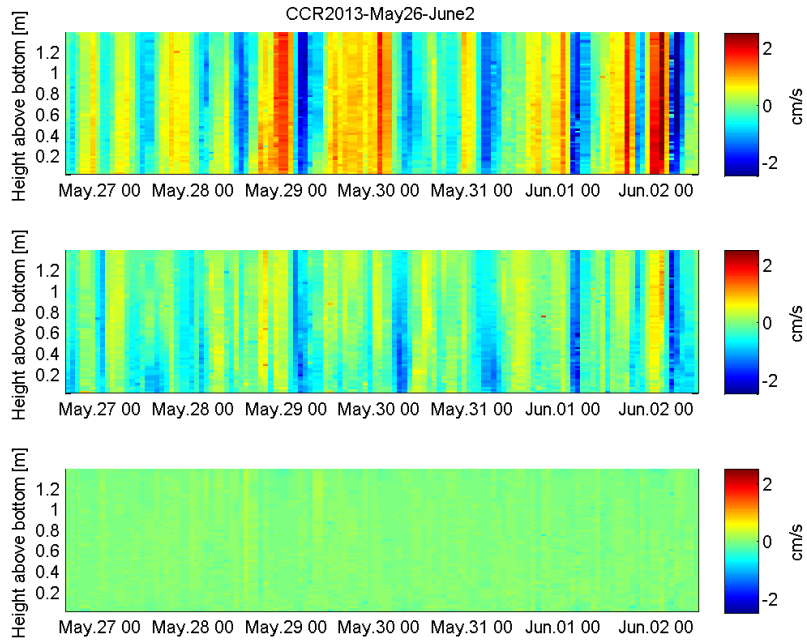
Figure 56. ADCP raw velocity measurements for CCR2013

As seen in the Figure 56, velocities demonstrate an unsteady behavior switching between directions consistent with the periodic motion sampled by the ADV*. We transform the data to be aligned with the longitudinal flow axis on a daily basis. We analyze the BBL response on a daily time step. Previously, we computed the longitudinal axis for 50 min time series by rotating the axes so that the time average flux is zero in the transverse axes. For the daily time series analyzed here, where the longitudinal axis is unsteady, we apply the method of Emery and Thomson (1997). We rotate the data series along its principal axes on which most of the variance is associated with a major axis and the remaining variance with a minor axis. Principal axes can be found from the principal angle by which the coordinates should be rotated. The principle angles θp are the angles that sum of the squares of the normal distances to the data points

$u_1^{'}$ and $u_2^{'}$ are extremum and can be found from the transcendental relation as proposed in Emery and Thomson (1997).

$$\tan 2\theta_p = \frac{\overline{2u'_1 u'_2}}{\overline{u'^2_1} - \overline{u'^2_2}}$$

(26)

where $u_1^{'}$ and $u_2^{'}$ are the turbulent part of east-west, and north-south component of current velocity. For the case of LH, the resulting dominant direction of flow showed good agreement with the orientation of the long axis of the lake.

To view vertical profiles of the ADCP velocity data, velocities were averaged over 8.53 minute bursts, which is the period of our measurements on each measurement cycle. As explained in the Methods section, we exclude ADCP data up to 10 cm from the bottom to avoid the side-lobe interference region. Figure 57 depicts a sample of the velocity profiles of the longitudinal current velocity of bottom boundary measurements for CCR2013 on May 28-29. This plot shows the complete flow reversal resulting from the dominant 24 hr. internal wave mode. Over this period, the currents can vary from slack to maximum velocity over one wave period.
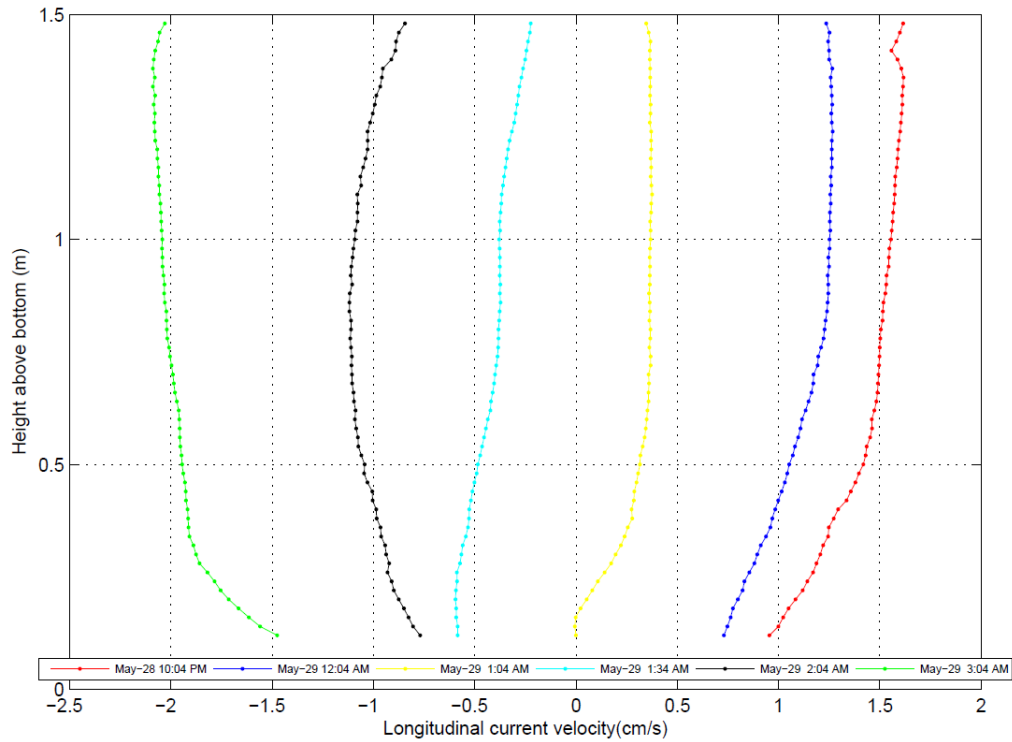
Figure 57. Sample profiles of the longitudinal velocity profiles. Boundary layer velocity profiles obtained from the down-ward looking high resolution ADP showing the current slowing down

4. 6. Synthesis of J_{O2} and lake physics data

4.6.1 Predictive model for J_{O2} in reservoir numerical models

Figure 58 compares the results of the daily measured oxygen fluxes (see Section 4.4.1) to those predicted by the Lorke and Peeters, (2006) and large eddy film renewal model. The dissipation rate used in the Lorke and Peeters, (2006) model was given by Section 4.4.3. In the large eddy model, the renewal time was taken from the expression in Section 4.5.1. In this section we make the model comparison at a daily time step. The renewal times estimated from the J_{O2} measurements and the large eddy turn-over time scale of the turbulence are of order 100 min and longer. Hence, each 50 min profile and J_{O2} measurement is more representative of an instantaneous measurement than an

average response to the turbulence. Hence, the models would not be expected to predict these data. A daily step was selected to give 5 to 10 renewal cycles per data point, hence, expected to give results consistent with the models.
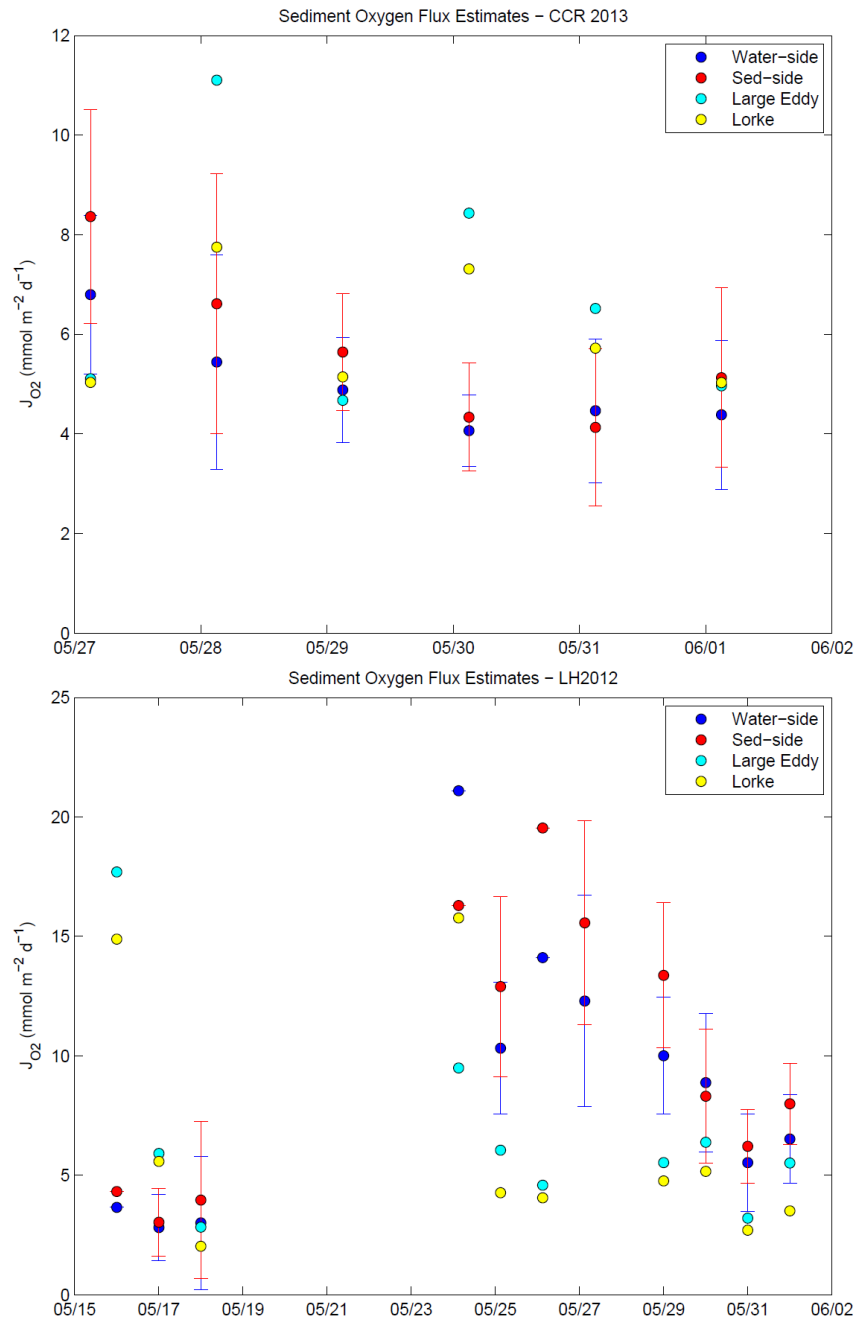
Figure 58. Comparison between interfacial flux model predictions and field measurements for a) CCR2013 and b) LH2012.

To quantify the difference between the predicted and observed fluxes, we use the root-mean-square deviation (RMSD):

Table 7. Root mean square deviation (RMSD), in mmol m^{-2} d^{-1}, of daily average value from interfacial flux models comparing to observed.

	Large Eddy (mmol m^{-2} d^{-1})	Lorke and Peeters (mmol m^{-2} d^{-1})	n
CCR2013	1.45	0.64	6
LH2012	2.37	2.82	11

As shown in Table 7, RMSD results demonstrate a better performance of the large-eddy film renewal model in LH2012, while the Lorke and Peeters model performs better in CCR2013. However, both models seem to provide reasonable estimates of the fluxes in both lakes with RMSD in the order of 20% of the measured values.

To test the scaling law of the Lorke and Peeters, (2006) model, Figure 59 presents the transfer velocities calculated directly from the J_{O2} measurements, normalized by the Schmidt number, as a function of the measured turbulence dissipation rate; similarly to Lorke and Peeters, (2006) in their paper. Data in CCR agree somewhat with the line representing the Lorke and Peeters model, meanwhile the agreement is slightly less for some of the observed transfer velocities in LH. Although the agreement appears less than in the Lorke and Peeters (2006) paper, these results extend the range of experimental data that was presented by them to lower values of dissipation rates; hence, the overall trend agrees with the model line.
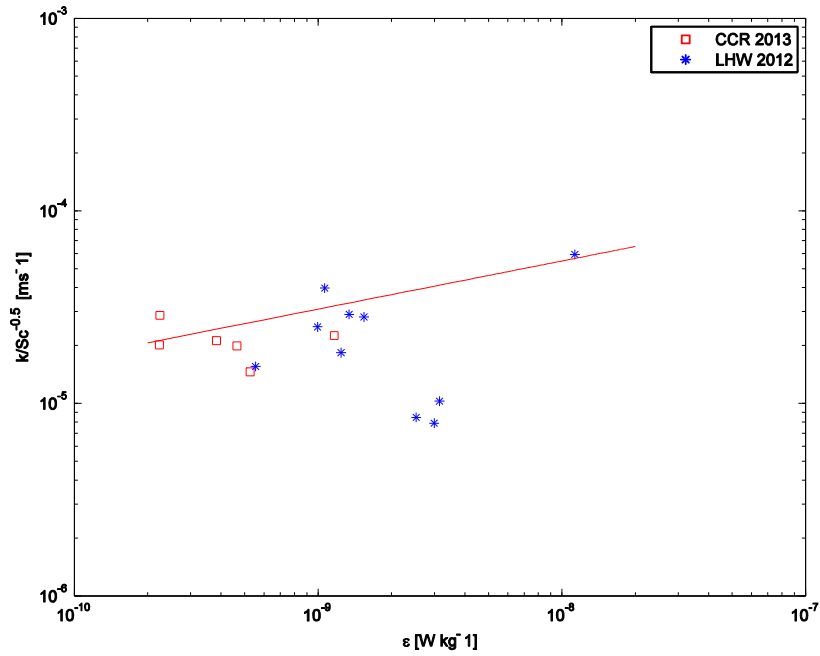
Figure 59. Transfer velocities calculated from oxygen microprofiles and normalized by the Schmidt number versus the observed turbulence dissipation rates calculated from ADV data. The red line represents the universal scaling relationship proposed by Lorke and Peeters (2006).

In this section, we have presented the comparison results based on the daily averages. Figure 60 also presents the comparison results for the dissipation rates as measured in 50 minute segments (left plot) and averaged over 12 hours segments (right plots) for CCR2013. As explained above, the 50 min data are essentially instantaneous, and the scatter in the left plot confirms this expectation. The data at the 12 hour average begin to show structure, and are converging on the daily value.

132
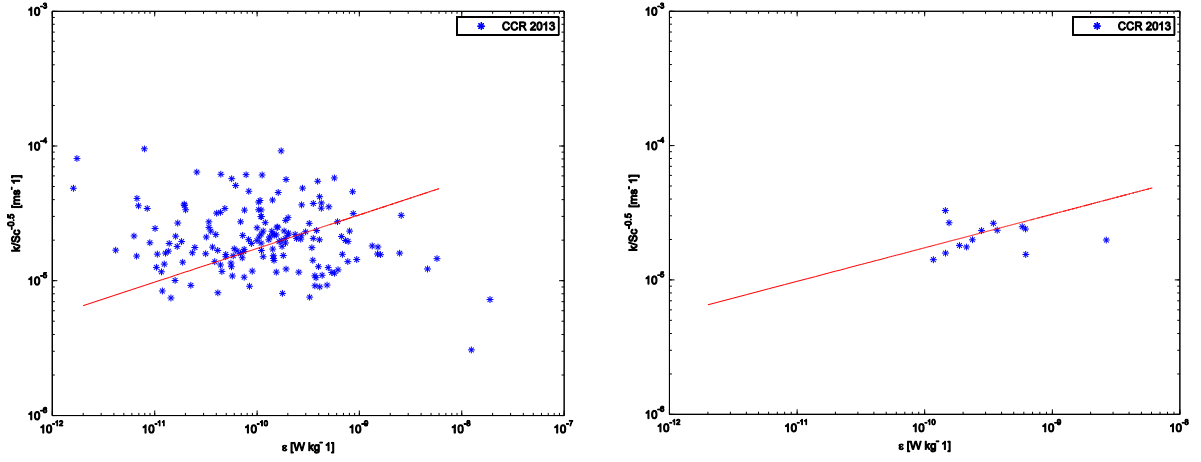
Figure 60. Transfer velocities calculated from oxygen microprofiles and normalized by the Schmidt number versus the observed turbulence dissipation rates calculated from ADV data. The red line represents the universal scaling relationship proposed by Lorke and Peeters (2006). Left plot presents results for 50 minute measurements for CCR2013 and right plot is based on 12 hour time averaged results for CCR2013.

4.6.2 Effects of the diffuser operation on the J_{O2}

Finally, we relate the observed J_{O2} fluxes to the diffuser operation and its effects

on the near-bottom turbulence. As a starting point, we consider the predictive models for

J_{O2} and an analytical analysis of their sensitivity to changes in the bulk oxygen

concentration and the turbulence characteristics. Both of the models are of the form

$$J_{O2} = -k_l \left(C_\infty - C_{SWI} \right) = -k_l \Delta C$$
(27)

where each model hypothesizes a different dependence of k_l on the near bottom

hydrodynamics.

Taking the Lorke and Peeters (2006) model first, we have the equation

$$J_{O_2} = -\frac{1}{2\pi} (\frac{D^2 \varepsilon}{\upsilon})^{1/4} \Delta C$$
(28)

133

From this expression, it is clear that J_{O2} is linearly proportional to ΔC and depends on ε to the quarter power. Hence, halving ΔC would reduce J_{O2} by half while halving ε would reduce J_{O2} by $(1/2)^{1/4}$, or only a factor of 84%. However, from the plots of dissipation rate, it is clear that there is high hour-to-hour and day-to-day variability in ε (e.g., spanning over two orders of magnitude between adjacent measurements in time) while ΔC is much more slowly varying. If ε reduces by a factor of 10, then J_{O2} reduces by 56%, which is similar in sensitivity to reducing ΔC by half.

The large eddy film renewal model is somewhat more complicated since its formulation depends on more than one parameter of the turbulence. Using the analytical model from Pope, (2000) for the large eddy turn over time scale and substituting into the large eddy film renewal model, we have

$$J_{O_2} = \left(\frac{31 D \varepsilon}{\pi k_{TKE}} \right)^{1/2} \Delta C$$

$(\,29\,)$

The sensitivity to ΔC remains linear, but the sensitivity to the turbulence parameters has changed. The dissipation rate now enters the equation to the $\frac{1}{2}$ power while the turbulent kinetic energy goes as the $-\frac{1}{2}$ power. From Figure 55 it is evident that k_{TKE} can vary over about a factor of two among the measured data. It is also expected that k_{TKE} will decrease as ε decreases. If ε decreases by an order of magnitude and k_{TKE} decreases by a factor of two, then J_{O2} will decrease by 55%. Hence, for both of the analytical models, considering the potential range of the concentration differences and

134

the turbulence parameters, J_{O2} is equally sensitive to changes in concentration and turbulence.

As a final study of the analytical nature of the predictive equations, we also consider the error propagation equation for the case of the Lorke and Peeters (2006) model. For uncertainty in ε, the resulting uncertainty in J_{O2} is given by

$$\frac{\partial J_{O_2}}{\partial \varepsilon}\delta\varepsilon = \frac{k_l\Delta C}{4\varepsilon}\delta\varepsilon$$

(30)

where $\delta\varepsilon$ is the standard deviation of the ε uncertainty. Likewise, the uncertainty resulting from variability in ΔC is

$$\frac{\partial J_{O_2}}{\partial\Delta C}\delta\Delta C = k_l\delta\Delta C$$

(31)

where $\delta\Delta C$ is the standard deviation of the uncertainty in ΔC. The error propagation equation weights these errors using a root mean square so that we can compare these two uncertainties by taking the ratio of their squares, given by

$$\left(\frac{\partial J_{O_2}}{\partial\varepsilon}\delta\varepsilon\right)^2 \bigg/ \left(\frac{\partial J_{O_2}}{\partial\Delta C}\delta\Delta C\right)^2 = \frac{1}{16}\frac{c_\varepsilon^2}{c_{\Delta c}^2}$$

(32)

where c_ε and $c_{\Delta c}$ are the coefficients of variation of the ε and ΔC data, respectively. If these data had similar statistics, then uncertainty in ε would be 16 times less important than similar uncertainty in ΔC. From the measurements, $c_{\Delta c}$ is about 0.4 and c_ε is between 5 to 10. Substituting into the above equation gives the ratio of uncertainties to be order of 1. Hence, uncertainty in J_{O2} originates about equally from uncertainty in ΔC and in the turbulence parameters. This is in agreement with the direct sensitivity of J_{O2} to

changes in these parameters over their measured ranges, summarized in the previous paragraphs. Thus, we conclude that both changes in the bulk concentration and changes in the turbulence properties may equally effect J_{O2}. To understand the role of the diffuser on oxygen uptake, it remains to compare the measurements of J_{O2} and the concentration and turbulence data to changes in the diffuser operation.

Figure 61 shows the changes in these parameters for one case at LH. The DO concentration is plotted together with the J_{O2} measurements in the upper panel of the figure; the corresponding dissipation rate measurements are shown in the lower panel. These measurements were made 30 m outside the diffuser ring, and the diffuser operated at a combined flow rate of 130 Nm^3/h until it was shut off on May 30 (shown as the vertical black line in the upper panel). The mean values of J_{O2} and ε over the periods before and after turning off the diffuser are also shown in the plots for reference. The net change in the average J_{O2} shows a reduction from 11 to 7 mmol/(m^{2}d), or a factor of 40%. At the same time, the bulk concentration decreases from about 5 mg/l during bubbling to 3 mg/l shortly after turning off the diffuser. This is also a reduction of 40%, suggesting that the changes in J_{O2} may be explained by changes in the bulk background concentration. The variability in the dissipation rate data shows similar spread during both periods, with a reduction in the mean value form about 6.10^{-10} to 2.10^{-10} W/kg. This is a reduction of 3 times which, for the Lorke and Peeters (2006) model, would yield a reduction in J_{O2} of about 25%, which is the same order of magnitude as the observed change, suggesting that turbulence may also play a role. However, there is considerable variability in the ε data so that one might conclude that the turbulence regime is

statistically stationary over this event. In any case, the change in the bulk concentration is large enough to explain the change in J_{O2}, and must be considered a dominant parameter.

To further study the effects of the diffuser operation on the turbulence, the direct correlation between the turbulence dissipation rates and diffuser operation is assessed using data from CCR, in which we have constantly changed the diffuser flow rates and simultaneously measured the dissipation rates. The results are shown in Figure 62 as box plots with the turbulent dissipation rate plotted against the diffuser flow rate. Average dissipation rates range from 2.10^{-11} to 4.10^{-10} W/kg, with a mean value of 10^{-10} W/kg over the complete time series. No consistent trend is observed between dissipation rate and diffuser flow rate. The lowest measurements of dissipation rate did occur when the diffuser was turned off, but similar low values were measured for a diffuser flow rate of 30.6 Nm^3/h. At the same time, dissipation rate both increases and decreases with increasing diffuser flow rate.

Each diffuser flow rate was maintained steady for 24 hours, and we did observe internal waves with about a 24 hour period that appeared to be excited by the changes in the diffuser operation. It is possible that the flat response in dissipation rate to the diffuser flow rate is a result of these internal waves maintaining a similar dynamic regime in the hypolimnion despite reduction in the diffuser flow rate. Thus, if the experiments were repeated, constant diffuser flow rates should be maintained for longer periods of time. Hence, for the data from these two field campaigns, the main factor affecting J_{O2} under different diffuser operations is the resulting change in ΔC for

different oxygen loadings. The background turbulence remains highly variable so that

the effect on J_{O2} is similar for all diffuser operation modes.
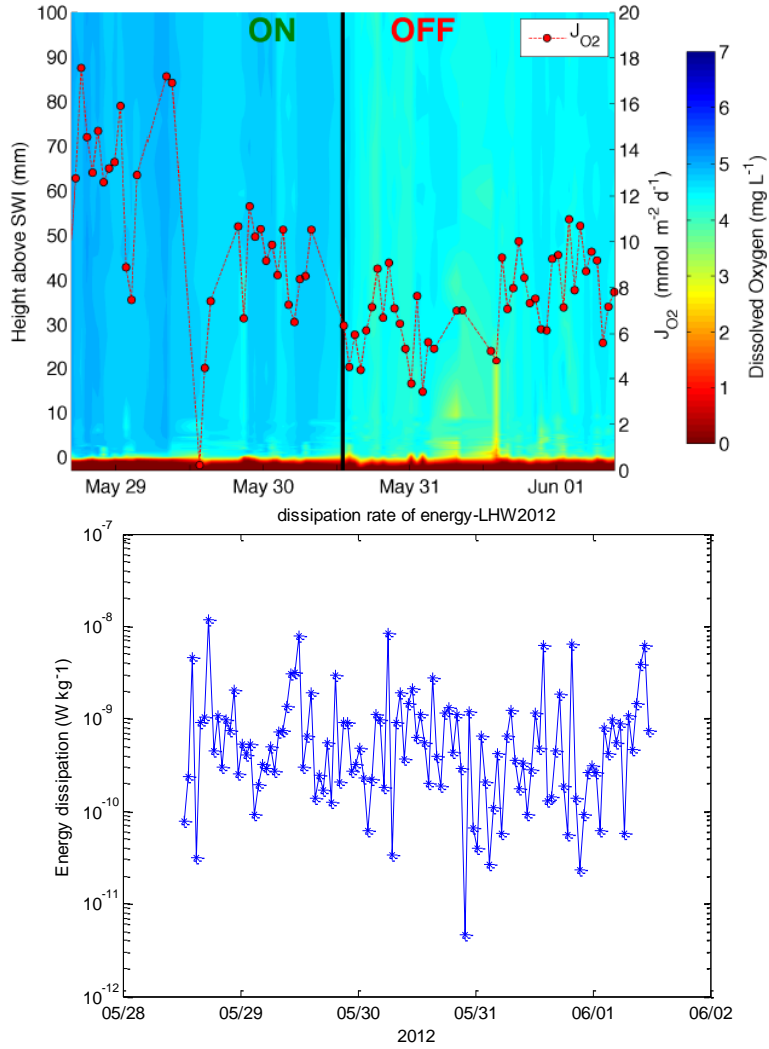

Figure 61. Time series of DO concentrations, J_{O_2}, and dissipation rates (at 10cm above the sediments) measured at the last deployment of LH2012.
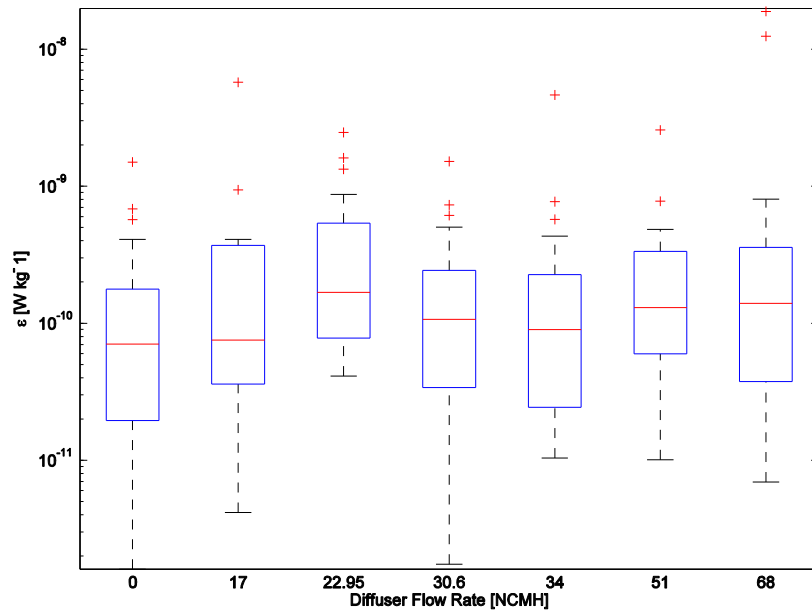
Figure 62. Measured dissipation rates (at 15cm above the sediments) plotted against oxygen diffuser flow rates. Means are represented by red lines, and blue boxes encompass the 25th and 75th percentiles.

4. 7.   Summary and conclusions

Hypolimnetic oxygenation systems, particularly bubble-plume types, are increasingly utilized in managed lakes to increase DO concentrations. Even so, studies show their operation can stimulate an increase in oxygen uptake, with a magnitude that is difficult to predict accurately while designing the systems. This research has done field studies in two different lakes (CCR and LH) to study the effects of bubble plume operation along with other natural phenomenon in enhancing J_{O2} and has used existing models with the field measurements to estimate the oxygen uptake and compare them with the measured values. Understanding the effects of bubble plume operation on near-sediment mixing and oxygen concentrations and improvements in predicting sediment

oxygen uptake will lead to more effective optimization of water quality in managed

lakes and reservoirs.

Mixing conditions have been studied in the study sites using thermister, weather

and velocity data to investigate if unsteady operation of the diffusers would contribute to

the internal wave motion. Observations showed that changes in bubble plume operations

may initiate internal waves. However, these waves have negligible effect on J_{O2} since we

did not observe statistical significance of correlations of model hydrodynamic

parameters to the diffuser operation and J_{O2} was most clearly affected by C_{bulk}. Thus,

oxygenation system operation influences oxygen uptake through increasing DO

concentrations in the bulk water which leads to a stronger concentration gradient across

the SWI which in turn stimulate oxygen uptake. This can be illustrated by the

observations made on Lake Halwill where oxygen flux experiences 40% reduction when

the diffuser was turned off, and simultaneous measurements showed 40% decrease in the

bulk background concentration. Hence, ΔC appears to be the dominant parameter

affecting the flux. Effects of bubble plumes on turbulence are shown to be limited to

close to the diffuser and becoming weak as the distance from diffuser increases.

Models, based either on film renewal or Batchelor length scale analysis, have

been used to predict J_{O2}. We analyzed the turbulence properties and investigated

different time scales that exist in the bottom boundary layer of these two lakes including

the periodic signals which have been shown to be important to the boundary exchange

(Lorke et al., 2003), to choose the appropriate parameters to input the models. The

values predicted by large-eddy film-renewal model based on the theoretical integral time

scales and Lorke and Peeters model, scale well with the measured values. It is important to account for increase in J_{O_2} as a result of diffuser operation when designing and operating the oxygenation systems in the managed lakes. Incorporating these interfacial models into hydrodynamic models of lakes will allow lake managers to better design bubble plumes by predicting the variability in J_{O_2} in response to oxygen systems operations.

5. CONCLUSIONS

5. 1.   Summary

The overarching purpose of this work is to advance analysis tools (i.e., coupled 3D lake models) for both the scientific investigation of hypolimnetic oxygen dynamics and for the management of lakes and reservoirs using bubble plumes. At the same time, these findings advance our fundamental understanding of bubble plumes in crossflows, which is clearly applicable to a variety of environmentally sensitive problems. In particular, this dissertation addresses the existing gaps in current three-dimensional hydrodynamic reservoir models which do not account for the role of bubble plumes in creating mixing or inducing currents in the hypolimnion.

In section 2, the time averaged flow field behind a bubble plume in a horizontal ambient current U_∞ was experimentally investigated using standard measurement techniques, including particle image velocimetry (PIV) and laser-induced fluorescence (LIF). Experiments were conducted in a glass-walled flume 35 m long by 0.9 m wide and 1.2 m deep. Crossflows were simulated in two ways: recirculation crossflow generated by a pump and using a towed source. Air bubbles were generated using an aquarium airstone positioned at the centerline of the flume. Different cases of ambient crossflow and bubble air flow rates were simulated to span a range of separation heights. The major findings were:

1) By comparing results from two set of independent experiments with one using a
   towed plume to simulate crossflow and the other using recirculation crossflow

generated by the pump, it is shown that ambient turbulence does not impact the results, and the analogy of a towed plume to open channel crossflow is validated.

2) Observations made in the wake region reveal that there is no secondary bubble plume above the separation height and that the bubble column above this point is considered to be "exhausted" solely imparting a vertical momentum to the fluid that passes through it.

3) Trajectories of the separated plume in the wake show deviations from the expected $z \sim x^{1/3}$ scaling of advected line puff behavior. This deviation can be attributed to the vertical motion that is experienced by the background flow above the separation height, due to the action of the exhausted plume.

4) A simple conceptual model based on momentum conservation is developed to predict the vertical velocities imparted from the exhausted phase of the bubble column. Model results were correlated with the experimental observations and show fair agreement.

Investigation of the turbulence characteristics of a bubble plume in crossflow was presented in Section 3. Experiments followed the same setup as in Section 2. Instantaneous velocities were quantified using PIV over the whole flow field of the plume wake, utilizing 25 overlapping fields of view. Details of data preprocessing and stitching the field of views were explained in this section. Turbulence intensities and Reynolds stress terms were obtained from the instantaneous data. Turbulence intensities were found to increase with increasing the bubble flow rate but then decrease with increasing the crossflow. Anisotropy in the wake is observed in the wake region and

found to increase with increasing the bubble flow rate and cross flow velocity. Investigation on the mean kinetic energy of the mean flow show that bubbles create mean kinetic energy in the wake region above the separated plume which is transported by the crossflow into the wake.

Section 4 detailed the field campaigns in Carvin's Cove (Virginia, USA) and Lake Hallwil (Lucerne, Switzerland) and presented simultaneous measurements of temperature, wind, turbulence, and J_{O2} in the bottom boundary layer of these lakes. The gas flow rates of the diffuser were manually adjusted to the designed experiments during the field campaigns. Analysis of the data showed that changing the diffuser flow rates can excite internal waves leading to the generation of unsteady currents. Nevertheless, the dominant parameter affecting the sediment oxygen uptake is likely the change in oxygen concentrations induced by the diffuser operation. Existing models of interfacial fluxes were utilized to predict the J_{O2} and were then compared to the direct J_{O2} measurements. Models based on the large eddy film-renewal theory and the Batchelor scale matched well with field observations and could be used to predict J_{O2}.

5. 2.   Recommendations for future research

5.2.1   *Crossflow experiments in the lab*

1) An extension of the experiments in a uniform crossflow could be done with the use of Stereoscopic PIV approaches which permit all three components to be recorded. For better understanding of the interactions between bubbles and crossflow, discrete bubbles in the chain can be setup and studied. Using

144

discrete bubbles would simplify the complexity of getting the flow field in a bubble column with high void fraction.

2) The structure of the flow in the wake region behind a bubble column can be investigated by identifying instantaneous vortices and quantifying their properties. These data are important to characterize the flow structures generating mixing and controlling the instantaneous dilution and concentration fields in multiphase plumes. Turbulence spectra can be investigated to add insight to the turbulence properties and scales in bubble plumes.

3) Numerical modeling: data from experiments presented in this study should be compared to the predictions from numerical models. An LES model is being developed with the same setup as these experiments by the Cardiff School of Engineering which adopts an Eulerian- Lagrangian approach representing bubbles as volume-less lagrangian markers. See Fraga et al (2015) for an example in a quiescent ambient.

5.2.2   Field studies

1) Variable J_{O2} expression along with a model for the bubble plume system can be incorporated into water quality models (Such as ELCOM-CAYDEM), setting J_{O2} to be a predicted variable rather than a fitting parameter to predict the impact of the oxygenation system on lake hydrodynamics and J_{O2}.

REFERENCES

Antenucci, J.P., Imberger, J., Saggio, A., 2000. Seasonal evolution of the basin-scale internal wave field in a large stratified lake. Limnol. Oceanogr. 45, 1621–1638. doi:10.4319/lo.2000.45.7.1621

Asaeda, T., Imberger, J., 1993. Structure of bubble plumes in linearly stratified environments. J. Fluid Mech. 249, 35–57. doi:10.1017/S0022112093001065

Asher, W.E., Pankow, J.F., 1986. The interaction of mechanically generated turbulence and interfacial films with a liquid phase controlled gas/liquid transport process. Tellus B 38B, 305–318. doi:10.1111/j.1600-0889.1986.tb00256.x

Beutel, M.W., 2003. Hypolimnetic Anoxia and Sediment Oxygen Demand in California Drinking Water Reservoirs. Lake Reserv. Manag. - LAKE RESERV MANAG 19, 208–221. doi:10.1080/07438140309354086

Beutel, M.W., Leonard, T.M., Dent, S.R., Moore, B.C., 2008. Effects of aerobic and anaerobic conditions on P, N, Fe, Mn, and Hg accumulation in waters overlaying profundal sediments of an oligo-mesotrophic lake. Water Res. 42, 1953–1962. doi:10.1016/j.watres.2007.11.027

Bierlein, K. A., M. Rezvani, S. A. Socolofsky, L. D. Bryant, and J. C. Little (2015a) Increased sediment oxygen flux in oxygenated lakes: the impact of hypolimnetic oxygenation, Manuscript in preparation.

Bluteau, C.E., Jones, N.L., Ivey, G.N., 2011. Estimating turbulent kinetic energy dissipation using the inertial subrange method in environmental flows. Limnol. Oceanogr. Methods 9, 302–321. doi:10.4319/lom.2011.9.302

Bombardelli, F.A., Buscaglia, G.C., Rehmann, C.R., Rincón, L.E., García, M.H., 2007. Modeling and scaling of aeration bubble plumes: A two-phase flow analysis. J. Hydraul. Res. 45, 617–630. doi:10.1080/00221686.2007.9521798

Bryant, D.B., Seol, D.-G., Socolofsky, S.A., 2009a. Quantification of turbulence properties in bubble plumes using vortex identification methods. Phys. Fluids 21, 075101–075101–10. doi:doi:10.1063/1.3176464

Bryant, D.B., Seol, D.G., Socolofsky, S.A., 2009b. Quantification of turbulence properties in bubble plumes using vortex identification methods. Phys. Fluids 21, 075101.

Bryant, L.D., Gantzer, P.A., Little, J.C., 2011. Increased sediment oxygen uptake caused by oxygenation-induced hypolimnetic mixing. Water Res. 45, 3692–3703. doi:10.1016/j.watres.2011.04.018

Bryant, L.D., Lorrai, C., McGinnis, D., Brand, A., Wüest, A., Little, J.C., 2010a. Variable sediment oxygen uptake in response to dynamic forcing. Limnol. Oceanogr. 55, 950–964.

Bryant, L.D., McGinnis, D.F., Lorrai, C., Brand, A., Little, J.C., Wüest, A., 2010b. Evaluating oxygen fluxes using microprofiles from both sides of the sediment–

water interface. Limnol. Oceanogr. Methods 8, 610–627.

doi:10.4319/lom.2010.8.0610

Chen, F., Yapa, P.D., 2004. Modeling gas separation from a bent deepwater oil and gas

jet/plume. J. Mar. Syst., Marine Environmental Modelling 2001 - Selected Papers

from the Fifth International Marine Environmental Modelling Seminar 45, 189–

203. doi:10.1016/j.jmarsys.2003.11.005

Clift, R., Grace, J.R., Weber, M.E., 2005a. Bubbles, Drops, and Particles. Courier

Corporation.

Clift, R., Grace, J.R., Weber, M.E., 2005b. Bubbles, drops, and particles. Courier

Corporation.

Cooke, G.D., Carlson, R.E., 1989. Reservoir management for water quality and THM

precursor control. AWWA Research Foundation Denver, CO.

Crounse, B., Wannamaker, E., Adams, E., 2007. Integral Model of a Multiphase Plume

in Quiescent Stratification. J. Hydraul. Eng. 133, 70–76.

doi:10.1061/(ASCE)0733-9429(2007)133:1(70)

Davidson, M., Pun, K., 1999. Weakly Advected Jets in Cross-Flow. J. Hydraul. Eng.

125, 47–58. doi:10.1061/(ASCE)0733-9429(1999)125:1(47)

Doneker, R.L., Jirka, G.H., Barnwell, T.O., 1990. Expert system for hydrodynamic

mixing zone analysis of conventional and toxic submerged single port discharges

(CORMIX1). Environmental Research Laboratory, Office of Research and
Development, US Environmental Protection Agency.

Doron, P., Bertuccioli, L., Katz, J., Osborn, T.R., 2001. Turbulence Characteristics and
Dissipation Estimates in the Coastal Ocean Bottom Boundary Layer from PIV
Data. J. Phys. Oceanogr. 31, 2108–2134. doi:10.1175/1520-
0485(2001)031<2108:TCADEI>2.0.CO;2

Fan, L.-N., 1967. Turbulent buoyant jets into stratified or flowing ambient fluids [WWW
Document]. URL http://resolver.caltech.edu/CaltechKHR:KH-R-15 (accessed
7.26.13).

Gantzer, P.A., Bryant, L.D., Little, J.C., 2009. Controlling soluble iron and manganese
in a water-supply reservoir using hypolimnetic oxygenation. Water Res. 43,
1285–1294. doi:10.1016/j.watres.2008.12.019

Gantzer, P.A., Bryant, L.D., Little, J.C., 2009. Effect of hypolimnetic oxygenation on
oxygen depletion rates in two water-supply reservoirs. Water Res. 43, 1700–
1710. doi:10.1016/j.watres.2008.12.053

Ghisalberti, M., Nepf, H.M., 2002. Mixing layers and coherent structures in vegetated
aquatic flows. J. Geophys. Res. Oceans 107, 3–1–3–11.
doi:10.1029/2001JC000871

Gwaze, S. (2003), Structure, dynamics and energetics of internal waves in Lake Hallwil,
M. Sc., UNESCO-IHE Inst. for Water Educ., Delft, Netherlands.

Higbie, R., 1935. The rate of absorption of a pure gas into still liquid during short periods of exposure,. [New York].

H L Grant, R.W.S., 1962. Turbulence spectra from a tidal channel. J Fluid Mech 12, 241–268. doi:10.1017/S002211206200018X

Holtappels, M., Lorke, A., 2011. Estimating turbulent diffusion in a benthic boundary layer. Limnol. Oceanogr. Methods 9, 29–41. doi:10.4319/lom.2011.9.29

Hugi, C., 1993. Modelluntersuchungen von Blasenstrahlen für die Seebelüftung. Institut für Hydromechanik und Wasserwirtschaft, Zürich.

Huttunen, J.T., Väisänen, T.S., Hellsten, S.K., Martikainen, P.J., 2006. Methane fluxes at the sediment–water interface in some boreal lakes and reservoirs. Boreal Environ. Res. 11.

Imberger, J., 1998. Flux Paths in a Stratified Lake, in: Imberger, J. (Ed.), Physical Processes in Lakes and Oceans. American Geophysical Union, pp. 1–17.

Johansen, Ø., 2000. DeepBlow – a Lagrangian Plume Model for Deep Water Blowouts. Spill Sci. Technol. Bull. 6, 103–111. doi:10.1016/S1353-2561(00)00042-6

Jørgensen, B.B., Revsbech, N.P., 1985. Diffusive boundary layers and the oxygen uptake of sediments and detritus1. Limnol. Oceanogr. 30, 111–122. doi:10.4319/lo.1985.30.1.0111

Josiam, R.M., Stefan, H.G., 1999. Effect of Flow Velocity on Sediment Oxygen Demand: Comparison of Theory and Experiments1. JAWRA J. Am. Water Resour. Assoc. 35, 433–439. doi:10.1111/j.1752-1688.1999.tb03601.x

Lance, M., Bataille, J., 1991. Turbulence in the liquid phase of a uniform bubbly air–water flow. J. Fluid Mech. 222, 95. doi:10.1017/S0022112091001015

Lee, J.H.J.H.W., Chu, V.H., 2003. Turbulent Jets and Plumes: A Lagrangian Approach. Springer.

Lemckert, C., Imberger, J., 1993. Energetic Bubble Plumes in Arbitrary Stratification. J. Hydraul. Eng. 119, 680–703. doi:10.1061/(ASCE)0733-9429(1993)119:6(680)

Lemmin, U., 1987. The structure and dynamics of internal waves in Baldeggersee1. Limnol. Oceanogr. 32, 43–61. doi:10.4319/lo.1987.32.1.0043

Lewis, W.K., Whitman, W.G., 1924. Principles of Gas Absorption. Ind. Eng. Chem. 16, 1215–1220. doi:10.1021/ie50180a002

Little, L., McGinnis, M., 2001. Hypolimnetic oxygenation: predicting performance using a discrete-bubble model [WWW Document]. URL http://www.iwaponline.com/ws/00104/ws001040185.htm (accessed 5.4.14).

Lorke, A., Muller, B., Maerki, M., Wuest, A., 2003. Breathing sediments: The control of diffusive transport across the sediment-water interface by periodic boundary-layer turbulence. Limnol. Oceanogr. 48, 2077–2085.

Lorke, A., Peeters, F., 2006. Toward a Unified Scaling Relation for Interfacial Fluxes. J. Phys. Oceanogr. 36, 955–961. doi:10.1175/JPO2903.1

Lorke, A., Umlauf, L., Jonas, T., Wüest, A., 2002. Dynamics of Turbulence in Low-Speed Oscillating Bottom-Boundary Layers of Stratified Basins. Environ. Fluid Mech. 2, 291–313. doi:10.1023/A:1020450729821

Lorke, A., Wüest, A., 2005. Application of Coherent ADCP for Turbulence Measurements in the Bottom Boundary Layer. J. Atmospheric Ocean. Technol. 22, 1821–1828. doi:10.1175/JTECH1813.1

Manasseh, R., Yoshida, S., Kajio, N., 1998. 'Bubble Trajectory Bifurcations in Cross Flow, in: Proceedings, 13th Australasian Fluid Mechanics Conference. pp. 13–18.

Mcdougall, T.J., 1978. Bubble plumes in stratified environments. J. Fluid Mech. 85, 655–672. doi:10.1017/S0022112078000841

McGinnis, D.F., Lorke, A., Wüest, A., Stöckli, A., Little, J.C., 2004. Interaction between a bubble plume and the near field in a stratified lake. Water Resour. Res. 40, W10206. doi:10.1029/2004WR003038

Mellor, G.L., 1973. Analytic Prediction of the Properties of Stratified Planetary Surface Layers. J. Atmospheric Sci. 30, 1061–1069. doi:10.1175/1520-0469(1973)030<1061:APOTPO>2.0.CO;2

Milgram, J.H., 1983. Mean flow in round bubble plumes. J. Fluid Mech. 133, 345–376.
doi:10.1017/S0022112083001950

Moore, B.C., Chen, P.-H., Funk, W.H., Yonge, D., 1996. A Model for Predicting Lake
Sediment Oxygen Demand Following Hypolimntetic Aeration1. JAWRA J. Am.
Water Resour. Assoc. 32, 723–731. doi:10.1111/j.1752-1688.1996.tb03469.x

MÜnnich, M., WÜest, A., Imboden, D.M., 1992. Observations of the second vertical
mode of the internal seiche in an alpine lake. Limnol. Oceanogr. 37, 1705–1719.
doi:10.4319/lo.1992.37.8.1705

Nepf, H.M., 1999. Drag, turbulence, and diffusion in flow through emergent vegetation.
Water Resour. Res. 35, 479–489.

Nepf, H.M., Sullivan, J.A., Zavistoski, R.A., 1997. A model for diffusion within
emergent vegetation. Limnol. Oceanogr. 42, 1735–1745.
doi:10.4319/lo.1997.42.8.1735

Owen, T., n.d. Vector — Nortek AS [WWW Document]. URL http://www.nortek-
as.com/lib/manuals/vector/view (accessed 7.6.15).

Pope, S.B., 2000. Turbulent flows. Cambridge university press.

Pun, K.L., Davidson, M.J., 1999. On the behaviour of advected plumes and thermals. J.
Hydraul. Res. 37, 519–540. doi:10.1080/00221686.1999.9628266

Read, J.S., Hamilton, D.P., Jones, I.D., Muraoka, K., Winslow, L.A., Kroiss, R., Wu, C.H., Gaiser, E., 2011. Derivation of lake mixing and stratification indices from high-resolution lake buoy data. Environ. Model. Softw. 26, 1325–1336. doi:10.1016/j.envsoft.2011.05.006

Rensen, J., Luther, S., Lohse, D., 2005. The effect of bubbles on developed turbulence. J. Fluid Mech. 538, 153–187. doi:10.1017/S0022112005005276

Saddoughi, S.G., Veeravalli, S.V., 1994. Local isotropy in turbulent boundary layers at high Reynolds number. J. Fluid Mech. 268, 333–372. doi:10.1017/S0022112094001370

Schlichting, H., 1979. Boundary-layer theory. McGraw-Hill.

Seol, D., Bhaumik, T., Bergmann, C., Socolofsky, S., 2007. Particle Image Velocimetry Measurements of the Mean Flow Characteristics in a Bubble Plume. J. Eng. Mech. 133, 665–676. doi:10.1061/(ASCE)0733-9399(2007)133:6(665)

Seol, D.-G., Bhaumik, T., Bergmann, C., Socolofsky, S.A., 2007. Particle Image Velocimetry Measurements of the Mean Flow Characteristics in a Bubble Plume. J. Eng. Mech. 133, 665–676. doi:10.1061/(ASCE)0733-9399(2007)133:6(665)

Seol, D.-G., Socolofsky, S.A., 2008a. Vector post-processing algorithm for phase discrimination of two-phase PIV. Exp. Fluids 45, 223–239. doi:10.1007/s00348-008-0473-9

Seol, D.-G., Socolofsky, S.A., 2008b. Vector post-processing algorithm for phase discrimination of two-phase PIV. Exp. Fluids 45, 223–239. doi:10.1007/s00348-008-0473-9

Simiano, M., Zboray, R., de Cachard, F., Lakehal, D., Yadigaroglu, G., 2006. Comprehensive experimental investigation of the hydrodynamics of large-scale, 3D, oscillating bubble plumes. Int. J. Multiph. Flow 32, 1160–1181. doi:10.1016/j.ijmultiphaseflow.2006.05.014

Singleton, V.L., Gantzer, P., Little, J.C., 2007. Linear bubble plume model for hypolimnetic oxygenation: Full-scale validation and sensitivity analysis. Water Resour. Res. 43, W02405. doi:10.1029/2005WR004836

Singleton, V.L., Rueda, F.J., Little, J.C., 2010. A coupled bubble plume–reservoir model for hypolimnetic oxygenation. Water Resour. Res. 46, W12538. doi:10.1029/2009WR009012

Socolofsky, S.A., Adams, E.E., 2002a. Multi-phase plumes in uniform and stratified crossflow. J. Hydraul. Res. 40, 661–672. doi:10.1080/00221680209499913

Socolofsky, S.A., Adams, E.E., 2002b. Multi-phase plumes in uniform and stratified crossflow. J. Hydraul. Res. 40, 661–672.

Socolofsky, S., Adams, E., 2005. Role of Slip Velocity in the Behavior of Stratified Multiphase Plumes. J. Hydraul. Eng. 131, 273–282. doi:10.1061/(ASCE)0733-9429(2005)131:4(273)

Socolofsky, S.A., Jirka, G.H., 2005. Special topics in mixing and transport processes in the environment. Eng. Fifth Ed Coast. Ocean Eng. Div. Tex. AM Univ.

Socolofsky, S., Bhaumik, T., Seol, D., 2008. Double-Plume Integral Models for Near-Field Mixing in Multiphase Plumes. J. Hydraul. Eng. 134, 772–783. doi:10.1061/(ASCE)0733-9429(2008)134:6(772)

Sreenivasan, K.R., 1995. On the universality of the Kolmogorov constant. Phys. Fluids 1994-Present 7, 2778–2784. doi:10.1063/1.868656

Stefan, H.G., 1992. Sedimentary Oxygen Demand and Its Effect on Winterkill in Lakes,.

Stevens, C., Imberger, J., 1996. The initial response of a stratified lake to a surface shear stress. J. Fluid Mech. 312, 39–66.

Stoker, R.L., 1946. Methods of Producing Uniform Velocity Distribution. Ind. Eng. Chem. 38, 622–624.

Tekeli, S., Maxwell, W.H.C., 1978. Behavior of Air Bubble Screens. Department of Civil Engineering, University of Ill.

Tian, X., Roberts, P.J.W., 2003. A 3D LIF system for turbulent buoyant jet flows. Exp. Fluids 35, 636–647. doi:10.1007/s00348-003-0714-x

Uittenbogaard, R.E., Cornelisse, J.M., O'Hara, K., 2015. Water–air bubble screens reducing salt intrusion through shipping locks, in: Proceedings of the 36th IAHR World Congress.

Willis, G.E., Deardorff, J.W., 1976. On the use of Taylor's translation hypothesis for diffusion in the mixed layer. Q. J. R. Meteorol. Soc. 102, 817–822. doi:10.1002/qj.49710243411

Wright, S.J., 1984. Buoyant Jets in Density-Stratified Crossflow. J. Hydraul. Eng. 110, 643–656. doi:10.1061/(ASCE)0733-9429(1984)110:5(643)

Wright, S.J., 1977. Effects of ambient crossflows and density stratification on the characteristic behavior of round, turbulent bouyant jets.

Wright, S.J., 1977. Mean behavior of buoyant jets in a crossflow. J. Hydraul. Div. 103, 499–513.

Wüest, A., Brooks, N.H., Imboden, D.M., 1992. Bubble plume modeling for lake restoration. Water Resour. Res. 28, 3235–3250. doi:10.1029/92WR01681

Wüest, A., Lorke, A., 2003. Small-Scale Hydrodynamics in Lakes. Annu. Rev. Fluid Mech. 35, 373–412. doi:10.1146/annurev.fluid.35.101101.161220

Wu, R.S.S., Zhou, B.S., Randall, D.J., Woo, N.Y.S., Lam, P.K.S., 2003. Aquatic hypoxia is an endocrine disruptor and impairs fish reproduction. Environ. Sci. Technol. 37, 1137–1141. doi:10.1021/es0258327

Yapa, P., Chen, F., 2004. Behavior of Oil and Gas from Deepwater Blowouts. J. Hydraul. Eng. 130, 540–553. doi:10.1061/(ASCE)0733-9429(2004)130:6(540)

Yapa, P.D., Li, Z., 1997. Simulation of oil spills from underwater accidents I: Model development. J. Hydraul. Res. 35, 673–688. doi:10.1080/00221689709498401

Yapa, P., Zheng, L., Nakata, K., 1999. Modeling Underwater Oil/Gas Jets and Plumes. J. Hydraul. Eng. 125, 481–491. doi:10.1061/(ASCE)0733-9429(1999)125:5(481)

Zhang, W., Zhu, D.Z., 2014. Trajectories of Air-Water Bubbly Jets in Crossflows. J. Hydraul. Eng. 140, 06014011. doi:10.1061/(ASCE)HY.1943-7900.0000886

Zhang, W., Zhu, D.Z., 2013. Bubble characteristics of air–water bubbly jets in crossflow. Int. J. Multiph. Flow 55, 156–171. doi:10.1016/j.ijmultiphaseflow.2013.05.003

Zheng, L., Yapa, P.D., Chen, F., 2003. A model for simulating deepwater oil and gas blowouts - Part I: Theory and model formulation. J. Hydraul. Res. 41, 339–351. doi:10.1080/00221680309499980

This appendix presents the summary of field measurements conducted during the field campaigns and not presented in the manuscript. Chapter 4 presents the analysis of the pertaining observations. The observations are presented in two sections, first section includes the measurements conducted in Lake Hallwil 2012, and second section presents measurements from CCR2013.

A.1 Lake Hallwil 2012

Measurements of weather, temperature and velocity in Lake Hallwil campaign are shown in Figure A. 1 - A. 4.
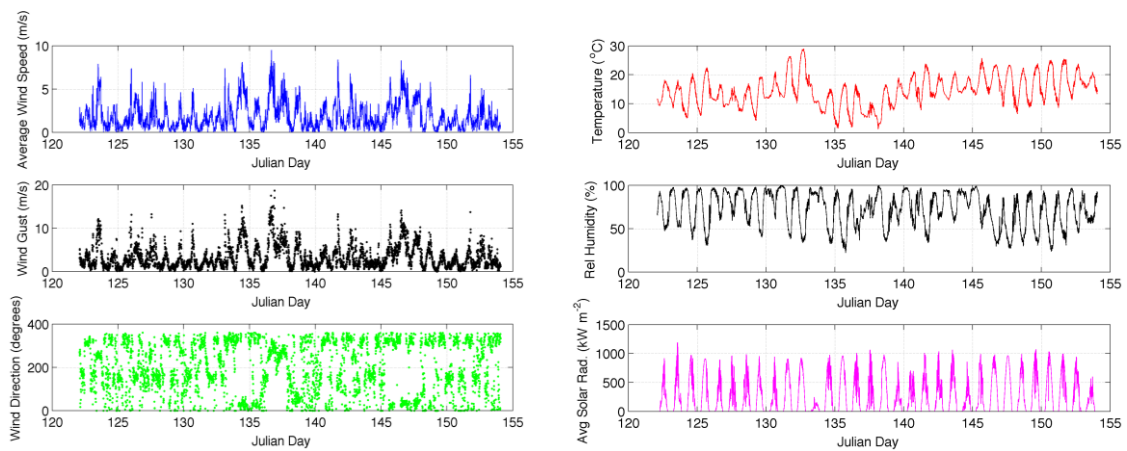
Figure A. 1. Weather measurements; Wind measurements (left side), and Temperature, Humidity, and Solar Radiation (right side)
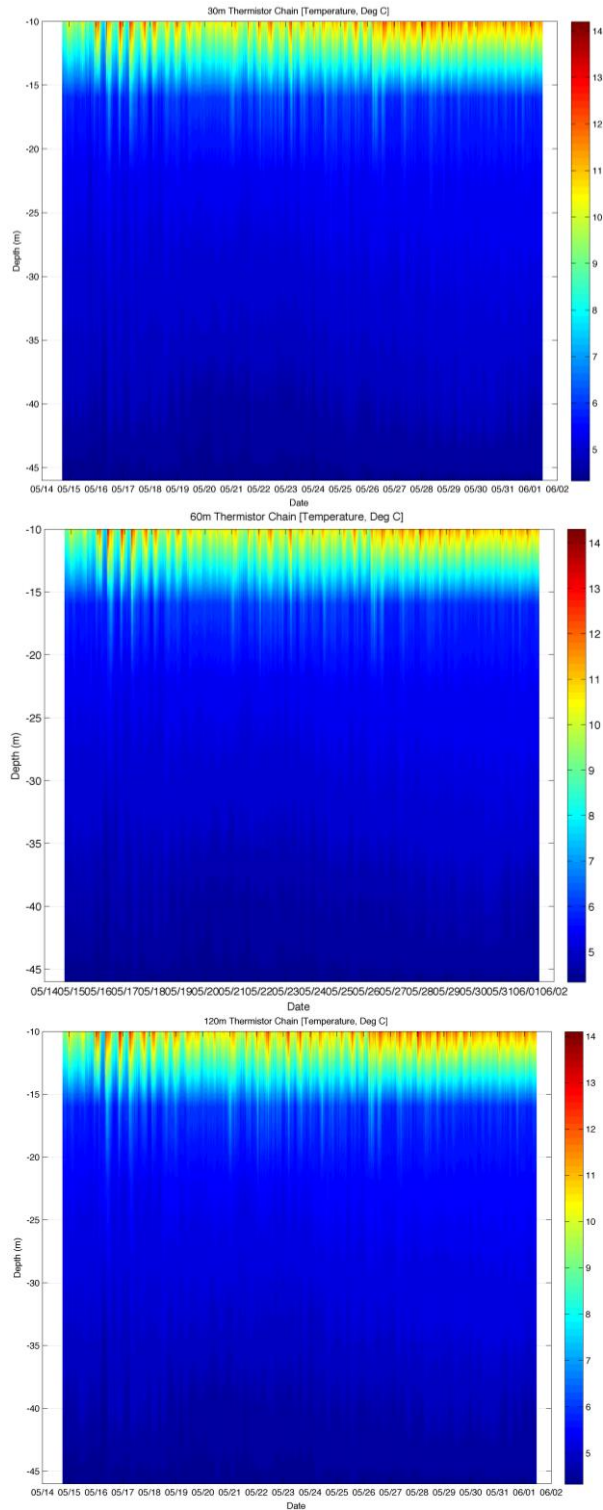
Figure A. 2. Vertical profile of temperature at 30 m (first row), 60m (second row), and 120 m (last row) from the diffuser measured by diffuser chains

160
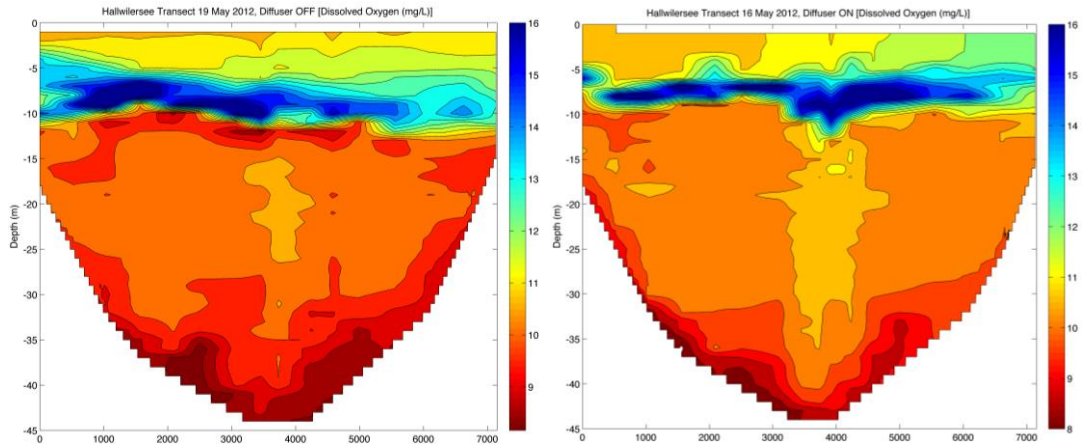
Figure A. 3. Lake Dissolved Oxygen transect when the diffuser is off (left column), and when the diffuser is on (right column)
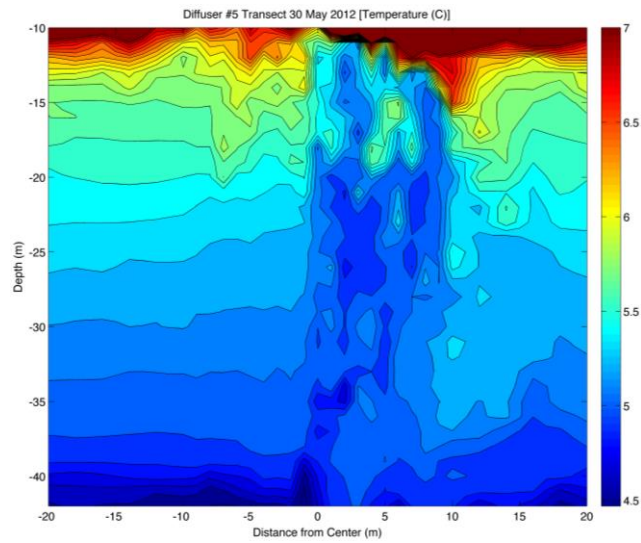
Figure A. 4. Diffuser temperature transect when the diffuser is operating

A.2 Carvins Cove 2013

Measurements of weather, temperature and velocity in Carvins Cove campaign are shown in Figure A. 5 - A.10.
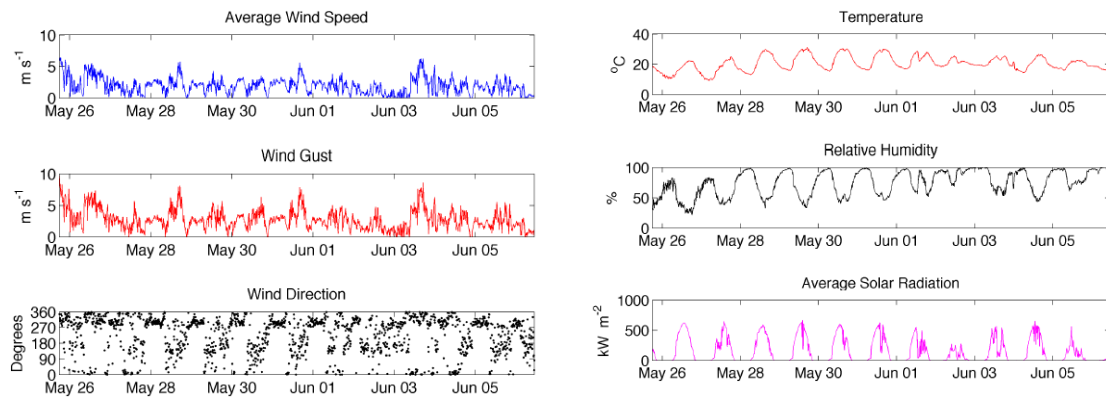
Figure A. 5. Weather measurements; Wind measurements (left side), and Temperature, Humidity, and Solar Radiation (right side)
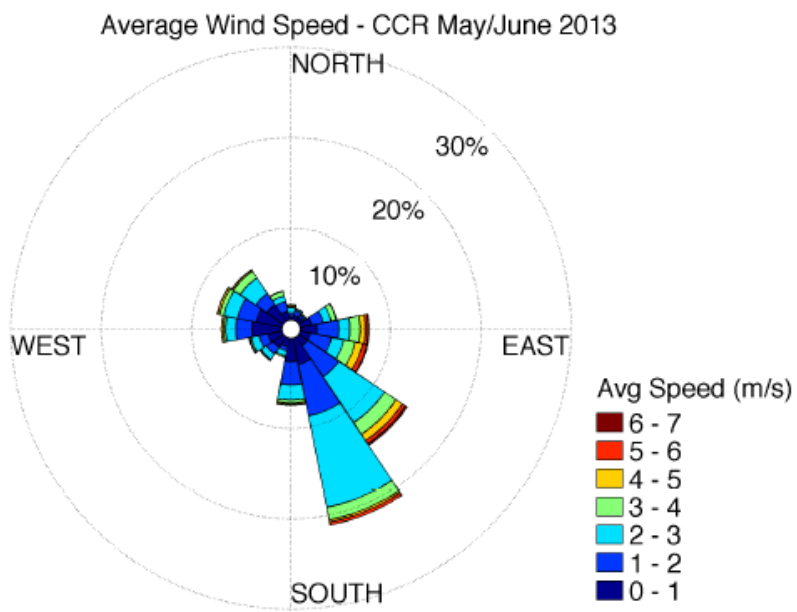
Figure A. 6. Wind measurement data for CCR 2013 campaign
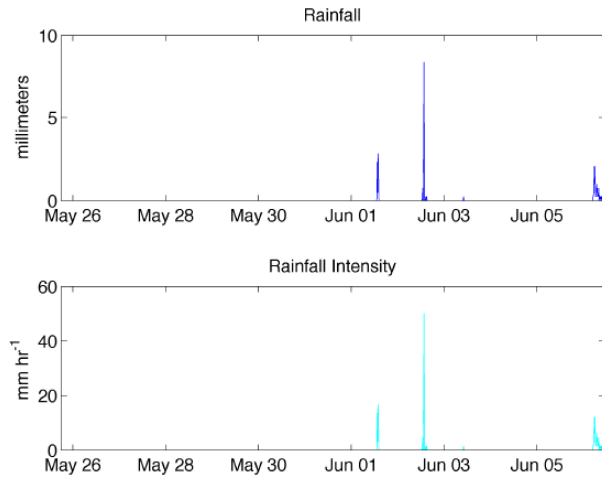
Figure A. 7. Rainfall measurement during the CCR campaign
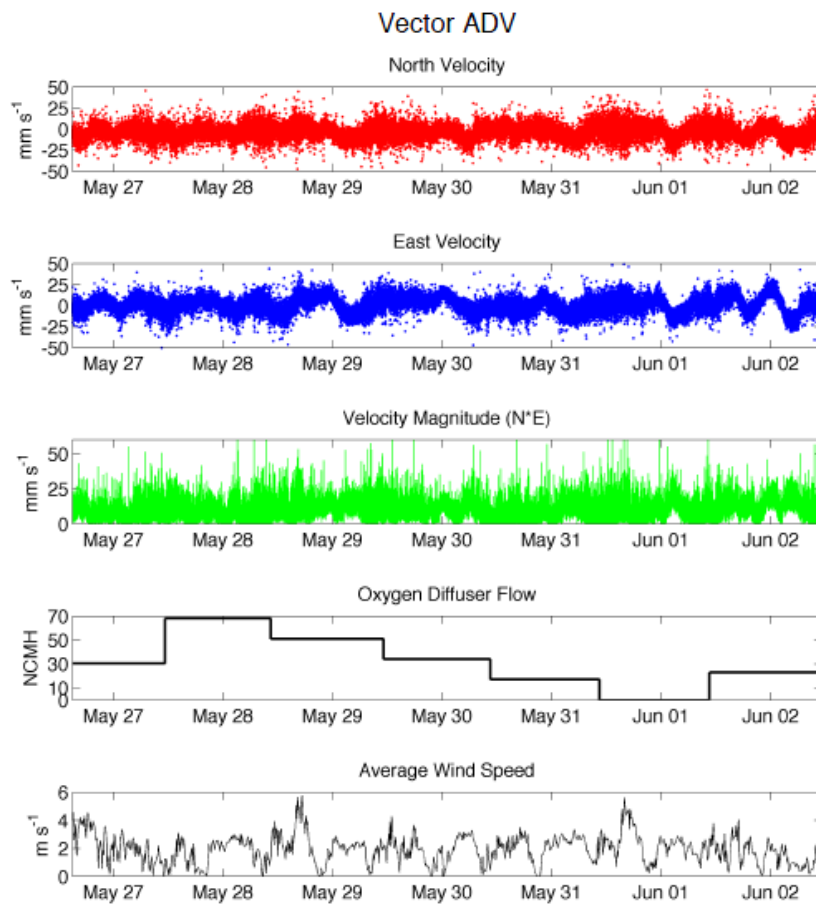
Figure A. 8. Components of velocity measured at 20 cm above the bottom (first three rows) with simultaneous diffuser flow rates (forth row) and wind speed (last row)
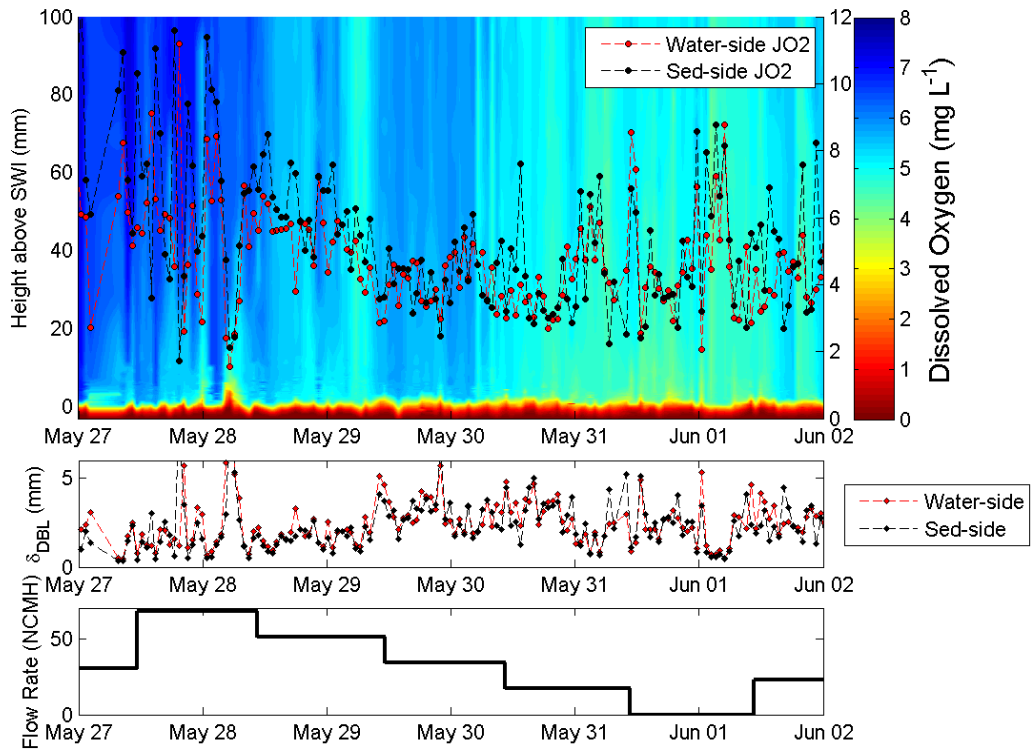
Figure A. 9. Time series of dissolved oxygen concentrations, oxygen fluxes, diffusive boundary layer thickness, and the stepped oxygenation system flow rate regime during CCR2013
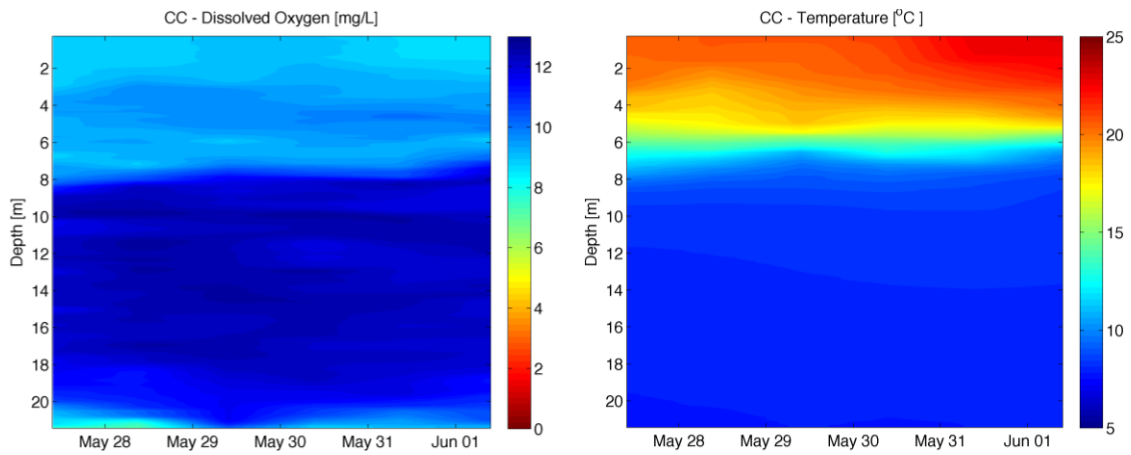

Figure A. 10. Measurements of DO (left column) and Temperature (right column) at CC
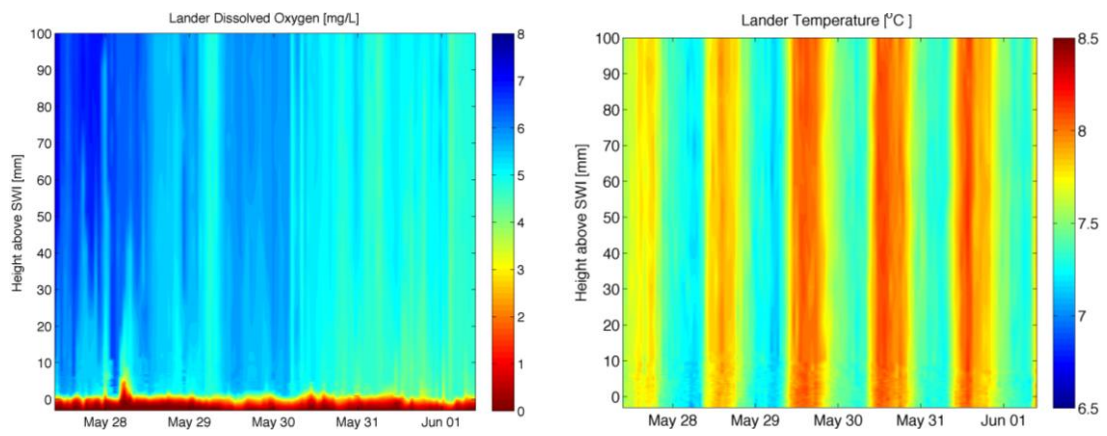
Figure A. 11. Measurements of DO and Temperature at the microprofiler